

Modelling and Simulation: Computational Intelligence in Medicine

Guest Editor: Ewa Pietka





Modelling and Simulation: Computational Intelligence in Medicine

Modelling and Simulation in Engineering

**Modelling and Simulation:
Computational Intelligence in Medicine**

Guest Editor: Ewa Pietka



Copyright © 2008 Hindawi Publishing Corporation. All rights reserved.

This is a special issue published in volume 2008 of “Modelling and Simulation in Engineering.” All articles are open access articles distributed under the Creative Commons Attribution License, which permits unrestricted use, distribution, and reproduction in any medium, provided the original work is properly cited.

Editor-in-Chief

Andrzej Bargiela, The University of Nottingham, UK

Associate Editors

K. Al-Begain, UK

Adel M. Alimi, Tunisia

Zeki Ayag, Turkey

Agostino Bruzzone, Italy

Michael Cloke, Malaysia

Andrzej Dzielinski, Poland

Piotr Fedelinski, Poland

F. Gao, UK

Ricardo Goncalves, Portugal

Ratan Guha, USA

Joanna Hartley, UK

Sergio Junco, Argentina

Iisakki Kosonen, Finland

Igor Kotenko, Russia

Natalio Krasnogor, UK

Azah Mohamed, Malaysia

Petr Musilek, Canada

Tomoharu Nakashima, Japan

Gaby Neumann, Germany

Alessandra Orsoni, UK

Javier Otamendi, Spain

Evtim Peytchev, UK

Ewa Pietka, Poland

Jerzy Rutkowi, Poland

Waleed Smari, USA

Boris Sokolov, Russia

Andrzej Swierniak, Poland

Soib Taib, Malaysia

Masahiro Tanaka, Japan

Andreas Tolk, USA

A. Verbraeck, The Netherlands

Bauke Vries, The Netherlands

Ivan Zelinka, Czech Republic

Borut Zupancic, Slovenia

Contents

Computation Intelligence in Medicine—Data Analysis and Modelling, Ewa Pietka
Volume 2008, Article ID 215073, 2 pages

A Computer-Aided Diagnosis System for Breast Cancer Using Independent Component Analysis and Fuzzy Classifier, Ikhlas Abdel-Qader and Fadi Abu-Amara
Volume 2008, Article ID 238305, 9 pages

Breast Tumor Simulation and Parameters Estimation Using Evolutionary Algorithms, Manu Mital and Ramana M. Pidaparti
Volume 2008, Article ID 756436, 6 pages

Hemodynamic Effect of Unequal Anterior Cerebral Artery Flow Rates on the Anterior Communicating Artery Bifurcation: A Computational Fluid Dynamics Study, Thomas Rau, Xing He, Prem Venugopal, Fernando Viñuela, Gary Duckwiler, and Daniel J. Valentino
Volume 2008, Article ID 691982, 9 pages

An Autonomic Nervous System Model Applied to the Analysis of Orthostatic Tests, Virginie Le Rolle, Alfredo I. Hernández, Pierre-Yves Richard, and Guy Carrault
Volume 2008, Article ID 427926, 15 pages

Experimental and Numerical Modeling of Screws Used for Rigid Internal Fixation of Mandibular Fractures, Naresh Chaudhary, Scott T. Lovald, Jon Wagner, Tariq Khraishi, and Bret Baack
Volume 2008, Article ID 628120, 11 pages

Editorial

Computation Intelligence in Medicine—Data Analysis and Modelling

Ewa Pietka

Silesian University of Technology, Institute of Electronics, 44-100 Gliwice, Poland

Correspondence should be addressed to Ewa Pietka, epietka@polsl.pl

Received 31 December 2008; Accepted 31 December 2008

Copyright © 2008 Ewa Pietka. This is an open access article distributed under the Creative Commons Attribution License, which permits unrestricted use, distribution, and reproduction in any medium, provided the original work is properly cited.

In clinical application, we deal with problems which have to be solved in a fast and objective way. However, human observation is influenced by internal (coming from the observer) as well as external (often independent from the observer) impacts. The objectivity of classification is restricted by the receptivity of human senses which are influenced by the experiences or level of training, psychological conditions (tiredness, hurry, etc.), as well as external conditions (lighting, destructive noise, etc.). The failure in perception questions the entire recognition process. The recognition process itself, influenced also by the abovementioned conditions, may cause a slow down and/or lead to a false diagnosis.

New computerized approaches to various problems have become critically important in healthcare. Mathematical information analysis, modelling, and computer simulation become standard tools underpinning the current rapid progress with developing computational intelligence. We are witnessing a radical change as technologies have been integrated into systems that address the core of medicine, including patient care in ambulatory and in-patient setting, disease prevention, health promotion, rehabilitation, and home care. Computational intelligence is in widespread use for the support of patient medical diagnosis and treatment, the assessment of the quality of care, and the enhancement of decision making, modelling, simulation, and medical research. A computerized support in the analysis of patient information and implementation of a computer-aided diagnosis and treatment systems increases the objectivity of the analysis and speeds up the response to pathological changes.

This special issue consists of 5 articles. The subsequent papers are organized into 3 groups.

The first one employs mathematical tools in the data analysis. A computer-aided diagnosis system for breast

cancer has been presented by Abdel-Qader and Abu-Amara. They have implemented the independent component analysis and fuzzy classifier to identify and label suspicious regions in mammograms.

An estimation methodology is presented by Mital and Pidaparti to determine the breast tumor parameters using the surface temperature profile that may be obtained by infrared thermography. The estimation methodology involves evolutionary algorithms using artificial neural network and genetic algorithm. The artificial neural network is used to map the relationship of tumor depth, tumor size, and the heat generation to the temperature profile over the idealized breast model. The genetic algorithm estimates the tumor parameters (depth, size, and heat generation) by minimizing a fitness function involving the temperature profiles obtained from simulated data or clinical data.

The second group has employed a modelling technique as a support in the assessment or decision-making problem.

Rau et al. have implemented the computational fluid dynamics techniques to investigate the hemodynamic effect of unequal anterior cerebral artery flow rates on the anterior cerebral and anterior communicating artery (ACA-ACOM) bifurcations. Using an idealized 2D symmetric model of the ACA-ACOM geometry, the flow field and wall shear stress (WSS) at the bifurcation regions are assessed for pulsatile inflows with left to right flow ratios.

A model-based approach to reproduce individual heart rate signals acquired during tilt tests is proposed by Le Rolle et al. A new physiological model adapted to this problem and coupling the autonomic nervous system, the cardiovascular system, and global ventricular mechanics is presented. Evolutionary algorithms are used for the identification of patient-specific parameters, in order to reproduce heart rate

signals obtained during tilt tests. The proposed approach is able to reproduce the main components of the observed heart rate signals and represents a first step toward a model-based interpretation of these signals.

The third group, employed in orthopedics, develops experimental and numerical methods to explore the stresses generated around the implants and bone screws. Chaudhary et al. have presented a finite-element model of a human mandible created with a fixated fracture in the parasymphiseal region. The mandibular model has then been anatomically loaded. Next, the forces exerted by the fixation plate onto the simplified screws are obtained and transferred to another finite-element submodel of a screw implant embedded in a trilaminar block with material properties of cortical and cancellous bone. The stress in the bone surrounding the screw implant has been compared for different screw configurations.

Ewa Pietka

Research Article

A Computer-Aided Diagnosis System for Breast Cancer Using Independent Component Analysis and Fuzzy Classifier

Ikhlas Abdel-Qader and Fadi Abu-Amara

Department of Electrical and Computer Engineering, Western Michigan University, MI 49008, USA

Correspondence should be addressed to Ikhlas Abdel-Qader, abdelqader@wmich.edu

Received 27 August 2007; Revised 10 January 2008; Accepted 11 March 2008

Recommended by Ewa Pietka

Screening mammograms is a repetitive task that causes fatigue and eye strain since for every thousand cases analyzed by a radiologist, only 3–4 are cancerous and thus an abnormality may be overlooked. Computer-aided detection (CAD) algorithms were developed to assist radiologists in detecting mammographic lesions. In this paper, a computer-aided detection and diagnosis (CADD) system for breast cancer is developed. The framework is based on combining principal component analysis (PCA), independent component analysis (ICA), and a fuzzy classifier to identify and label suspicious regions. This is a novel approach since it uses a fuzzy classifier integrated into the ICA model. Implemented and tested using MIAS database. This algorithm results in the classification of a mammogram as either normal or abnormal. Furthermore, if abnormal, it differentiates it into a benign or a malignant tissue. Results show that this system has 84.03% accuracy in detecting all kinds of abnormalities and 78% diagnosis accuracy.

Copyright © 2008 I. Abdel-Qader and F. Abu-Amara. This is an open access article distributed under the Creative Commons Attribution License, which permits unrestricted use, distribution, and reproduction in any medium, provided the original work is properly cited.

1. INTRODUCTION

Breast cancer is considered one of the most common and fatal cancers among women in the USA [1]. According to National Cancer Institute, 40 480 women died due to this disease and on average every three minutes one woman is diagnosed with this cancer. Right now there are over two and a half million women in the US who have been treated from it [1]. Radiologists visually examine mammograms to search for signs of abnormal regions. They usually look for clusters of microcalcifications, architectural distortions, or masses.

Early detection of breast cancer via mammography improves treatment chances and survival rates [2]. Unfortunately, mammography is not perfect. False positive (FP) rates are 15–30% due to the overlap in the appearance of malignant and benign abnormalities while false negative (FN) rates are 10–30%. A result of FP is defined to be when a radiologist reports a suspicious change in the breast but no cancer is found after further examinations. Therefore, it leads to unnecessary biopsies and anxiety. A result of FN means failure to detect or correctly characterize breast cancer in a case of which later tests conclude that cancer is present. Nonetheless, mammography has an overall accuracy rate of 90% [3].

CAD algorithms have been developed to assist radiologists in detecting mammographic lesions. These systems are regarded as a second reader, and the final decision is left to the radiologist. CAD algorithms have improved total radiologist accuracy of detection of cancerous tissues [4]. CADD algorithms are considered as an extremely challenging task for various reasons. First, the imaging system may have serious imperfections. Second, the image analysis task is compounded by the large variability in the appearance of abnormal regions. Finally, abnormal regions are often hidden in dense breast tissue. The goal of the detection stage is to assist radiologists in locating abnormal tissues.

Many methods have been proposed in the literature for mammography detection and diagnosis utilizing a wide variety of algorithms. Chang et al. [5] developed a 3D snake algorithm that finds the tumor's contour after reducing the noise levels and followed by an edge enhancement process. Finally, the tumor's contour is estimated by using the gradient vector flow snake. Kobatake et al. [6] proposed the iris filter to detect lesions as suspicious regions with a low contrast compared to their background. The proposed filter has the features' extraction ability of malignant tissues. Bocchi et al. [7] developed an algorithm for microcalcification

detection and classification by which the existing tumors are detected using a region growing method combined with a neural network-based classifier. Then, microcalcification clusters are detected and classified by using a second fractal model. Also, Li et al. [8] developed a method for detecting tumors using a segmentation process, adaptive thresholding, and modified Markov random fields, followed by a classification step based on a fuzzy binary decision tree. Bruce and Adhami [9] used the modulus-maxima technique of discrete wavelet transform as a feature extraction technique combined with a Euclidean distance classifier. A radial distance measure of mass boundaries is used to extract multiresolution shape features. Finally, the leave-one-out and apparent methods are used to test their proposed technique. Peña-Reyes and Sipper [10] applied a combined fuzzy-genetic approach with new methods as a computer-aided diagnosis system. Zheng and Chan [11] combined artificial intelligent methods with the discrete wavelet transform to build an algorithm for mass detection. Hassanien and Ali [12] proposed an enhanced rough set technique for feature reduction and classification. Swiniarski and Lim [13] integrated ICA with rough set model for breast-cancer detection. First, features are reduced and extracted using ICA. Then, extracted features are selected using a rough set model. Finally, a rough set-based method is used for rule-based classifier design.

This work is based on integrating PCA, ICA, and fuzzy classifier to identify and label suspicious regions from digitized mammograms. The rest of this paper is organized as follows: Section 2 presents PCA and ICA algorithms and covers fuzzy logic adaptation as a classifier. The proposed integrated approach is presented in Section 3. Section 4 presents the experimental results followed by the conclusions in Section 5.

2. BACKGROUND

2.1. PCA

PCA is a decorrelation-based technique that finds the basis vectors for a subspace in order to select the most important information. PCA consists of two phases. The first phase finds ν uncorrelated and orthogonal vectors; and the second phase projects the testing data into a subspace spanned by these ν vectors [14]. PCA algorithm can be presented as follows:

- (i) construct R_{train} matrix with dimension $N \times M$, where N is the total number of training subimages and M is the size of each square subimage; then, generate its normalized matrix $P_{M \times N}$;
- (ii) covariance matrix is constructed using

$$C_{N \times N} = P_{N \times M}^T P_{M \times N}; \quad (1)$$

- (iii) let λ_i and E_i , $i = 1, 2, \dots, M$, be its eigenvalues and eigenvectors that satisfy the equation $C E_i = \lambda_i E_i$, where $\lambda_1 \geq \lambda_2 \geq \dots \geq \lambda_M \geq 0$; discard of all eigenvalues less than T (a predetermined threshold) and retain

the rest (the principal components) to produce the reduced matrix $R_{M \times \nu}^R$. T is calculated using

$$T = \frac{\sum_{k=1}^{\nu} \lambda_k}{\sum_{q=1}^M \lambda_q}. \quad (2)$$

The given testing data R_{test} is projected into the space spanned by the reduced training matrix $R_{M \times \nu}^R$ using

$$W_{\nu \times N} = (R_{M \times \nu}^R)^T R_{\text{test}, M \times N}. \quad (3)$$

2.2. ICA

Higher-order statistics, such as ICA techniques, are used to compensate for PCA shortcomings. ICA is based on the use of moments and cumulants up to fourth-order to describe any distribution of a random variable.

In general, ICA is a relatively new technique developed to find a linear representation of nongaussian data so that the data components are statistically as independent as possible. ICA has the ability to describe localized shape variations and it does not require a Gaussian distribution of the data as in PCA. However, the resulting vectors are not ordered; and, therefore, ICA requires a method for ordering the resulting vectors.

The statistical latent variables model is used to define ICA. Assuming that we have n linear mixtures $r_1 \dots r_n$ of n independent components $s_1 \dots s_n$ according to

$$r = \sum_{i=1}^n a_i s_i \quad \text{or} \quad R = AS. \quad (4)$$

The digital mammographic image R is considered as a mixture of linear combination of statistically independent source regions S where A , the mixing matrix, and its coefficients describe uniquely the mixed source regions and can be used as extracted features. After estimating the matrix A and its inverse W (the separating matrix), the independent components can be estimated using

$$S = WR. \quad (5)$$

2.3. Fuzzy classifier

Fuzzy logic can be interpreted as the emulation of human reasoning on computers [15]. Fuzzy rules are more comprehensible than crisp rules since they can be expressed in terms of linguistic concepts. The value of the linguistic variable is not a number but a word. For example, the linguistic variable "size" might have the values "small," "medium," and "large." Each one of these values is called a fuzzy set when implemented using fuzzy logic and thus fuzzy sets can be used to model linguistic variables.

Fuzzy classifier is ideally suited to the labeled observed data to provide interpretable solutions. It handles imprecise data and the resulting fuzzy rules are interpretable, that is, fuzzy classifier structure can be analyzed through its semantic structure. There are two different methods for development of fuzzy classifiers; approximate and descriptive fuzzy rule base.

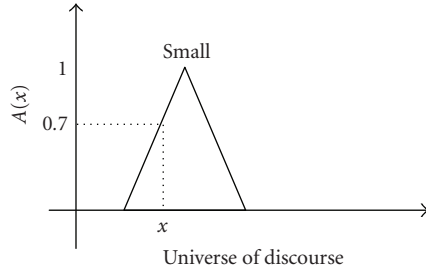


FIGURE 1: A triangular membership function of the fuzzy set “Small.”

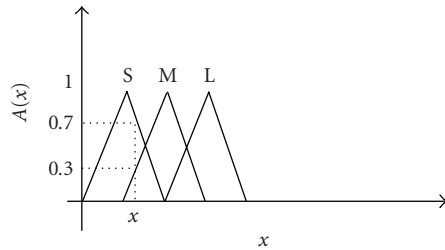


FIGURE 2: Fuzzy space of the object of Figure 1 that consists of three fuzzy sets: “Small,” “Medium,” and “Large.”

Each fuzzy rule is defined using membership function of fuzzy sets in an approximate fuzzy rule base which is implemented in this work. Values of the linguistic variable can be described in terms of numerals using membership functions. The object membership degree to a fuzzy set defines a membership function. Its domain is the universe of discourse (all values an object may take) and its range of the interval $[0.0, 1.0]$. A commonly used membership function is the triangular function. Figure 1 shows a triangular membership function of a fuzzy set “Small.”

In Figure 1, an object x has a membership degree of 0.7 to the fuzzy set “Small.” A fuzzy space is defined to be the set of fuzzy sets that define fuzzy classes for a particular object as shown in Figure 2.

Fuzzy space allows the object to partially belong to different classes simultaneously. This idea is very useful in cases where the difference between classes is not well defined. For example, the object x has a membership degree of 0.7 to the fuzzy set “Small” and 0.3 to the fuzzy set “Medium.” Similarly, in mammographic images, the difference between benign/malignant and normal/abnormal subimages is not well defined. For example, an abnormal subimage may be classified as benign rather than malignant which can be described in terms of numerals using membership functions as it has a membership degree of 0.7 to the fuzzy set “benign” and 0.3 to the fuzzy set “malignant.” Fuzzy membership functions are easy to implement and their fuzzy inference engines are fast.

In descriptive fuzzy rule base, linguistic variables are commonly defined by fuzzy if-then rules where labels A_{ij} are used to represent a discrete set of linguistic fuzzy sets. For example, fuzzy classification rules that describe each class of

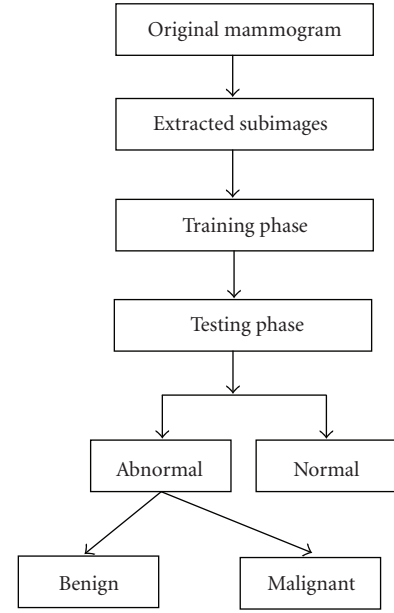


FIGURE 3: Block diagram of the proposed CADD system.

subimages may be developed to represent each class. Fuzzy rules have the form

$$\text{IF antecedent THEN consequent [weight].} \quad (6)$$

Fuzzy rules can also be expressed as

$$R_i : \text{If } x_1 \text{ is } A_{i1} \text{ and } \dots x_t \text{ is } A_{it} \text{ then } Y = \text{Class}_i \text{ [weight],} \quad (7)$$

where Y represents the decision class (i.e., normal, abnormal, benign, or malignant) and A_{ij} represents a fuzzy set for $j: 1, \dots, t$ th selected feature.

3. PROPOSED CADD ALGORITHM

In this section, a computer-aided detection and diagnosis algorithm of suspicious regions in mammograms is developed. PCA algorithm is used as a dimensionality reduction module followed by ICA as a feature extraction module. Finally, a fuzzy classifier is used to classify testing subimages into normal/abnormal and at a later stage to classify the abnormal subimages into malignant/benign as a diagnosis system. Figure 3 presents the general framework for this system.

3.1. Subimages generation

MIAS database has a total of 119 regions of suspicion (ROS) divided into 51 malignant and 68 benign. Two different sets of abnormal subimages, each set consists of 119 ROS, are cropped and scaled into 35×35 and 45×45 pixels based on the center of each abnormality.

Then, five different sets of normal subimages, each set consists of 119 subimages, are cropped and scaled randomly from normal MIAS mammograms where two sets of size 35×35 and three sets of size 45×45 pixels.

Each set of abnormal subimages is mixed with one set of normal subimages every time and then divided into two groups; one for training phase and the other group for testing phase as shown in Table 1.

Each training set is used to create the matrix R_{train} with dimension $N \times M$ where each row contains a subimage. The training matrix dimensionality is reduced by using PCA algorithm to generate R^R . Then, the covariance matrix is estimated by using

$$C_{N \times \nu} = R_{\text{train}_{N \times M}} R_{M \times \nu}^R. \quad (8)$$

3.2. Unsupervised learning

Estimation of the separating matrix, W , and the independent source regions, S , is done in an unsupervised manner. The independent source regions are estimated by using (9), where $(R^R)^T$ is the transpose of the reduced matrix R^R . The separating matrix, W , is initialized to the identity matrix yielding

$$S = W(R^R)^T. \quad (9)$$

To reach the maximum statistical independence of S , the nonlinear function $\Phi(S)$ is used to estimate the marginal probability density function of S using its central moments and cumulants. Minimum mutual information algorithm [16] is used to estimate $\Phi(S)$ as shown in (10)–(14). Equations (10) and (11) are used to estimate the i th central moments and cumulants where E is the expected value and μ is the mean of the current feature r . Equations (12)–(14) are used to estimate $\Phi(S)$ (\circ indicates the Hadamard product of two matrices)

$$m_i = E(r - \mu)^i, \quad (10)$$

$$k_3 = m_3, \quad k_4 = m_4 - 3, \quad (11)$$

$$\Phi(S) = f_1(k_3, k_4) \circ S^2 + f_2(k_3, k_4) \circ S^3, \quad (12)$$

$$f_1(k_3, k_4) = 0.5 k_3 (4.5 k_4 - 1), \quad (13)$$

$$f_2(k_3, k_4) = 1.5(k_3)^2 + \frac{1}{6} k_4 (4.5 k_4 - 1). \quad (14)$$

Natural gradient descent method [16] is used to estimate the change of W according to $dW/dt = \eta[I - \Phi(S)S^T]W$, where $\eta(t)$ is the learning rate and I is the identity matrix. If dW/dt is not close to zero, W is updated using

$$W_i(t+1) = W_i(t) + \frac{dW}{dt}. \quad (15)$$

Finally, selected features resulting from the training process are estimated using minimum square error method (MSE) [17, 18].

(i) From (8), the training matrix is reconstructed as

$$R_{\text{train}} \approx C(R^R)^T. \quad (16)$$

(ii) Substitute (9) into (16):

$$R_{\text{train}} \approx C_{N \times \nu}(R^R)^T = C_{N \times \nu}AS. \quad (17)$$

(iii) There, the reduced dimensionality selected features from the training set are estimated by

$$Q_{\text{train}} = CA. \quad (18)$$

Same procedure followed for training data is used for testing; and R_{test} is projected into the reduced matrix (R^R) from the training procedure. The reduced dimensionality extracted features from the testing procedure are estimated by using

$$Q_{\text{test}} = R_{\text{test}}R^RA. \quad (19)$$

3.3. Fuzzy classifier modeling

The matrices Q_{train} and Q_{test} contain the reduced dimensionality extracted features from subimages where each one of size N by ν . Each class of subimages (normal, abnormal, benign, and malignant) is represented by a single fuzzy rule by aggregating the membership functions of each antecedent fuzzy set using the information about selected feature values of training subimages.

The proposed fuzzy-based classification algorithm can be summarized as follows.

- (1) Four activation functions μ_{bs} , μ_{ms} , μ_{as} , μ_{ns} , with each one is of size N by 1, are initialized to 0 where each element of them represents the aggregated membership functions of the selected feature values for the corresponding testing subimage. Each one represents the degree of activation of the selected feature values and so these parameters are defined as
 - (i) μ_{bs} : represents the degree of activation for the benign testing subimages,
 - (ii) μ_{ms} : represents the degree of activation for the malignant testing subimages,
 - (iii) μ_{as} : represents the degree of activation for the abnormal testing subimages, and
 - (iv) μ_{ns} : represents the degree of activation for the normal testing subimages.
- (2) Since subimages have different intensities and the goal is to reduce the variation and the computational complexity, the selected features of Q_{train} and Q_{test} are mapped into a limited range of $[r_1, r_2]$ using

$$q(x, y) = r_1 + \frac{(q(x, y) - \min(q)) (r_2 - r_1)}{\max(q) - \min(q)}. \quad (20)$$

- (3) Using (21), membership functions of fuzzy sets of the testing subimages are obtained from the product space of the selected features from the training phase:

$$A_{ij}(x_j) = \frac{s_i(x_j)}{s(x_j)}, \quad i = 1, \dots, \nu; j = 1, \dots, N, \quad (21)$$

where $s_i(x_j)$ represents number of samples of the current feature x_j , $s(x_j)$ represents the total number of all samples in the current feature x_j , that is, the product space of the current feature. Also, the subscript (j)

TABLE 1: Different sets used to evaluate the detection algorithm performance.

#	Training set			Testing set			
	ROS	Normal	Total	ROS	Normal	Total	Size-pixels
1	60	59	119	59	60	119	35 × 35
2	60	59	119	59	60	119	35 × 35
3	60	59	119	59	60	119	45 × 45
4	60	59	119	59	60	119	45 × 45
5	60	59	119	59	60	119	45 × 45

is the index for the selected feature for each training subimage, and (i) is the index for the current processed sample of the current feature.

- (4) The membership functions are normalized by using

$$A_{ij}(x_j) = \frac{A_{ij}(x_j)}{\max_{ij}(A_j(x_j))}. \quad (22)$$

- (5) The degree of activation of the developed membership functions is computed for the testing subimages for μ_{as} , μ_{ns} in the detection phase and for μ_{bs} , μ_{ms} in the diagnosis phase by aggregating estimated membership functions:

$$\mu_i(x) = \sum_{j=1}^N A_{ij}(x_j). \quad (23)$$

- (6) There are many methods used in the literature to determine to which class a subimage belongs (i.e., normal/abnormal or benign/malignant). An efficient one is the maximum algorithm. It classifies the testing subimage into the class that has the maximum degree of activation according to (24) where C_1 is used as an index of a testing subimage being identified as normal or abnormal and C_2 for being identified as benign or malignant:

$$\begin{aligned} C_1 &= \max(\mu_{as}(x), \mu_{ns}(x)), \\ C_2 &= \max(\mu_{ms}(x), \mu_{bs}(x)). \end{aligned} \quad (24)$$

4. EXPERIMENTAL RESULTS

Table 2 shows results of the proposed CADD algorithm against PCA and ICA algorithms for the same testing data using fuzzy classifier. Algorithm accuracy is defined as the ratio between number of correctly classified testing subimages and total number of testing subimages. Results demonstrate that combining ICA and PCA algorithms improves the total algorithm performance in all testing sets over usage of PCA algorithm only. PCA algorithm has a best result of 80.67% while 84.03% for the proposed CADD algorithm as shown in Table 2. The proposed algorithm improved PCA algorithm accuracy with an average of 8.56% for all tests.

Table 2 also shows the simulation results of ICA algorithm versus the proposed CADD algorithm. ICA algorithm has an accuracy of 49.58% in all testing sets. In contrast, the best result of applying the proposed CADD algorithm is 84.03%. These results indicate that using PCA algorithm for

dimensionality reduction before ICA algorithm improves the ICA algorithm accuracy with an average of 50.51%. Results from ICA algorithm show that fuzzy classifier performance is degraded when no dimensionality reduction module is implemented. A fuzzy classifier requires features reduction method in order to minimize total number of membership functions and improves its accuracy. As for ICA algorithm alone, each subimage has larger number of selected features and therefore fuzzy classifier performance is degraded in all testing subimages.

The experimental results of the proposed CADD algorithm as a computer-aided diagnosis system are shown in Table 3. The best result is 78% where 15 malignant subimages out of 25 are correctly classified and 31 benign subimages out of 34 are correctly classified.

This system uses several parameters that impact the performance and accuracy of results such as the number of selected principal components, learning rate, and mapping range.

4.1. Number of selected PC

Using PCA algorithm to reduce data dimensionality as a pre-processing step for ICA algorithm affects the total algorithm accuracy. In Table 4, simulation results on test sets 1–5 (PC indicates the number of selected principal components) are shown. These results indicate that selecting less than 11 principal components achieves acceptable results in all simulations. This means that less than 0.81% of principal components are selected for subimages of size 35 × 35 pixels and less than 0.5% of principal components are selected for subimages of size 45 × 45 pixels. This is harmony with all literature that used PCA algorithm for dimensionality reduction.

4.2. Learning rate

The learning rate for computing the change in W for ICA algorithm determines the speed of convergence for dW/dt and it impacts the total algorithm accuracy. Figures 4–8 show learning rate impact on test sets 1–5. It can be concluded that choosing a learning rate close to 0.0045 produce acceptable results for all sets.

4.3. Mapping range

Figures 9–13 show the accuracy of the results versus the mapping range values for all test sets 1–5 and it can be concluded

TABLE 2: F_P and F_N ; and total PCA, ICA, and PCA-ICA algorithms accuracy.

Set	PCA				ICA			CADD			
	PC	F_P	F_N	Accuracy	F_P	F_N	Accuracy	PC	F_P	F_N	Accuracy
1	19	17.65%	25.21%	57.14%	10.08%	40.34%	49.58%	25	15.13%	18.48%	66.39%
2	20	26.05%	10.08%	63.87%	10.08%	40.34%	49.58%	10	12.61%	18.48%	68.91%
3	5	10.08%	14.29%	75.63%	10.08%	40.34%	49.58%	5	9.24%	6.73%	84.03%
4	6	12.61%	21%	66.39%	10.08%	40.34%	49.58%	5	20.17%	10.08%	69.75%
5	5	11.75%	7.58%	80.67%	10.08%	40.34%	49.58%	6	7.56%	8.41%	84.03%

TABLE 3: Computer-aided diagnosis using CADD algorithm.

Set	Training set			Testing set			Size-pixels	PC	CADD Algorithm		
	Benign	Malignant	Total	Benign	Malignant	Total			FP	FN	Accuracy
1	34	26	60	34	25	59	35×35	36	5.1%	16.9%	78%
2	34	26	60	34	25	59	45×45	6	8.48%	13.55%	77.97%

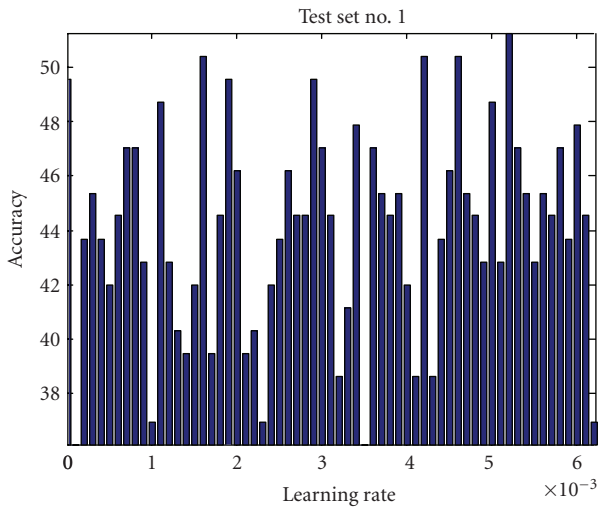


FIGURE 4: Learning rate impact on algorithm accuracy for test set no. 1 where other parameters are kept constant.

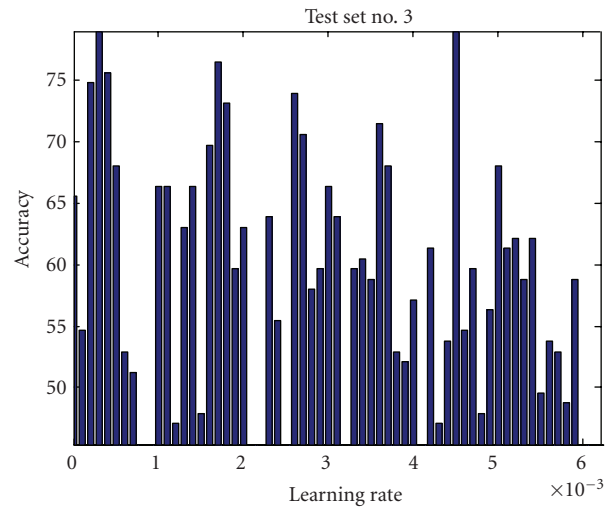


FIGURE 6: Learning rate impact on algorithm accuracy for test set no. 3 where other parameters are kept constant.

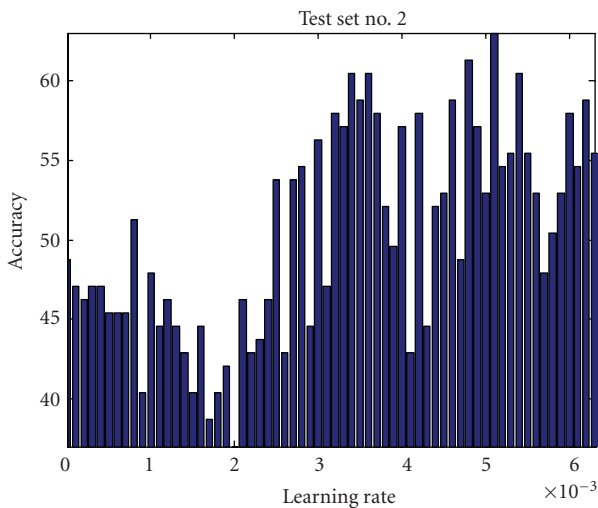


FIGURE 5: Learning rate impact on algorithm accuracy for test set no. 2 where other parameters are kept constant.

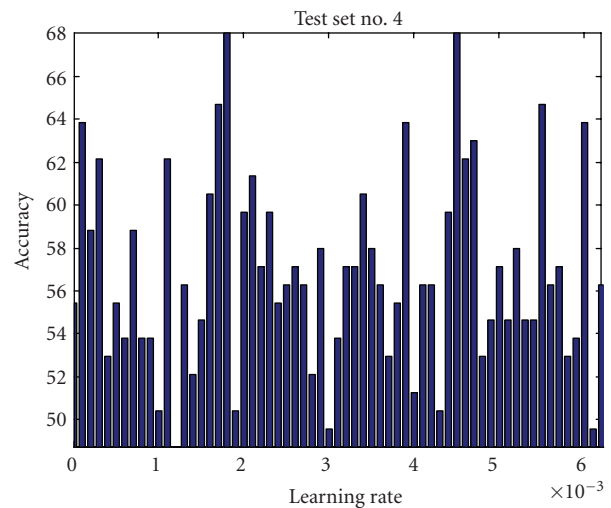


FIGURE 7: Learning rate impact on algorithm accuracy for test set no. 4 where other parameters are kept constant.

TABLE 4: Number of selected principal components impact on algorithm accuracy where learning rate and mapping range of each set are kept fixed.

PC	Set no. 1	Set no. 2	Set no. 3	Set no. 4	Set no. 5
5	61.35%	65.55%	84%	69.75%	81.52%
6	55.46%	64.71%	79.83%	68.07%	84.03%
7	62.19%	66.39%	78.99%	68.91%	82.35%
8	66.39%	66.39%	78.99%	65.55%	78.15%
9	59.66%	66.39%	70.59%	67.23%	76.47%
10	58.82%	68.91%	80.67%	66.39%	74.79%
11	63.03%	65.55%	69.75%	63.87%	75.63%
12	58.82%	60.5%	72.27%	63.03%	78.15%
13	62.19%	63.87%	70.59%	63.87%	74.79%
14	63.87%	62.19%	73.95%	62.19%	77.31%
15	57.98%	63.03%	69.75%	63.03%	73.95%
16	62.19%	59.66%	68.07%	63.03%	76.47%
17	62.19%	67.23%	72.29%	63.87%	77.31%
18	63.03%	60.5%	71.43%	62.19%	76.47%
19	64.71%	67.23%	72.29%	64.71%	79.83%
20	62.19%	64.71%	79.83%	62.19%	73.95%
21	60.5%	66.39%	74.79%	61.35%	80.67%
22	63.03%	66.39%	78.15%	62.19%	71.43%
23	63.03%	63.87%	80.67%	63.87%	74.79%
24	58.82%	60.5%	73.95%	62.19%	80.67%
25	59.66%	60.5%	68.91%	63.03%	79.83%

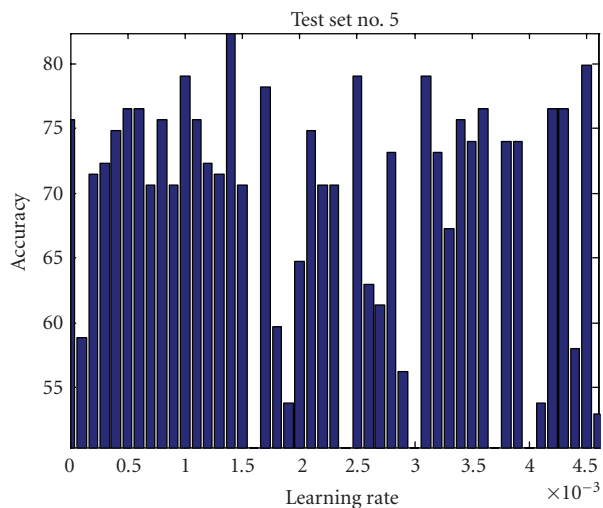


FIGURE 8: Learning rate impact on algorithm accuracy for test set no. 5 where other parameters are kept constant.

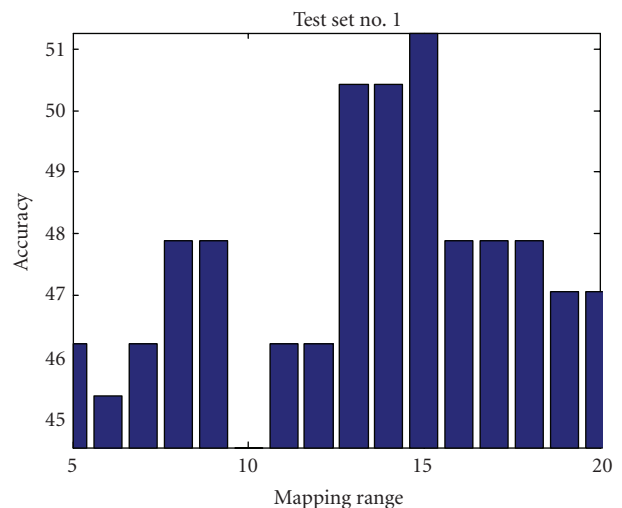


FIGURE 9: Mapping range impact on algorithm accuracy for test set no. 1.

that choosing a mapping range equal to $[0, 9]$ or $[0, 15]$ is acceptable for all testing sets.

The proposed system performance is a parameter-dependent and an investigation of this dependency is outside this presentation but rather is left for future investigations. Efforts developed earlier such as in [19, 20] can be investigated. Estimating the parameters will continue to be one of the main disadvantages of algorithms such ICA where human intervention is needed.

In other classification methods such as in fractal models, [7], a set of 30 mammograms are used that contains single and clustered microcalcifications. 50 subimages are extracted and divided into 30 subimages for the training phase and 20 subimages for the testing phase. Results of using two different multilayer subnetworks in neural network-based classifier indicate that the proposed system has a classification accuracy of 90%. Also, in discrete wavelet transform method [9], a set of 60 mammograms are used. Masses are segmented

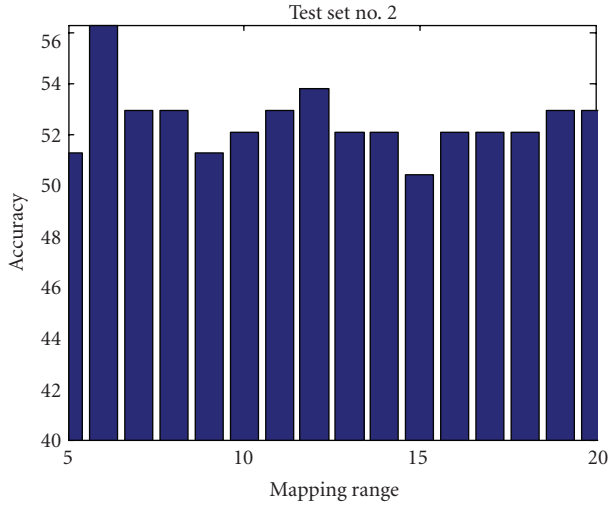


FIGURE 10: Mapping range impact on algorithm accuracy for test set no. 2.

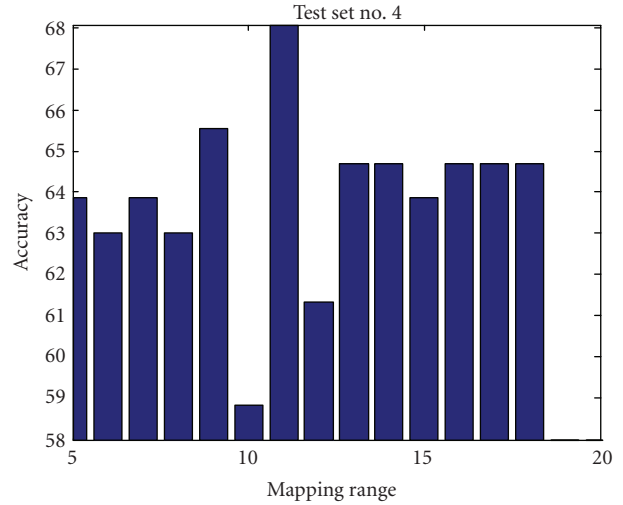


FIGURE 12: Mapping range impact on algorithm accuracy for test set no. 4.

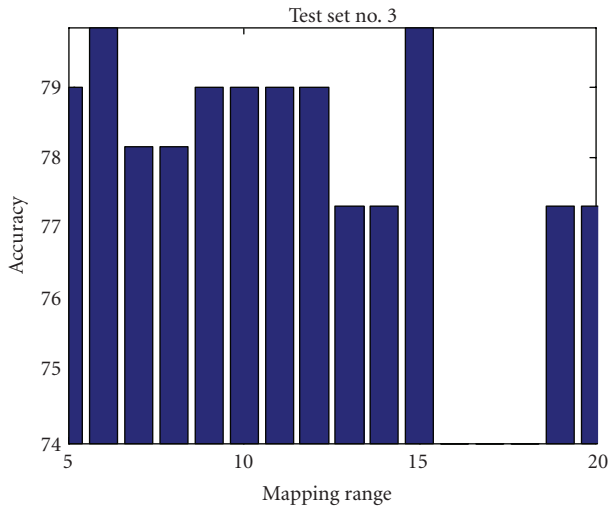


FIGURE 11: Mapping range impact on algorithm accuracy for test set no. 3.

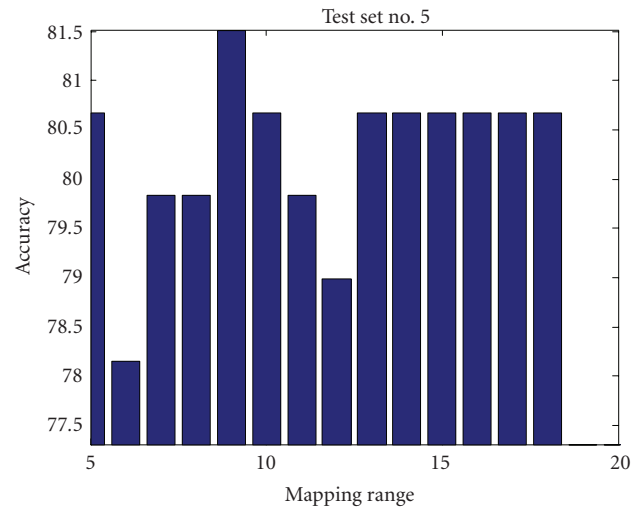


FIGURE 13: Mapping range impact on algorithm accuracy for test set no. 5.

manually as a preprocessing step for the classification system. The proposed system classifies masses into round, nodular, or stellate. Results indicate a classification accuracy of 83%. In [13], 330 subimages are cropped and scaled into sizes of 20×20 , 40×40 , and 60×60 pixels from all MIAS mammograms as one subimage from each mammogram. Results using ICA-Rough indicate a classification accuracy of 82.22% for subimages of size 60×60 pixels and for PCA-Rough of 88.57% for subimages of size 40×40 pixels.

Furthermore, Table 2 shows that each test set has different algorithm accuracy so cropping size for example has an impact on the results.

5. CONCLUDING REMARKS

A CADD system has been developed and implemented. Its framework is based on integrating PCA, ICA, and fuzzy

logic. The performance of the proposed CADD is compared against PCA and ICA performance individually. Extensive simulations using 833 subimages are performed. These results indicate that combining ICA and PCA algorithms improves PCA algorithm accuracy about 8.56% for all test sets and ICA algorithm accuracy about 50.51%. The best results are obtained with subimage sizes of 45×45 pixels over the 35×35 size. Using ICA algorithm for feature extraction without using a preprocessing module of PCA degraded fuzzy classifier performance. ICA takes advantage of the reduction of dimensionality and noise to produce more accurate and robust results. Parameter values play a vital role in the system's performance and their selection should be investigated to improve system's robustness. Other membership functions can be modeled based on mean and standard deviation of selected feature values.

ACKNOWLEDGMENTS

Partial support of this work was provided by the National Science Foundation Grant (MRI-0215356) and by Western Michigan University FRACASF Award (WMU: 2005–2007). The authors would like also to acknowledge Western Michigan University for its support and contributions to the Information Technology and Image Analysis (ITIA) Center.

REFERENCES

- [1] National Cancer Institute, “U.S. National Institute of Health,” 2008, <http://www.cancer.gov/cancertopics/types/breast/>.
- [2] C. H. Lee, “Screening mammography: proven benefit, continued controversy,” *Radiologic Clinics of North America*, vol. 40, no. 3, pp. 395–407, 2002.
- [3] C. Smart, R. Hendrick, J. Rutledge, and R. Smith, “Benefit of mammography screening in women ages 40 to 49 years: current evidence from randomized controlled trials,” *Cancer*, vol. 75, no. 7, pp. 1619–1626, 1995.
- [4] M. L. Giger, N. Karssemeijer, and S. G. Armato III, “Computer-aided diagnosis in medical imaging,” *IEEE Transactions on Medical Imaging*, vol. 20, no. 12, pp. 1205–1208, 2001.
- [5] R.-F. Chang, W.-J. Wu, C.-C. Tseng, D.-R. Chen, and W. K. Moon, “3-D snake for US in margin evaluation for malignant breast tumor excision using mammatome,” *IEEE Transactions on Information Technology in Biomedicine*, vol. 7, no. 3, pp. 197–201, 2003.
- [6] H. Kobatake, M. Murakami, H. Takeo, and S. Nawano, “Computerized detection of malignant tumors on digital mammograms,” *IEEE Transactions on Medical Imaging*, vol. 18, no. 5, pp. 369–378, 1999.
- [7] L. Bocchi, G. Coppini, J. Nori, and G. Valli, “Detection of single and clustered microcalcifications in mammograms using fractals models and neural networks,” *Medical Engineering & Physics*, vol. 26, no. 4, pp. 303–312, 2004.
- [8] H. D. Li, M. Kallergi, L. P. Clarke, V. K. Jain, and R. A. Clark, “Markov random field for tumor detection in digital mammography,” *IEEE Transactions on Medical Imaging*, vol. 14, no. 3, pp. 565–576, 1995.
- [9] L. M. Bruce and R. R. Adhami, “Classifying mammographic mass shapes using the wavelet transform modulus-maxima method,” *IEEE Transactions on Medical Imaging*, vol. 18, no. 12, pp. 1170–1177, 1999.
- [10] C. A. Peña-Reyes and M. Sipper, “A fuzzy-genetic approach to breast cancer diagnosis,” *Artificial Intelligence in Medicine*, vol. 17, no. 2, pp. 131–155, 1999.
- [11] L. Zheng and A. K. Chan, “An artificial intelligent algorithm for tumor detection in screening mammogram,” *IEEE Transactions on Medical Imaging*, vol. 20, no. 7, pp. 559–567, 2001.
- [12] A. E. Hassanien and J. M. H. Ali, “Enhanced rough sets rule reduction algorithm for classification digital mammography,” *Journal of Intelligent Systems*, vol. 13, no. 2, pp. 151–171, 2004.
- [13] R. Swiniarski and H. K. Lim, “Independent component analysis, principal component analysis and rough sets in hybrid mammogram classification,” in *Proceedings of the International Conference on Image Processing, Computer Vision, and Pattern Recognition (ICCV ’06)*, Las Vegas, Nev, USA, June 2006.
- [14] I. Abdel-Qader, L. Shen, C. Jacobs, F. Abu Amara, and S. Pashaie-Rad, “Unsupervised detection of suspicious tissue using data modeling and PCA,” *International Journal of Biomedical Imaging*, vol. 2006, Article ID 57850, 11 pages, 2006.
- [15] L. A. Zadeh, “Fuzzy logic,” *Computer*, vol. 21, no. 4, pp. 83–93, 1988.
- [16] H. H. Yang, S.-I. Amari, and A. Cichocki, “Information-theoretic approach to blind separation of sources in non-linear mixture,” *Signal Processing*, vol. 64, no. 3, pp. 291–300, 1998.
- [17] I. Christoyianni, A. Koutras, E. Dermatas, and G. Kokkinakis, “Computer aided diagnosis of breast cancer in digitized mammograms,” *Computerized Medical Imaging and Graphics*, vol. 26, no. 5, pp. 309–319, 2002.
- [18] M. Bartlett, M. Lades, and T. Sejnowski, “Independent component representation for face recognition,” in *Human Vision and Electronic Imaging III*, vol. 3299 of *Proceedings of SPIE*, pp. 528–539, San Jose, Calif, USA, January 1998.
- [19] S. Amari, A. Cichocki, and H. Yang, “A new learning algorithm for blind source separation,” in *Advances in Neural Information Processing*, vol. 8, pp. 757–763, MIT Press, Cambridge, Mass, USA, 1996.
- [20] R. Martín-Clemente and J. I. Acha, “New equations and iterative algorithm for blind separation of sources,” *Signal Processing*, vol. 82, no. 6, pp. 861–873, 2002.

Research Article

Breast Tumor Simulation and Parameters Estimation Using Evolutionary Algorithms

Manu Mital and Ramana M. Pidaparti

Department of Mechanical Engineering, Virginia Commonwealth University, Richmond, VA 23284, USA

Correspondence should be addressed to Ramana M. Pidaparti, rmpidaparti@vcu.edu

Received 20 September 2007; Revised 7 December 2007; Accepted 20 February 2008

Recommended by Ewa Pietka

An estimation methodology is presented to determine the breast tumor parameters using the surface temperature profile that may be obtained by infrared thermography. The estimation methodology involves evolutionary algorithms using artificial neural network (ANN) and genetic algorithm (GA). The ANN is used to map the relationship of tumor parameters (depth, size, and heat generation) to the temperature profile over the idealized breast model. The relationship obtained from ANN is compared to that obtained by finite element software. Results from ANN training/testing were in good agreement with those obtained from finite element model. After ANN validation, GA is used to estimate tumor parameters by minimizing a fitness function involving comparing the temperature profiles from simulated or clinical data to those obtained by ANN. Results show that it is possible to determine the depth, diameter, and heat generation rate from the surface temperature data (with 5% random noise) with good accuracy for the 2D model. With 10% noise, the accuracy of estimation deteriorates for deep-seated tumors with low heat generation. In order to further develop this methodology for use in a clinical scenario, several aspects such as 3D breast geometry and the effects of nonuniform cooling should be considered in future investigations.

Copyright © 2008 M. Mital and R. M. Pidaparti. This is an open access article distributed under the Creative Commons Attribution License, which permits unrestricted use, distribution, and reproduction in any medium, provided the original work is properly cited.

1. Introduction

Breast cancer, which is common among women, is an international concern. There are about 200 000 cases a year, and it is estimated that there are more than 1 million women with undetected breast cancer. Among various techniques to detect breast cancer, infrared (IR) imaging has been widely used since the late 1950's. In general, the temperature of the human body on the surface of the skin depends on the metabolic activity, the blood flow, and the temperature of the surroundings. Any abnormality in the tissue, such as the presence of a tumor, alters the normal temperature on the skin surface due to increased metabolic activity of the tumor. Therefore, abnormal skin temperature profiles are an indication of diseases such as mastitis, benign tumors, fibrocystic breast disease, and cancer. Lawson [1] was the first to propose the use of thermographic detection of breast cancer, when he observed that the local temperatures of the skin over a tumor were significantly higher (about 2-3 degrees) than normal skin temperatures. Lawson and Chughtai [2] established that

the regional temperature difference over an embedded tumor was due to convection effects associated with increased blood perfusion, and increased metabolism around the tumor.

Thermography, also known as thermal or infrared imaging, is a procedure to determine if an abnormality is present in the breast tissue surface temperature distribution. This abnormality in temperature distribution might indicate the presence of an embedded tumor. Amalu [3] and Keyserlingk et al. [4] have reviewed the role of infrared thermography with respect to the role of IR imaging in the detection of breast cancer and risk indicator. They [3, 4] concluded that the IR imaging has a significant role to play in breast cancer screening due to its ability to image metabolic aspects of the breast and along with sensitivity, specificity, and prognostics. Further aspects of IR imaging techniques of breast cancer and detection methods from infrared images are described in detail and compiled in a recent book by Diakides and Bronzino [5].

In order to complement the IR imaging techniques of breast tumor detection, models have been proposed to

estimate the temperature distributions over breast with and without tumors. For example, Sudarshan et al. [6] studied the temperature distributions in breast cancer by considering a two-dimensional model first proposed by Romrel and Bland [7]. In this model, Pennes bioheat equation was used to describe the flow of thermal energy. The breast model consisted of a subcutaneous fat layer, followed by a gland layer and a deep muscle layer adjacent to the thoracic wall. Using this model, the effects of the tumor size, depth, and the blood perfusion rate on the surface temperature magnitude and profile were determined. Evolutionary algorithms based on neural networks and genetic algorithms have been proposed to detect abnormalities in several applications (such as ECG, tomography, ultrasound); see, for example, Diakides and Bronzino [5]. Recently, Mital and Scott [8] developed a method to determine parameters of an embedded heat source representing a tumor using infrared imaging. It appears that based on literature there are no methods available to estimate the tumor parameters based on the temperature distribution obtained from IR imaging techniques.

The objective of this study is the development of a methodology to estimate the depth, size, and heat generation rate of an embedded tumor in the breast, based on temperature profile on the surface that may be obtained by infrared thermography. This study differs from other works related to breast cancer in that inverse methods are used in the estimation methodology. The methodology is demonstrated with a simple model in order to illustrate the details of the procedures involved. Several cases of various embedded tumor conditions were presented to illustrate the generality of the method.

2. Estimation Methodology and Procedure

The estimation methodology involves evolutionary algorithms using artificial neural network (ANN) and genetic algorithm (GA) as shown in Figure 1. The ANN is used to map the relationship of tumor depth, tumor size, and the heat generation to the temperature profile over the idealized breast model. The relationship obtained from ANN is compared and validated to that obtained by standard numerical model-based finite element analysis software (ANSYS). GA is used to estimate the tumor parameters (depth, size, and heat generation) by minimizing a fitness function involving the temperature profiles obtained from simulated or clinical data to those obtained by ANN. The fitness function is given as a sum of the squares' function that relates the data from the observed thermographic temperature profile to the temperature profile for a given set of estimated parameters. It is defined as

$$S = [\mathbf{Y} - \mathbf{T}(\boldsymbol{\beta})]^T [\mathbf{Y} - \mathbf{T}(\boldsymbol{\beta})], \quad (1)$$

where \mathbf{Y} and \mathbf{T} are vectors containing the observed and estimated temperatures, respectively, and superscript T denotes the transpose of the vector. The observed temperature vector \mathbf{Y} contains surface temperatures that would be obtained

experimentally from thermal imaging. The estimated temperatures contained in vector \mathbf{T} are obtained by the outputs of the trained neural network model using estimates for the unknown parameters (from the *population* pool of the GA). The vector containing the estimates for unknown parameters is denoted by $\boldsymbol{\beta}$. In this study, the unknown parameter vector $\boldsymbol{\beta}$ contains the depth, diameter, and the heat generation rate of the source. Once the objective function was formulated, the estimation scheme using GA was used to determine the unknown parameters.

3. Artificial Neural Network Model to Map Breast Temperature Profiles

A multilayer feed-forward ANN with backpropagation learning algorithm is developed to represent the surface temperature profile of the breast as a function of depth, diameter, and heat generation rate of the tumor. The network is developed with the MATLAB Neural Network Toolbox using the "newff" function. The learning rate was set reasonably low at 0.05 to ensure convergence of the algorithm. There are many transfer functions available in MATLAB software. After some experimentation, the "logsig" transfer function was chosen for the hidden layers and the output neurons, due to nature of the desired outputs. A schematic of the network is shown in Figure 2. The network has 3 input nodes for the three parameters, and 31 output nodes that define one half of the symmetrical temperature profile on the skin surface. There are 2 hidden layers in the network, the first with 21 nodes, and the second with 19 nodes. This configuration was reached after a few iterations of a single hidden layer network proved to give less than adequate results. Two layer deep-nested loops were used in an exhaustive search that varied the number of neurons in the first and second hidden layers, and found the appropriate combination (21-19) that best trained the network. Therefore, a 3-21-19-31 neural network architecture was developed and trained and tested to validate the model. More details about the neural networks and their concepts can be found in Russell and Norvig [9].

In this study, a simplified 2D model of the cross-section of the breast similar to that used by Sudershan et al. [6] was considered, as shown in Figure 3. The Pennes bioheat equation has to be solved to estimate the temperature distribution over the breast model. Due to the complexity of the breast geometry, there are no known analytical solutions to the bioheat equation. Therefore, solutions are usually obtained using computational techniques such as the finite element method. A finite element model created using a commercially available finite element package, ANSYS, solves the Pennes bioheat equation to find the surface temperatures, and this information is used in training/validating ANN model. In this study, the breast is assumed to be of 0.072 m radius hemispherical shape, with a subcutaneous fat layer of 0.005 m uniform thickness, followed by gland, muscle, and the thoracic wall. The tumor is situated symmetrically in the gland layer and assumed to be circular in shape for simplicity. Note that the entire breast is modeled even though the 2D geometry is symmetrical about the Y axis. This is done

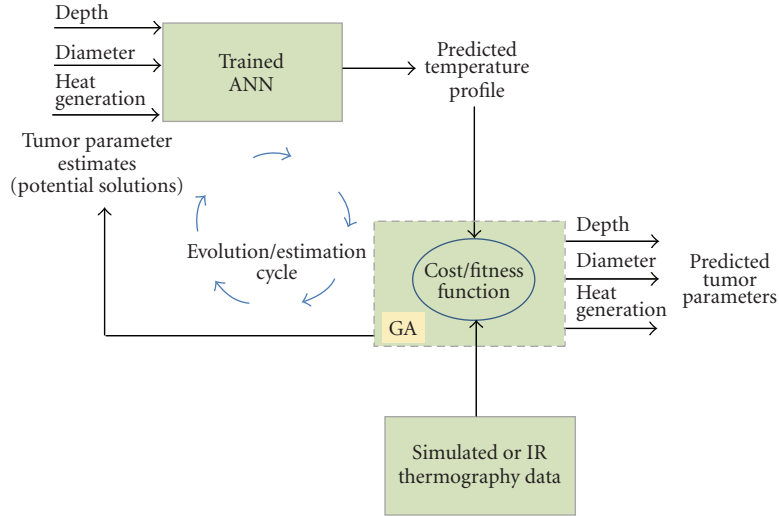


FIGURE 1: Overall estimation methodology for prediction of breast tumor parameters.

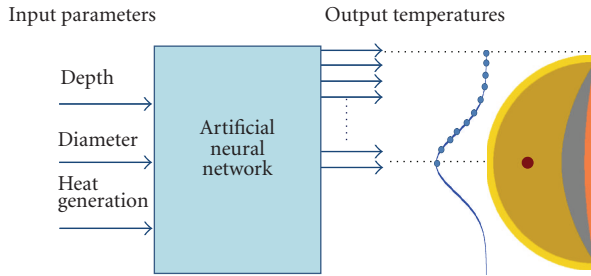


FIGURE 2: Schematic of the neural network.

for future studies where an offcenter tumor location may be considered. The heat transfer in each layer is governed by (1). The values of thermal conductivity, metabolic heat generation rate, and the perfusion source term for each layer, adopted from Werner and Buse [10], are presented in Table 1. The thoracic wall is assumed to be maintained at a constant core body temperature of 37°C. Based on estimate by Osman and Afify [11], the surface of the breast is subjected to a combined heat transfer coefficient (convection, radiation, and evaporation) of 13.5 W/m²-K, a reasonable value in the absence of forced convection. The clinical environment under which the thermographic measurements are made is assumed to be at a constant temperature of 21°C.

Using the finite element analysis of the breast model, a total of 17 different cases were analyzed and used for training the ANN. The inputs parameters are scaled between 0 and 1 using upper and lower bounds for each parameter. The diameter of the tumor is allowed to vary between 0.005 and 0.015 m so that it is in mammary gland region. The bounds for depth are 0.014 and 0.041 m (based on the assumption that the tumor will most likely be present in the gland). The lower and upper bounds on the heat generation rate of the tumor are 20 times (14,000 W/m³) and 100 times (70,000 W/m³) that of normal tissue. The output surface

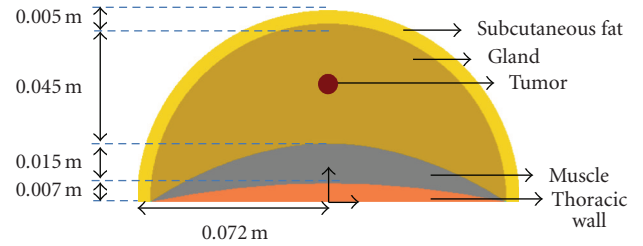


FIGURE 3: A 2D model of the breast based on Sudershan et al. [6].

temperatures of the network are scaled values between 0 and 1, using a lower limit of 26°C and upper limit of 33°C. The network was trained for 400 epochs or training cycles using the data generated from finite element analysis results. Three different cases were used for validating the trained network.

4. Genetic Algorithms in Breast Tumor Parameters Estimation

In the implementation of the GA, the potential solution (*chromosome*) contains the depth, diameter, and the tumor heat generation rate as the 3 *genes* and 10 *bits* are used to represent the value of each *gene* in binary format. Therefore, each *chromosome* has 30 bits. The *population* size has been chosen to be 20. The initial *population* pool was generated using a random number generator.

The parameters contained in each *chromosome* are changed from their binary representation to floating point representation using (for the *i*th parameter)

$$P_i = a + \frac{b - a}{2^{nb} - 1}(m), \quad (2)$$

where P_i is the decimal value of *i*th parameter, a and b are the lower and upper limits of the search interval, respectively, nb is the number of bits used to represent the parameter (e.g., 10 in this case), and m is the decimal value of the parameter

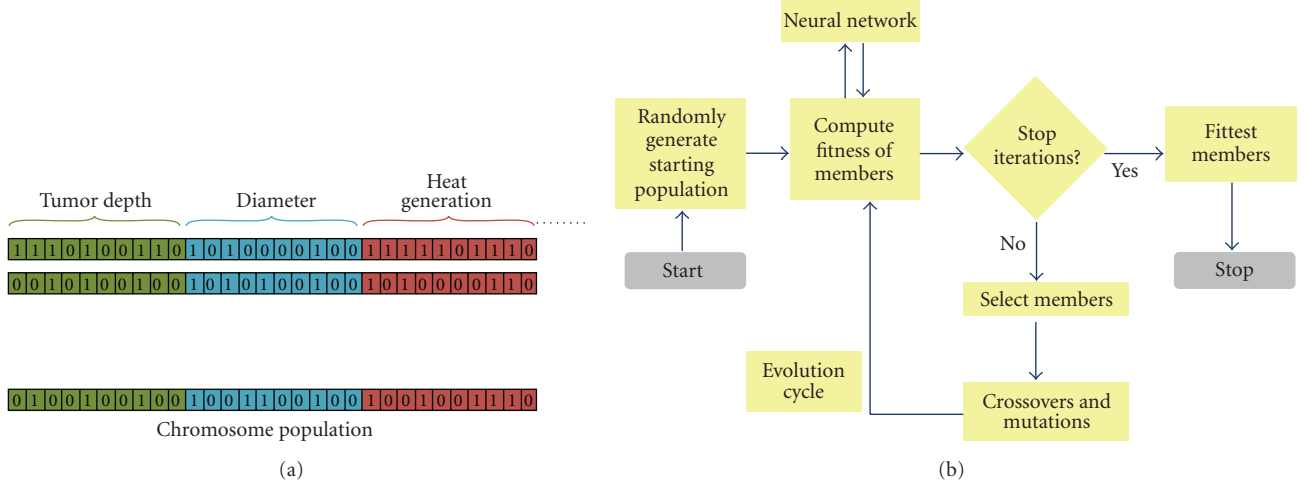


FIGURE 4: Flowchart of the GA estimation procedure.

TABLE 1: Values of thermal conductivity, metabolic heat generation, and perfusion term.

Layer	Thermal conductivity (W/m-K)	Metabolic heat generation (W/m ³)	Perfusion (W/ m ³ -C)
Subcutaneous fat	0.21	400	800
Gland	0.48	700	2400
Muscle	0.48	700	2400
Tumor	0.48	14000–70000	48000

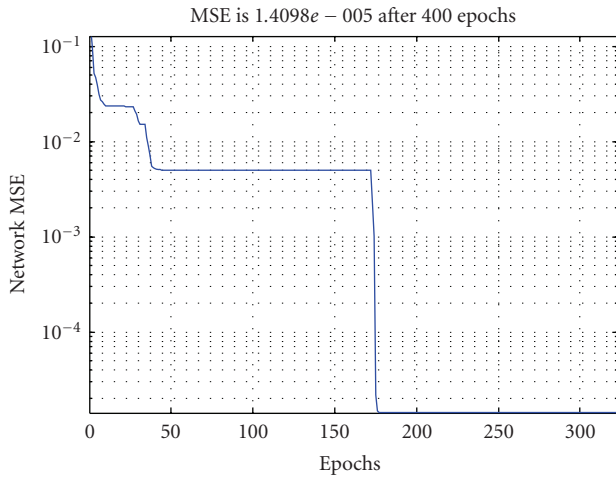


FIGURE 5: Convergence plot with mean squared error of the network output during training.

in binary form. The lower limit a and upper limit b for each of the three parameters were mentioned earlier.

The *fitness* of each *chromosome* is evaluated using the sum of the squares objective function given by (2). The *fitness* f of a *chromosome* is related to the sum of the squares function using

$$f = S_{\text{Max}} - S(\beta), \quad (3)$$

where S_{MAX} was arbitrarily chosen to be 10 so it always stays greater than the maximum value of sum of squares possible,

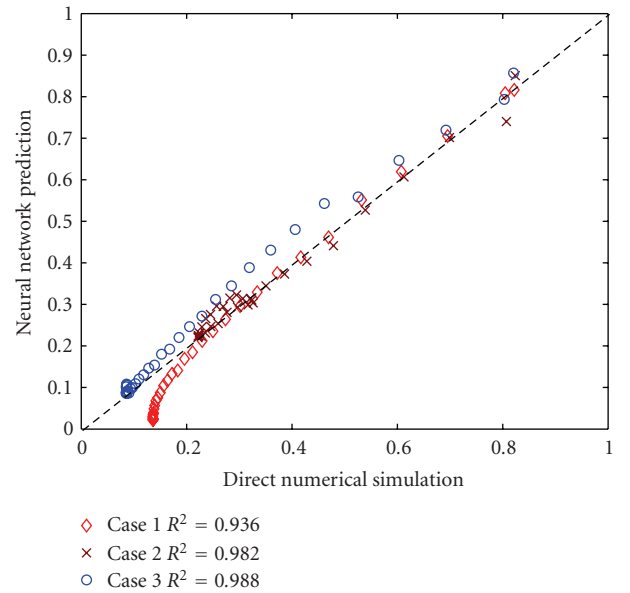


FIGURE 6: Comparison of output of trained ANN with finite element simulation.

and S is the sum of the squares generated using a parameter set (*chromosome*) β .

The *fitness* is determined for each parameter set (*chromosome*) and then ranked. *Chromosomes* of higher *fitness* are more likely to be selected to reproduce and contribute their genetic material to the next *generation*. A probability of

TABLE 2: Results from parameter estimation procedure to determine embedded tumor parameters using temperature data with 5% noise.

Case	Run	Actual			Estimated		
		Depth (m)	Diameter (m)	Heat generation (W/m ³)	Depth (m)	Diameter (m)	Heat generation (W/m ³)
1	1	0.015	0.008	25000	0.015	0.007	25440
	2				0.015	0.007	27302
2	1	0.015	0.012	40000	0.014	0.011	39126
	2				0.015	0.012	39619
3	1	0.035	0.008	25000	0.035	0.008	27028
	2				0.034	0.007	28396
4	1	0.035	0.012	40000	0.036	0.011	40330
	2				0.036	0.012	42082

TABLE 3: Results from parameter estimation procedure to determine embedded tumor parameters using temperature data with 10% noise.

Case	Run	Actual			Estimated		
		Depth (m)	Diameter (m)	Heat generation (W/m ³)	Depth (m)	Diameter (m)	Heat generation (W/m ³)
1	1	0.015	0.008	25000	0.016	0.007	23689
	2				0.014	0.010	21000
2	1	0.015	0.012	40000	0.015	0.012	39000
	2				0.014	0.011	40987
3	1	0.035	0.008	25000	0.040	0.010	20130
	2				0.039	0.010	20980
4	1	0.035	0.012	40000	0.037	0.012	35622
	2				0.038	0.014	36428

mutation (random changing of a *chromosome*) of 0.10 and a probability of *crossover* (formation of *children*) equal to 0.90 are used to determine how members of the *population* will reproduce to bring forth the next *generation*. A flowchart of the solution method is presented in Figure 4. More details about GA procedures and applications can be found in Goldberg [12] and Davis [13].

Several cases were simulated in order to validate the ability of the estimation procedure to accurately predict the depth, size, and heat generation rate of the embedded tumor. For each parameter set, two runs of the GA were conducted by introducing 5% and 10% noises in the simulation data to see the sensitivity of the prediction of breast tumor parameters.

5. Results and Discussion

A convergence plot of the mean squared error of the neural network output during training is shown in Figure 5. In general, the results obtained from ANN training were in good agreement with those obtained from finite element analysis model. After the ANN is trained, the network is validated for three different cases as shown in Figure 6. It can be seen from Figure 6 that, for each validation case, the output of the neural network model shows good agreement with the simulation results with R^2 values of 0.936, 0.982, and 0.988, respectively. To further validate the ANN results, the temperature profiles obtained for a specific case 3 (depth of 0.029 m, diameter of 0.008 m, and heat generation of 30000 W/m³) are compared with the finite element and ANN

models as shown in Figure 7. Once again a good comparison is seen.

The parameter estimates for the depth, diameter, and heat generation rate of the tumor for the four cases, corresponding to 5% and 10% random noise in the temperature rise on the skin surface, are presented in Tables 2 and 3, respectively. MATLAB built in function “*rand*” was used for generating random noise in the temperature rise on the skin surface. For each case, the GA was run twice with different random initial populations yielding similar results. With 5% random noise, the results show good agreement between actual and predicted parameters. In this case, the absolute errors in depth and size were within 0.001 m, and absolute errors in heat generation rate were within 3000 W/m³. With 10% noise, the accuracy of the estimated parameters deteriorates for deep seated tumors with low heat generation rate. In this case, the absolute errors in depth were within 0.005 m, error in size within 0.002 m, and in heat generation rate within 4870 W/m³.

6. Conclusions

An estimation methodology-based evolutionary algorithm using neural networks and genetic algorithms was developed to estimate the breast tumor parameters based on surface temperature profile that may be obtained by infrared thermography. The methodology is demonstrated with a simple model in order to illustrate the details of the procedures involved. For the cases studied, results from simulations show that it is possible to determine the depth, diameter, and

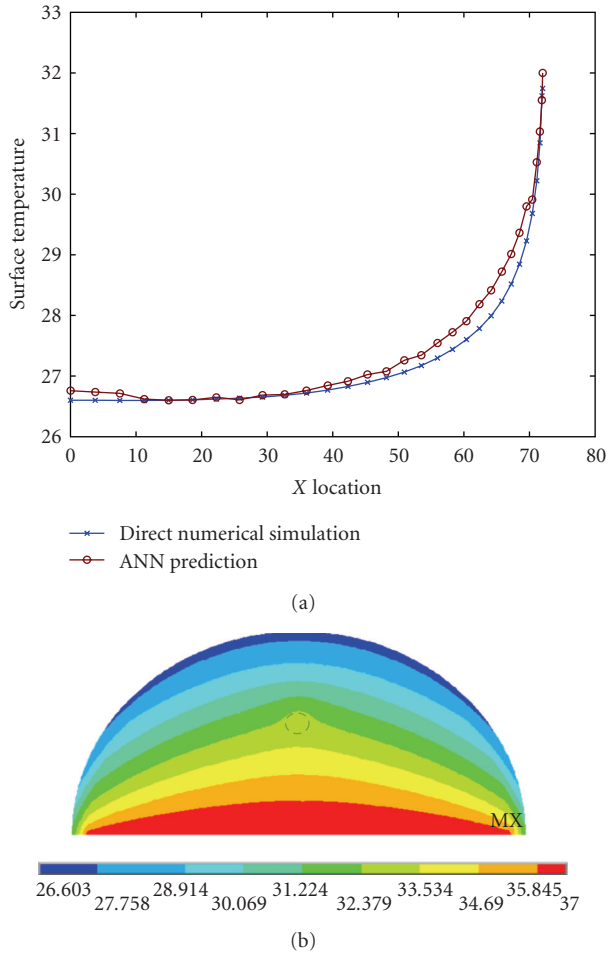


FIGURE 7: Comparison of temperature profile of trained ANN with direct numerical simulation.

heat generation rate from the surface temperature data (with 5% random noise) with good accuracy for the simplified 2D model. With 10% noise, the accuracy of the estimated parameters deteriorates for deep-seated tumors with low heat generation rate. With the recent advances in the accuracy of IR images and noise reduction techniques, it may be possible to reduce noise to within acceptable levels (5%) for the methodology to be effective. In general, the breast shape is complex, and this should be considered for realistic studies. However, the estimation methodology is general and can be applied even to realistic breast geometry. This may increase the computation time but the methodology can be easily extended. In order to further develop the proposed methodology so that it can be used in a clinical scenario, several aspects such as complexities of 3D breast geometry and the effects of nonuniform cooling should be considered in future investigations.

References

[1] R. N. Lawson, "Implications of surface temperatures in the diagnosis of breast cancer," *Canadian Medical Association Journal*, vol. 75, no. 4, pp. 309–310, 1956.

[2] R. N. Lawson and M. S. Chughtai, "Breast cancer and body temperatures," *Canadian Medical Association Journal*, vol. 88, pp. 68–70, 1963.

[3] W. C. Amalu, "A Review of Breast Thermography," International Academy of Clinical Thermology, 2003.

[4] J. Keyserlingk, P. Ahlgren, E. Yu, N. Belliveau, and M. Yassa, "Functional infrared imaging of the breast," *IEEE Engineering in Medicine and Biology Magazine*, vol. 19, no. 3, pp. 30–41, 2000.

[5] N. A. Diakides and J. D. Bronzino, *Medical Infrared Imaging*, CRC Press, Boca Raton, Fla, USA, 2007.

[6] N. M. Sudarshan, E. Y. K. Ng, and S. I. Teh, "Surface temperature distribution of a breast with and without tumour," *Computer Methods in Biomechanics and Biomedical Engineering*, vol. 2, no. 3, pp. 187–199, 1995.

[7] L. J. Romrell and K. I. Bland, "Anatomy of breast, axilla, chest wall, and related metastatic sites," in *The Breast: A Comprehensive Management of Benign and Malignant Diseases*, p. 22, Saunders, Philadelphia, Pa, USA, 1991.

[8] M. Mital and E. P. Scott, "Thermal detection of embedded tumors using infrared imaging," *Journal of Biomechanical Engineering*, vol. 129, no. 1, pp. 33–39, 2007.

[9] P. Russell and P. Norvig, *Artificial Intelligence: A Modern Approach*, Prentice Hall, Upper Saddle River, NJ, USA, 1995.

[10] J. Werner and M. Buse, "Temperature profiles with respect to inhomogeneity and geometry of the human body," *Journal of Applied Physiology*, vol. 65, no. 3, pp. 1110–1118, 1988.

[11] M. M. Osman and E. M. Afify, "Thermal modeling of the normal woman's breast," *Journal of Biomechanical Engineering*, vol. 106, no. 2, pp. 123–130, 1984.

[12] D. E. Goldberg, *Genetic Algorithms in Search, Optimization and Machine Learning*, Addison-Wesley, Reading, Mass, USA, 1989.

[13] L. Davis, *Handbook of Genetic Algorithms*, Van Nostrand Reinhold, New York, NY, USA, 1991.

Research Article

Hemodynamic Effect of Unequal Anterior Cerebral Artery Flow Rates on the Anterior Communicating Artery Bifurcation: A Computational Fluid Dynamics Study

Thomas Rau,¹ Xing He,² Prem Venugopal,² Fernando Viñuela,²
Gary Duckwiler,² and Daniel J. Valentino²

¹ Department of Radiology, University of Colorado Health Sciences Center, Aurora, CO 80045, USA

² Department of Radiological Sciences, University of California, Los Angeles, CA 90095, USA

Correspondence should be addressed to Thomas Rau, thomas.rau@ucdenver.edu

Received 12 November 2007; Revised 11 June 2008; Accepted 11 December 2008

Recommended by Ewa Pietka

Computational fluid dynamics techniques were used to investigate the hemodynamic effect of unequal anterior cerebral artery flow rates on the anterior cerebral and anterior communicating artery (ACA-ACOM) bifurcation. Hemodynamics have long been implicated as a major factor in cerebrovascular disease. Using an idealized 2D symmetric model of the ACA-ACOM geometry, the flow field and wall shear stress (WSS) at the bifurcation regions are assessed for pulsatile inflows with left to right flow ratios of 1:1, 2:1, 3:1, and 4:1. Unequal flow rates through the ACA parent arteries result in bifurcation of the higher flow parent stream and a shifting of the impingement points along the A2-ACOM adjoining wall toward the contralateral ACA. Cross-flow through the ACOM is generally unstable and results in increased WSS at the impingement region from the higher flow parent artery and a double amplitude peak in the WSS at the contralateral bifurcation region from local recirculation effects. These results suggest that asymmetry in ACA flow rates result in increased hemodynamic stresses at the ACA-ACOM bifurcation regions and suggest a possible factor for vessel weakening and aneurysm formation.

Copyright © 2008 Thomas Rau et al. This is an open access article distributed under the Creative Commons Attribution License, which permits unrestricted use, distribution, and reproduction in any medium, provided the original work is properly cited.

1. Introduction

Numerous investigations on the hemodynamics in the Circle of Willis have been performed to elucidate the pathogenesis of aneurysm formation. It is known that over 85% of aneurysms occur in the anterior circulation and form predominantly at the apex of vessel bifurcations and around sharp bends. It is at these locations where hemodynamic stresses are the greatest and the structural protein assembly of the muscular layer of the vessel wall is most underdeveloped [1]. A generally accepted theory is that an anomalous response of the vascular endothelium to oscillating wall shear stresses leads to progressive and unstable degradation of the arterial wall and consequent aneurysm formation [2]. The validity and reliability of computational methods to model the hemodynamic processes has motivated numerous computational flow studies to characterize the flow patterns and wall shear stresses associated with pulsatile flows in these susceptible regions [3–9].

The junction of the anterior cerebral (ACA) and anterior communicating (ACOM) arteries represents a unique and complex vascular geometry with two closely apposed bifurcations (see Figure 1). Studies in the past have shown that a strong association exists between the development of aneurysms and their neck sizes at the ACOM junction with the dominant A1 parent artery feeder [10]. In this study, a computational fluid dynamics (CFD) simulation was performed on an idealized 2D symmetric model of the ACA and ACOM bifurcation to investigate the hemodynamic effect of unequal flow rates through the A1 ACA segments. Simulations were run with left to right inflow ratios fixed at 1:1, 2:1, 3:1, and 4:1. The overall flow patterns as well as the wall shear stress (WSS) at various points along the adjoining wall between the A2 and ACOM segments are analyzed spatially and temporally near the impingement points where aneurysms are predicted to occur. Unequal left-right A1 flow rates can occur whenever the total upstream flow resistances are not equal bilaterally. Clinically, this may

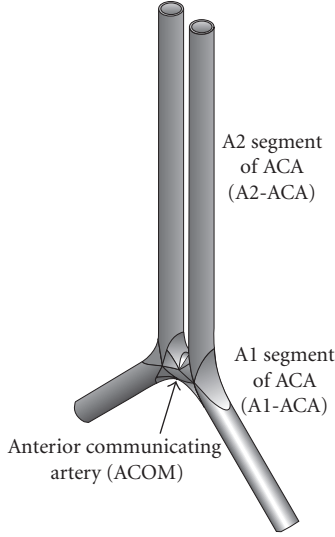


FIGURE 1: A 3D model depiction of the anterior cerebral circulation upon which the simulation is based.

occur with unilateral high grade stenotic lesions in upstream vessels to the Circle of Willis. This might be seen after a thromboembolic event in stroke victims and succeeding vasospasm in upstream arteries or the existence of a congenital hypoplastic A1-ACA. Asymmetric flow rates between the A1 segments can also occur transiently by iatrogenic means during a rapid intravenous infusion of contrast media during diagnostic cerebral angiography. This study attempts to characterize some hemodynamic stress pattern differences which may occur under these circumstances.

2. Methods

A 2D symmetric model of the ACA and ACOM was constructed using the Solidworks [11] software seen in Figure 2. The diameter was assigned a unit length of 1, and all other dimensions were scaled accordingly and proportioned from other studies [12, 13]. The bifurcation angle from the A1 to A2 segments of the anterior cerebral arteries was chosen to be 45 degrees, within the range of clinical models. The radii of curvature adjoining the walls of the A1 to the A2 and ACOM segments were chosen such that a smooth transition was made. The model was then imported into FLUENT's Gambit for meshing. A finer-graded mesh was used at the boundary layer along all wall surfaces to increase the resolution of the gradients near the wall. A total of 196 944 data points were obtained after meshing.

Substitution of the following nondimensional expressions for velocity u and v , length x and y , time t , pressure P , and Reynolds number Re allows us to nondimensionalize the governing equations of continuity and Navier-Stokes in the Cartesian coordinate system. We divide the flow variables with the corresponding references variables denoted by subscript ref to produce the nondimensional variables denoted by $*$. Let ρ be the density of blood, μ the dynamic viscosity of blood, u_{ref} be the reference velocity, and L_{ref} the reference

length, where

$$\begin{aligned} u^* &= \frac{u}{u_{ref}}, & v^* &= \frac{v}{u_{ref}}, \\ x^* &= \frac{x}{L_{ref}}, & y^* &= \frac{y}{L_{ref}}, \\ t^* &= \frac{tu_{ref}}{L_{ref}}, & P^* &= \frac{P}{\rho u_{ref}^2}, \\ Re &= \frac{\rho u_{ref} L_{ref}}{\mu}. \end{aligned} \quad (1)$$

The equations of continuity and Navier-Stokes become [14]

$$\begin{aligned} \frac{\partial u^*}{\partial x^*} + \frac{\partial v^*}{\partial y^*} &= 0, \\ \frac{\partial u^*}{\partial t^*} + u^* \frac{\partial u^*}{\partial x^*} + v^* \frac{\partial u^*}{\partial y^*} &= -\frac{\partial p^*}{\partial x^*} + \frac{1}{Re} \left(\frac{\partial^2 u^*}{\partial x^{*2}} + \frac{\partial^2 u^*}{\partial y^{*2}} \right), \\ \frac{\partial v^*}{\partial t^*} + u^* \frac{\partial v^*}{\partial x^*} + v^* \frac{\partial v^*}{\partial y^*} &= -\frac{\partial p^*}{\partial y^*} + \frac{1}{Re} \left(\frac{\partial^2 v^*}{\partial x^{*2}} + \frac{\partial^2 v^*}{\partial y^{*2}} \right). \end{aligned} \quad (2)$$

The usage of the governing flow equations in this form eliminates dependence on absolute dimensions and makes the simulation dependent only on the Reynold's number. The results obtained can, therefore, be more generalized. Incompressible, Newtonian fluids were assumed in the calculations of the nondimensional Navier-Stokes equations, and the solutions were performed using OpenFOAM software [15]. A minimum Reynold's number of 400 was set by allowing fluid density to be equal 1, scaling the maximum of the velocity profile to 1, and setting fluid viscosity to 0.0025. The Reynold's number was allowed to vary up to 800 by the nature of the pulsatile velocity profile at the 2 inlets. Two-plug flow inlets were assigned at the parent anterior cerebral arteries with the pulse arterial waveform defined by (3). A no-slip and nonelastic condition was imposed on the walls and the outflow boundary was set at a reference pressure of 0. The simulations were allowed to run for three to four complete cycles at 60 beats per minute to achieve convergence of solutions.

Simulations were run with the ratio of the inflow rates between the left and right A1 segments set at 1:1, 2:1, 3:1, and 4:1. This was conducted by decreasing the time-dependent amplitude of the right A1 inflow segment by the appropriate fraction (0.5, 0.33, and 0.25).

The velocity, U , pulse profile used in these simulations was given by

$$\begin{aligned} U(t) &= 8.419 \\ & * \{0.08225 \\ & + 2(-0.013077 \cos(wt) - 0.002868 \sin(wt)) \\ & + 2(0.001125 \cos(2wt) - 0.001625 \sin(2wt)) \\ & + 2(-0.000172 \cos(3wt) + 0.001631 \sin(3wt)) \\ & + 2(-0.001000 \cos(4wt))\}, \end{aligned} \quad (3)$$

where $w = 2\pi/T$, $T = 1$ second.

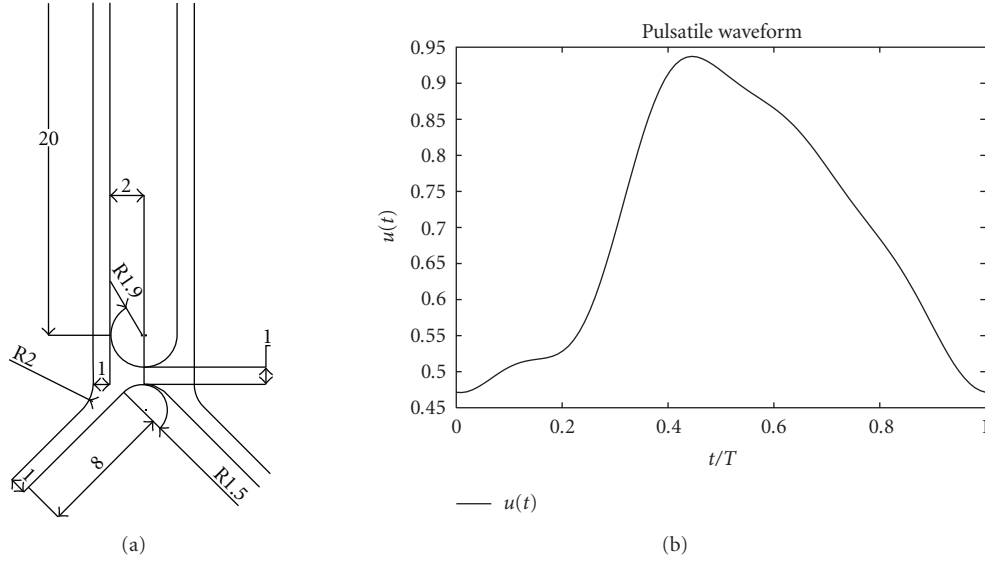


FIGURE 2: (a) ACA-ACom geometry with 45 degree bifurcation angles. (b) Pulse waveform given by (3). The global maximum occurring at $0.45 t/T$ will define the transition between the systolic and diastolic phases of the flow waveform.

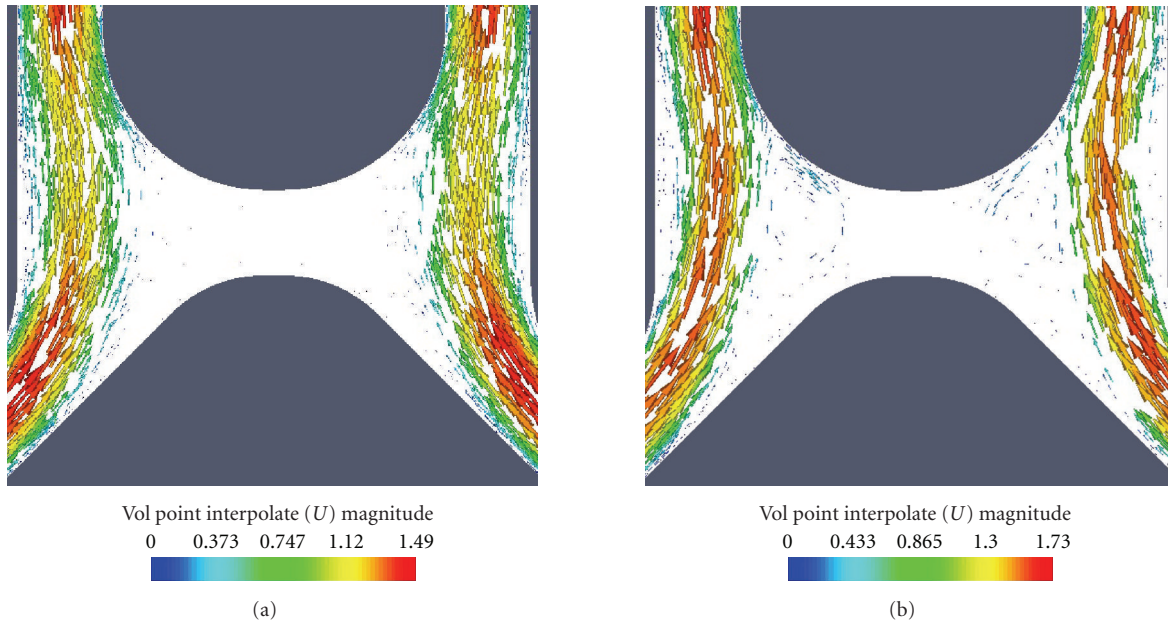


FIGURE 3: Velocity field with equal left and right ACA flow rates ($Q_R = Q_L$) during (a) systole and (b) early diastole. A dead zone in the ACom exists throughout the pulsation cycle. (b) Unsteadiness exists bilaterally at the A2-ACom impingement sites with flow separation and vortices seen during the diastolic phase.

The transition point between the systolic and diastolic phases of the velocity wave form will be defined at the global maximum occurring at $0.45 t/T$.

The wall shear stress (WSS) is obtained with the following equation:

$$\begin{pmatrix} W_x \\ W_y \end{pmatrix} = \mu \begin{pmatrix} 2 \frac{\partial u}{\partial x} & \frac{\partial u}{\partial y} + \frac{\partial v}{\partial x} \\ \frac{\partial u}{\partial y} + \frac{\partial v}{\partial x} & 2 \frac{\partial v}{\partial y} \end{pmatrix} \begin{pmatrix} n_x \\ n_y \end{pmatrix}, \quad (4)$$

where n_x and n_y are the x and y components of the normal vector of vessel wall.

3. Results

The relative inflow rates through the two A1 parent artery segments greatly affect the overall flow pattern and the hemodynamic stresses on the walls at the bifurcation region. When the left-right A1 inflow rates are unequal, bifurcation of the higher velocity parent stream occurs and the ACom

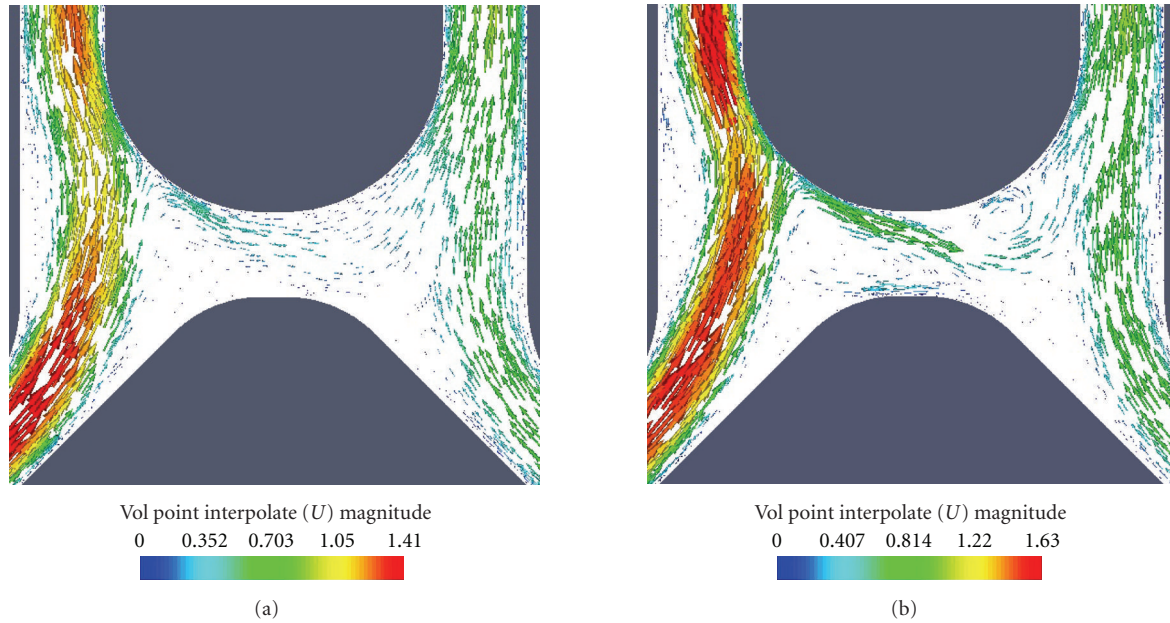


FIGURE 4: (a) Velocity field during systole and (b) early diastole with ACA flow rates set at $Q_R = 0.5Q_L$. Left ACA impingement site moves rightward along the A2-ACOM adjoining wall as compared to the case where $Q_R = Q_L$ with bifurcation of flow into the A2-ACA and ACOM segments. (b) A large vortex is generated on the right bifurcation site during diastole.

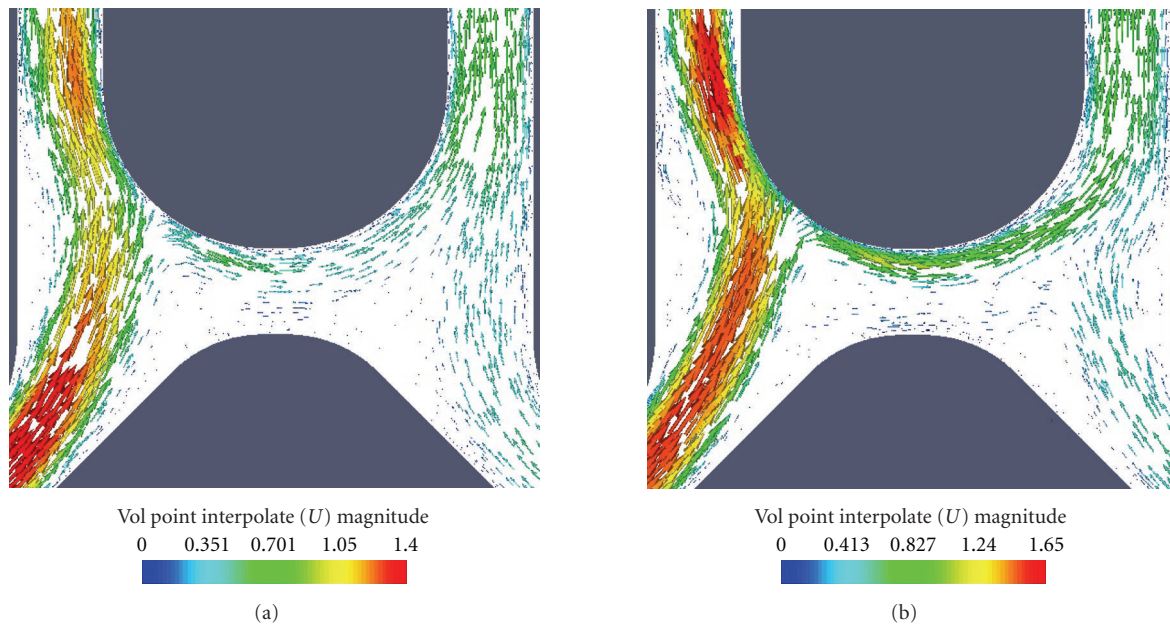


FIGURE 5: (a) Velocity field during systole and (b) early diastole with ACA flow rates set at $Q_R = 0.33Q_L$. Again bifurcation of the A1 parent flow artery into the ACOM and A2 segments is seen. Left ACA impingement site moves further rightward along A2-ACOM adjoining wall compared to that seen in the case where $Q_R = 0.5Q_L$. Flow separation is again seen on the right A2-ACOM impingement site leading to local recirculation effects.

becomes a functional anastomosis. While flow through the A1 and A2 ACA segments is generally laminar, unsteadiness is seen in the ACA-ACOM bifurcation section especially during the deceleration phase of pulsation. Figures 4, 5, and 6 show the bifurcation of the higher flow parent artery streams. The flow through the junction appears more stabilized during the acceleration phase of the pulse cycle.

For equal left-right A1 flow rates, separation and vortex shedding occur at the ACOM junction as the streams bypass the anastomosis into the A2 segment. Thus, while the ACOM is rendered a dead zone, a local unsteady region is created near the impingement site resulting in irregular, low amplitude WSS patterns at the A2-ACOM adjoining wall. Figure 3 shows the bilateral oblique impingement zones of

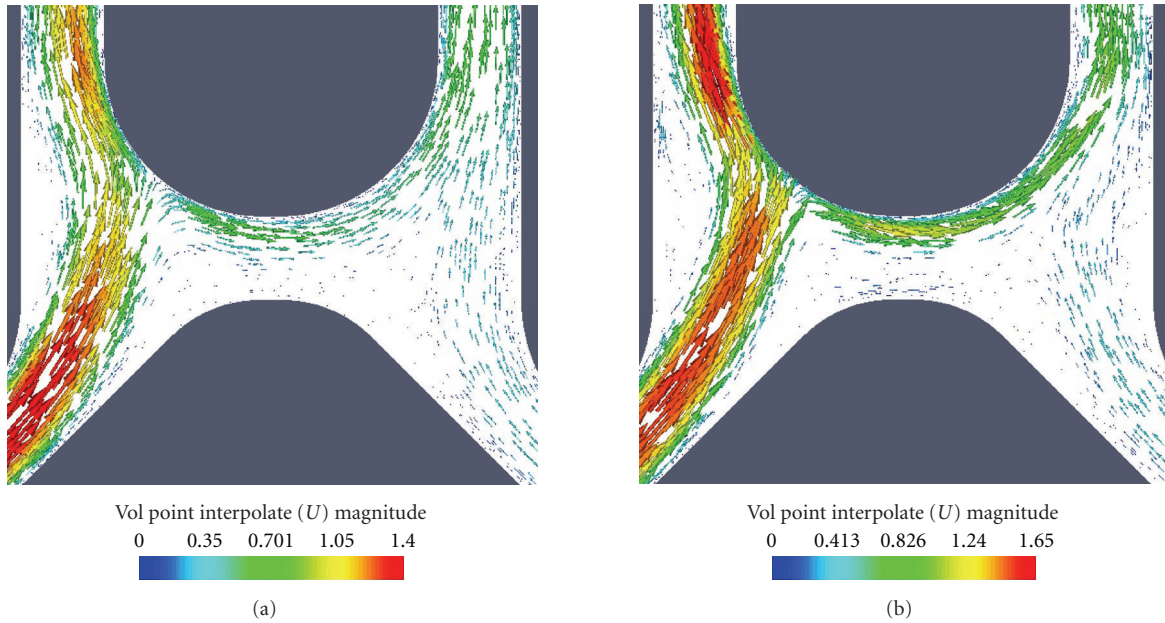


FIGURE 6: (a) Velocity field during systole and (b) early diastole with ACA flow rates set at $Q_R = 0.25Q_L$. Bifurcation of the A1 parent flow artery into the ACOM and A2 segments is again seen. Left ACA impingement site appears to move even further rightward along A2-ACOM adjoining wall compared to that seen in the case where $Q_R = 0.33Q_L$. Flow separation is again seen on the right A2-ACOM impingement site leading to local recirculation effects.

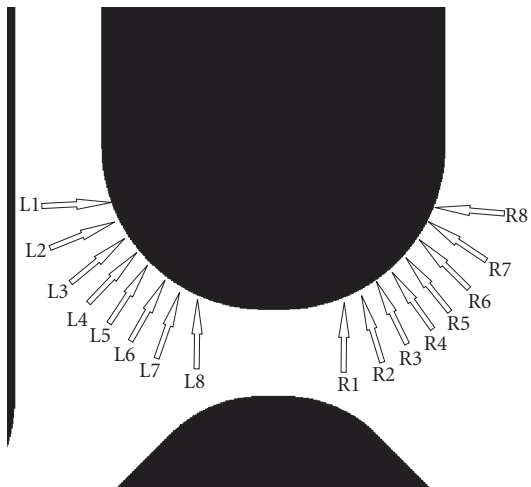


FIGURE 7: Labeled points on the left and the right impingement points in the WSS plots.

the parent A1 segments onto the distal A2-ACOM adjoining wall. The WSS plots in Figures 8 and 12 demonstrate smaller amplitude WSS and gradients compared to the unequal ACA flow rate cases.

As the inflow rate from the right ACA is reduced relatively to the left, the impingement point of the left A1 stream moves toward the contralateral bifurcation along the A2-ACOM adjoining wall segment and is divided. The impingement point is also observed to oscillate toward the contralateral ACA segment during the deceleration phase of the pulsation cycle. The majority of the inflow continues into the A2 segment while the divided fraction enters the ACOM

segment and joins the flow through the right ACA. Flow through the ACOM anastomosis is subject to separation as it negotiates the curvature of the ACOM during the deceleration phase of the pulsation cycle. The flow separation results in a large second peak in time in the WSS plots due to local recirculation effects. The recirculation zone is most apparent in the case where $Q_R = 0.5Q_L$ in Figure 4(b) but can be seen in the other cases at high magnification views (not shown). The magnitude of the second peak appears to increase as the ratio of the left to right flow rates is increased and occurs earlier in the pulsation cycle. Thus, unequal A1 flow rates impose additional stresses on the ACA-ACOM bifurcation region by the degree of unbalanced left-right A1 inflow rates.

The plots of WSS versus time and position are shown in Figures 8, 9, 10, and 11 for the various left to right flow ratios. The positions along the left and right impingement points are denoted by L1-L8 and R1-R8, respectively, and are shown in Figure 7. The plots for unequal left to right flow rates in Figures 9–11 show the double amplitude peak which occurs during the diastolic phase which is absent when the left and right flow rates are equal (see Figure 8). Figure 12 plots WSS versus time for a characteristic point at the left and right impingement regions. Clearly shown in this figure is the double amplitude peak occurring with unequal parent A1 flows and the time between successive peaks as the imbalance between the A1 flows is greater.

4. Discussion

The results demonstrate that the flow behavior and hemodynamic stresses at the ACOM bifurcation are highly

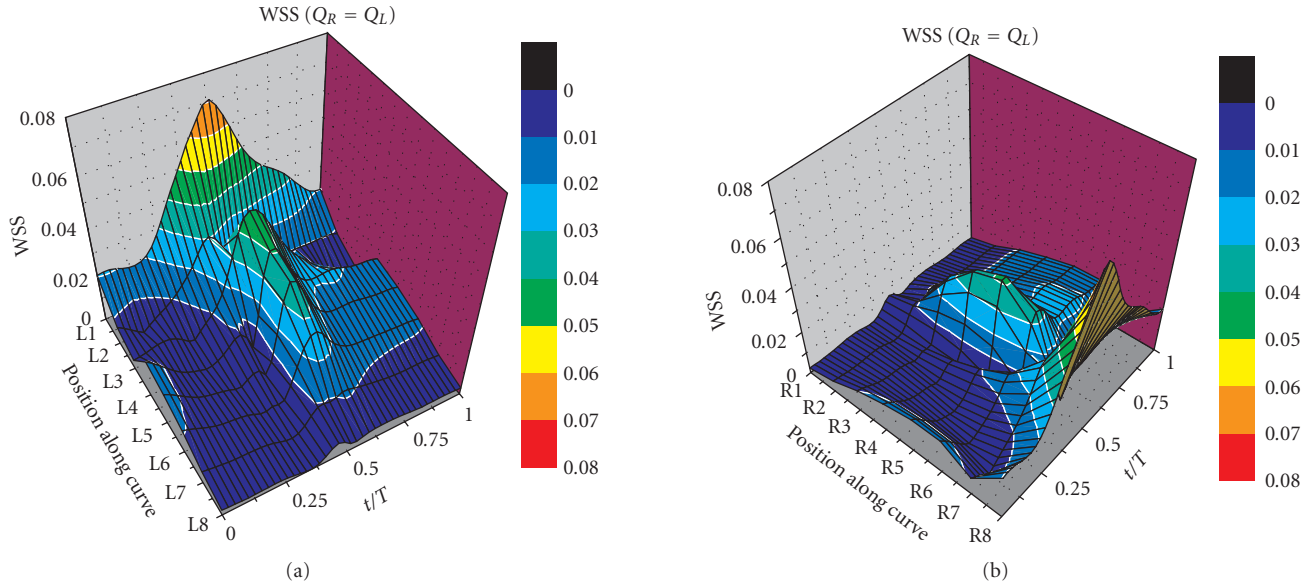


FIGURE 8: WSS versus position and time for $Q_R = Q_L$ on (a) the left and (b) the right bifurcation regions.

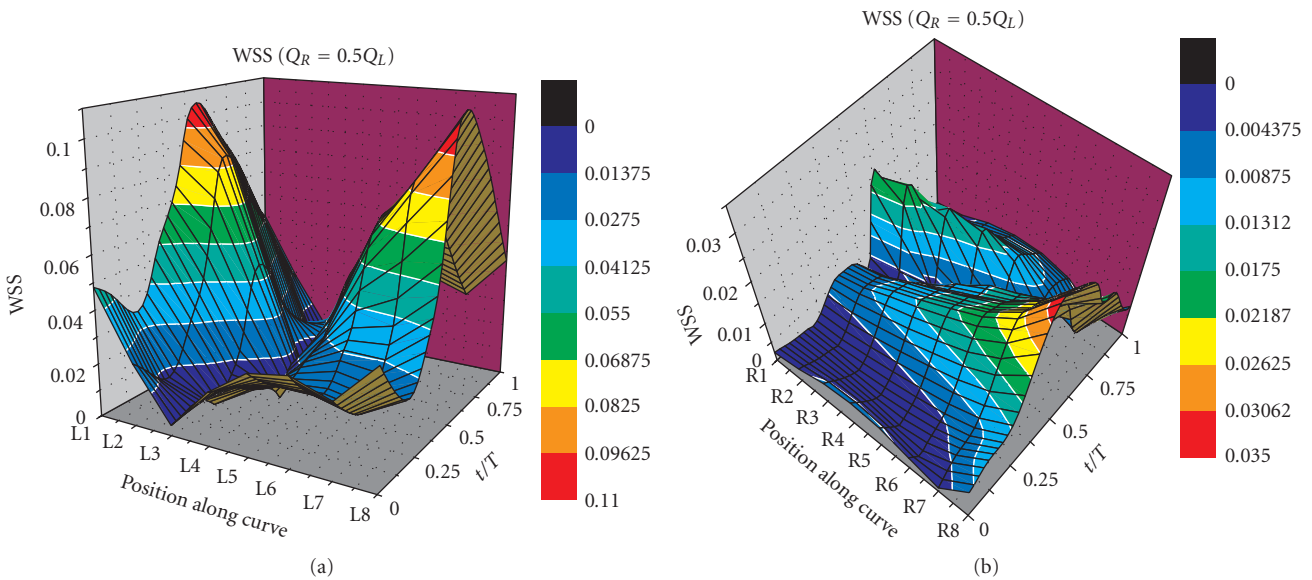


FIGURE 9: WSS versus position and time for $Q_R = 0.5Q_L$ on (a) the left and (b) the right bifurcation regions.

dependent on the relative flow rate ratios between the A1-ACA parent arteries. Asymmetrical flow conditions at the A1 segments in a symmetrical geometry result in bifurcation of the higher flow parent artery into the A2 and ACOM segments. Cross-flow through the ACOM from the higher flow parent artery is generally unstable at the bifurcation regions especially during diastole. Pulsatility creates a cyclically varying region of flow separation and reversal at those locations which change markedly in amplitude throughout the cycle. Bifurcation regions, where these instabilities occur, are sites of large fluctuations in WSS magnitude and are consistent with the location where aneurysms are predicted to develop.

Unequal flow between left-right A1 segments produces a change in the WSS pattern as compared to symmetrical flow conditions. Both an increase in WSS amplitude at the impingement point and a double amplitude peak at the opposite bifurcation region are observed due to local recirculation effects. The impingement sites of the incoming parent artery flow also shift toward the apex of the bifurcation region along the A2-ACOM adjoining wall where the median muscular layer of the arterial wall is least developed [1]. This leads to greater hemodynamic stresses at locations that are least able to withstand them and a possible mechanism for mechanical deformation from cyclic fatigue stresses. Figures 3–6 also demonstrate that as the impingement site

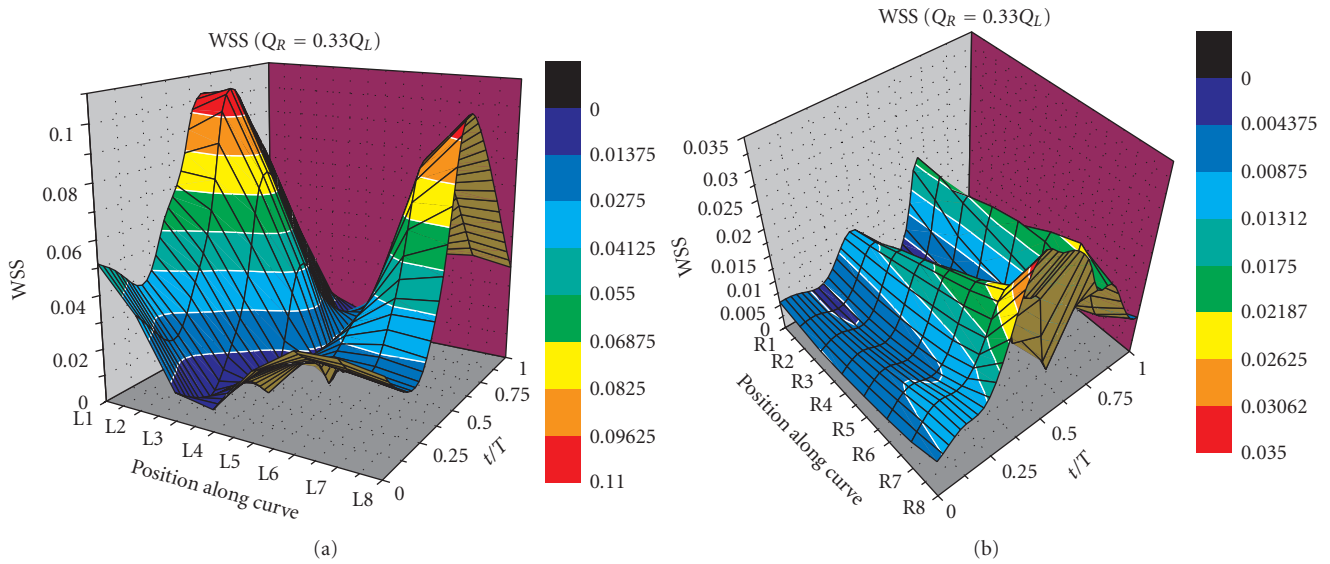


FIGURE 10: WSS versus position and time for $Q_R = 0.33Q_L$ on (a) the left and (b) the right bifurcation regions.

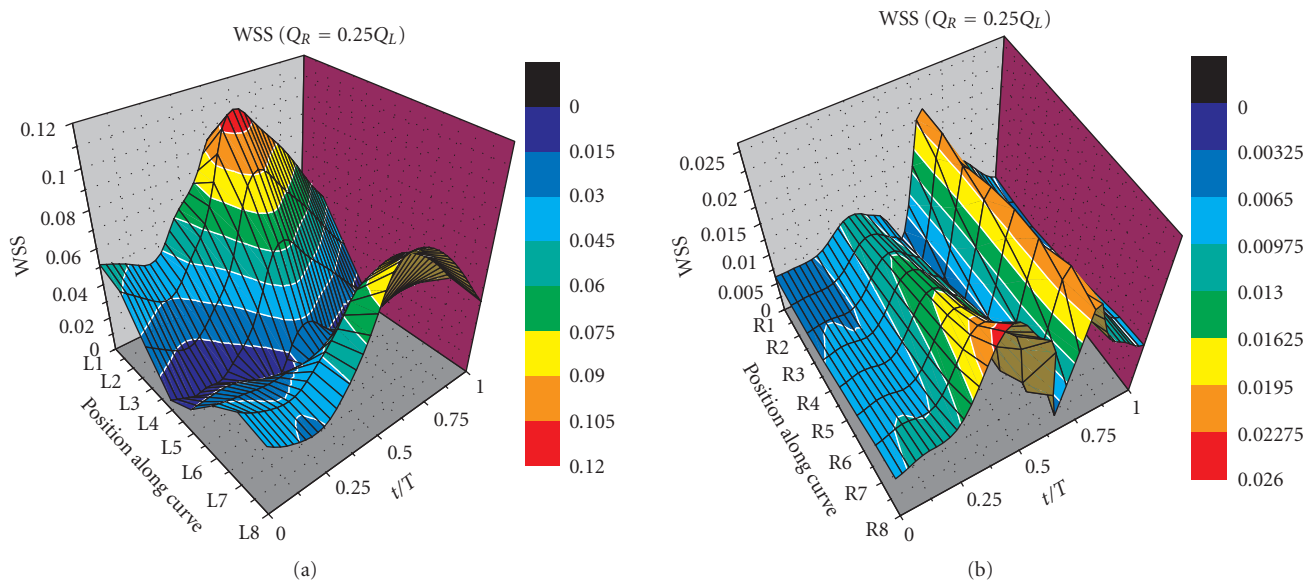


FIGURE 11: WSS versus position and time for $Q_R = 0.25Q_L$ on (a) the left and (b) the right bifurcation regions.

from the dominant A1 shifts toward the contralateral ACA with unequal A1 flow rates, the flow impinges at a smaller impingement zone with a more acute angle with respect to the normal of the impingement surface. In addition, the impingement region tends to oscillate along the A2-ACOM adjoining wall with shifting toward the contralateral ACA during systole and vice versa during diastole. By contrast, the case with equal flow rates demonstrates (see Figure 3) that the incoming streams hit at a more oblique angle with respect to the impingement region and oscillate less. Cebra et al. have found that aneurysms that had smaller and changing impingement regions and disturbed flow patterns were associated with rupture. These related findings

further strengthen the association of unstable progression of aneurysm growth with large temporal gradient WSS.

Figures 4–6 demonstrate large spatial WSS gradients at the left impingement site where the higher flow parent stream impinges and bifurcates. Spatial gradients from disturbed laminar shear stress from regional flow disturbances have been found to be important local modulators of endothelial cell expression of various growth factors [16]. The plots of the right bifurcation region as seen in Figures 4–6, and 12 demonstrate that the unsteady effects of flow separation region in unequal flow rates are subject to a double peak in the temporal evolution of WSS. While the magnitude of WSS is decidedly less in the unequal A1 flow

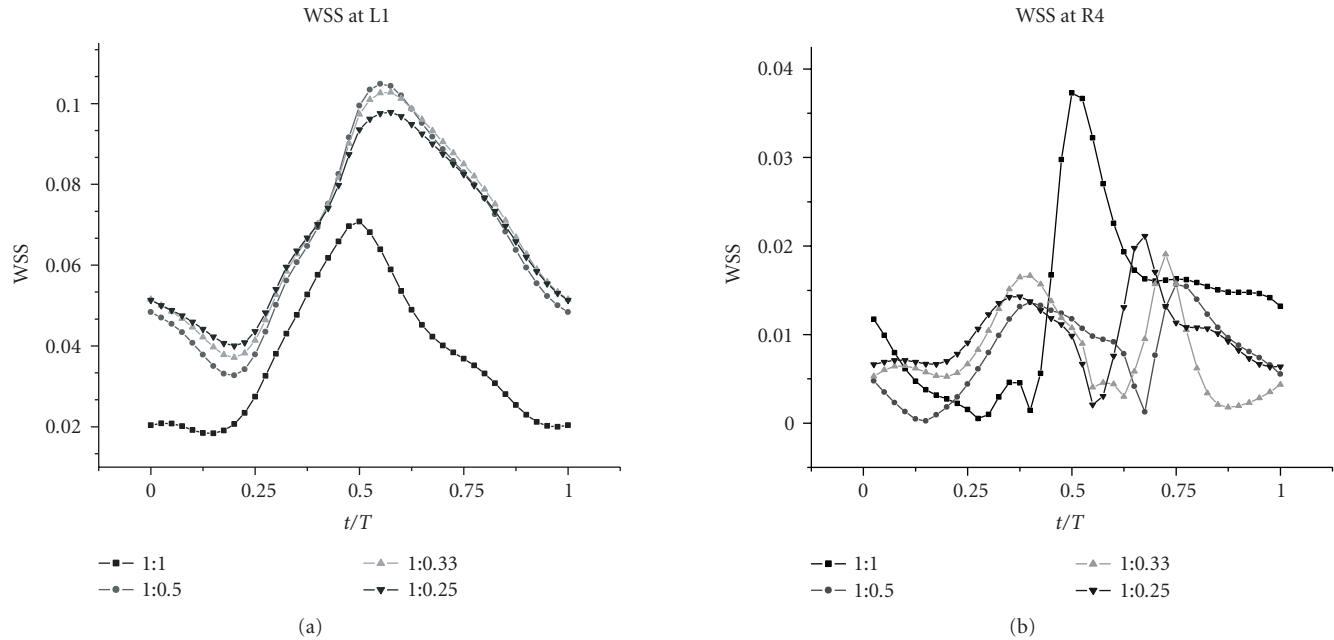


FIGURE 12: WSS on (a) the left and (b) the right impingement points.

rate condition as compared to equal flow rate conditions, it has been shown that low-amplitude oscillating shear stresses in unsteady flows are an important determining factor in endothelial cell turnover and may be more important than WSS amplitude [17, 18]. Another interesting observation from Figure 12 is that the frequency between the two peaks increases as the imbalance between the incoming A1 inflows is greater. The increased frequency is about 4% of the total pulsation cycle between the 2:1 and 3:1 case and increases to 8% between the 2:1 and 4:1 studies. These differences reflect the time during the pulsation cycle at which flow separation occurs as the cross-flow navigates through the ACOM segment for the various imbalances in A1 flow. Thus, unequal A1-ACA flow rates induce a change in pattern of hemodynamic stresses which may affect endothelial cells by mechanotransduction in addition to mechanical deformation stresses.

In some cases, flow separation has been shown to be sufficient to cause activation of platelets and to cause freely floating aggregates [19–21]. This suggests that certain regions of unsteady flow may possibly contribute to thromboembolic phenomena. Thus, the ACA-ACOM junction may serve as key centers of platelet aggregates which may release constituents and become a source of emboli. Spontaneous thrombosis and extension of thrombi to bilateral ACAs from an unruptured ACOM aneurysm have been reported in literature and demonstrate that hemodynamic phenomenon in susceptible geometry can lead to cerebrovascular accidents [22].

It is interesting to note that the alteration in hemodynamic stress changes occurs despite the overall reduced flow rate through the anterior cerebral circulation. Unequal flow through the ACAs is a situation which may occur from a number of pathological clinical situations as well

as iatrogenic interventions. Intracranial hemorrhage after carotid stenting is a known fatal complication in the postprocedure period [23]. Indeed, the hemodynamic implications of endovascular interventions such as stenotic vessel angioplasty and stenting deserve further investigation. The findings presented may provide some insight into the etiology of wall vessel weakening and perhaps assist in clinical management of patients with ACA-ACOM aneurysms.

The current study is concentrated on the effect of unequal parent ACA flow rates on the hemodynamics of ACOM. By employing a 2D symmetric model, other geometrical factors could be controlled and quick simulation results could be obtained. Even though 2D simulations could be anticipated to reasonably resemble the main characteristics of 3D flows, significant differences between the 2D and 3D simulations are also anticipated to appear in cases of complex geometrical models. The model used in this study employed a high degree of symmetry in an attempt to minimize such 3D confounding factors. More realistic patient-specific 3D models are the subject of future studies.

5. Conclusions

Unequal pulsatile flow rates through the A1-ACA arteries result in bifurcation and unstable cross-flow through the ACOM from the higher flow parent artery. There is an increase in WSS magnitude at the impingement site on the same side as the parent A1 segment and a change in position of the maximum WSS related to the left to right flow ratios. The increased hemodynamic stress appears to occur where aneurysms are expected to develop. At the contralateral A2-ACOM adjoining wall, a double peak in the WSS amplitude occurs from local unsteady effects

arising from flow separation as cross-flow negotiates the ACOM segment. These increased hemodynamic stresses at the bifurcation regions may be a contributing factor to vessel wall weakening where aneurysms often occur.

References

- [1] R. M. K. W. Lee, "Morphology of cerebral arteries," *Pharmacology & Therapeutics*, vol. 66, no. 1, pp. 149–173, 1995.
- [2] P. F. Davies, C. F. Dewey Jr., S. R. Bussolari, E. J. Gordon, and M. A. Gimbrone Jr., "Influence of hemodynamic forces on vascular endothelial function. In vitro studies of shear stress and pinocytosis in bovine aortic cells," *The Journal of Clinical Investigation*, vol. 73, no. 4, pp. 1121–1129, 1984.
- [3] M. D. Ford, G. R. Stuhne, H. N. Nikolov, et al., "Virtual angiography for visualization and validation of computational models of aneurysm hemodynamics," *IEEE Transactions on Medical Imaging*, vol. 24, no. 12, pp. 1586–1592, 2005.
- [4] X. He, P. Venugopal, J. R. Cebral, H. Schmitt, and D. J. Valentino, "Reproducibility of brain hemodynamic simulations: an inter-solver comparison," in *Medical Imaging 2006: Physiology, Function, and Structure from Medical Images*, vol. 6143 of *Proceedings of SPIE*, pp. 1–12, San Diego, Calif, USA, February 2006.
- [5] J. R. Cebral, M. A. Castro, J. E. Burgess, R. S. Pergolizzi, M. J. Sheridan, and C. M. Putman, "Characterization of cerebral aneurysms for assessing risk of rupture by using patient-specific computational hemodynamics models," *American Journal of Neuroradiology*, vol. 26, no. 10, pp. 2550–2559, 2005.
- [6] D. N. Ku, "Blood flow in arteries," *Annual Review of Fluid Mechanics*, vol. 29, pp. 399–434, 1997.
- [7] D. N. Ku, D. P. Giddens, C. K. Zarins, and S. Glagov, "Pulsatile flow and atherosclerosis in the human carotid bifurcation. Positive correlation between plaque location and low and oscillating shear stress," *Arteriosclerosis*, vol. 5, no. 3, pp. 293–302, 1985.
- [8] S. A. Berger and L.-D. Jou, "Flows in stenotic vessels," *Annual Review of Fluid Mechanics*, vol. 32, pp. 347–382, 2000.
- [9] C. A. Taylor, T. J. R. Hughes, and C. K. Zarins, "Finite element modeling of blood flow in arteries," *Computer Methods in Applied Mechanics and Engineering*, vol. 158, no. 1-2, pp. 155–196, 1998.
- [10] R. Kwak, T. Ohi, H. Niizuma, and J. Suzuki, "Afferent artery and the site of neck of anterior communicating aneurysms," *Surgical Neurology*, vol. 13, no. 3, pp. 221–223, 1980.
- [11] <http://www.solidworks.com>.
- [12] F. Cassot, V. Vergeur, P. Bossuet, B. Hillen, M. Zagzoule, and J.-P. Marc-Vergnes, "Effects of anterior communicating artery diameter on cerebral hemodynamics in internal carotid artery disease: a model study," *Circulation*, vol. 92, no. 10, pp. 3122–3131, 1995.
- [13] M. A. Stefani, F. L. Schneider, A. C. H. Marrone, A. G. Severino, A. P. Jackowski, and M. C. Wallace, "Anatomic variations of anterior cerebral artery cortical branches," *Clinical Anatomy*, vol. 13, no. 4, pp. 231–236, 2000.
- [14] G. Batchelor, *An Introduction to Fluid Dynamics*, Cambridge University Press, Cambridge, UK, 2000.
- [15] <http://www.openfd.co.uk/openfoam>.
- [16] T. Nagel, N. Resnick, C. F. Dewey Jr., and M. A. Gimbrone Jr., "Vascular endothelial cells respond to spatial gradients in fluid shear stress by enhanced activation of transcription factors," *Arteriosclerosis, Thrombosis, and Vascular Biology*, vol. 19, no. 8, pp. 1825–1834, 1999.
- [17] P. F. Davies, A. Remuzzi, E. J. Gordon, C. F. Dewey Jr., and M. A. Gimbrone Jr., "Turbulent fluid shear stress induces vascular endothelial cell turnover in vitro," *Proceedings of the National Academy of Sciences of the United States of America*, vol. 83, no. 7, pp. 2114–2117, 1986.
- [18] E. Sho, H. Nanjo, M. Sho, et al., "Arterial enlargement, tortuosity, and intimal thickening in response to sequential exposure to high and low wall shear stress," *Journal of Vascular Surgery*, vol. 39, no. 3, pp. 601–612, 2004.
- [19] W. A. Morton, E. M. Parmentier, and H. E. Petschek, "Study of aggregate formation in region of separated blood flow," *Thrombosis et Diathesis Haemorrhagica*, vol. 34, no. 3, pp. 840–854, 1975.
- [20] S. Einav and D. Bluestein, "Dynamics of blood flow and platelet transport in pathological vessels," *Annals of the New York Academy of Sciences*, vol. 1015, pp. 351–366, 2004.
- [21] O. A. el-Masry, I. A. Feuerstein, and G. F. Round, "Experimental evaluation of streamline patterns and separated flows in a series of branching vessels with implications for atherosclerosis and thrombosis," *Circulation Research*, vol. 43, no. 4, pp. 608–618, 1978.
- [22] R. D. Brownlee, B. I. Tranmer, R. J. Sevvick, G. Karmy, and B. J. Curry, "Spontaneous thrombosis of an unruptured anterior communicating artery aneurysm: an unusual cause of ischemic stroke," *Stroke*, vol. 26, no. 10, pp. 1945–1949, 1995.
- [23] W. F. Morrish, S. Grahovac, A. Douen, et al., "Intracranial hemorrhage after stenting and angioplasty of extracranial carotid stenosis," *American Journal of Neuroradiology*, vol. 21, no. 10, pp. 1911–1916, 2000.

Research Article

An Autonomic Nervous System Model Applied to the Analysis of Orthostatic Tests

Virginie Le Rolle,^{1,2} Alfredo I. Hernández,^{1,2} Pierre-Yves Richard,³ and Guy Carrault^{1,2}

¹INSERM U642, 35000 Rennes, France

²LTSI, Université de Rennes 1, 35000 Rennes, France

³Supelec-IETR, Campus de Rennes, Avenue de la Boulaie, 35511 Cesson Sévigné, France

Correspondence should be addressed to Virginie Le Rolle, virginie.lerolle@univ-rennes1.fr

Received 30 August 2007; Accepted 10 March 2008

Recommended by Ewa Pietka

One of the clinical examinations performed to evaluate the autonomic nervous system (ANS) activity is the tilt test, which consists in studying the cardiovascular response to the change of a patient's position from a supine to a head-up position. The analysis of heart rate variability signals during tilt tests has been shown to be useful for risk stratification and diagnosis on different pathologies. However, the interpretation of such signals is a difficult task. The application of physiological models to assist the interpretation of these data has already been proposed in the literature, but this requires, as a previous step, the identification of patient-specific model parameters. In this paper, a model-based approach is proposed to reproduce individual heart rate signals acquired during tilt tests. A new physiological model adapted to this problem and coupling the ANS, the cardiovascular system (CVS), and global ventricular mechanics is presented. Evolutionary algorithms are used for the identification of patient-specific parameters in order to reproduce heart rate signals obtained during tilt tests performed on eight healthy subjects and eight diabetic patients. The proposed approach is able to reproduce the main components of the observed heart rate signals and represents a first step toward a model-based interpretation of these signals.

Copyright © 2008 Virginie Le Rolle et al. This is an open access article distributed under the Creative Commons Attribution License, which permits unrestricted use, distribution, and reproduction in any medium, provided the original work is properly cited.

1. Introduction

Heart rate variability (HRV) represents one of the most efficient indicators to characterize the modulation of the cardiovascular system (SCV) by the autonomic nervous system (ANS) [1]. In fact, HRV can be easily extracted from the electrocardiogram (ECG), which is a common noninvasive clinical examination reflecting the electrical activity of the heart. However, the interpretation of HRV measurements can be difficult because of the complex mechanisms involved in the autonomic regulation. Time domain and frequency domain methods have been developed to assist the signal analysis and to estimate the levels of vagal (parasympathetic) and sympathetic activities [1]. Although these classical indicators provide useful information and have been widely used in clinical practice, a model-based approach can be particularly useful to complement this information and to ease its interpretation, as these mathematical models directly

represent the interactions between the ANS and the CVS [2]. Such a model could also assist in the prediction of the patient's response to different physiological conditions or therapeutic strategies. However, a necessary step for such model-based interpretation methods is the creation of a patient-specific instance of the model, characterized by individualized parameters.

In this paper, we propose a model-based approach to reproduce patient-specific HRV measurements acquired during tilt tests. After a brief description of the underlying physiology of ANS regulation, a new model of the short-term autonomic regulation of the cardiovascular system is presented in Section 2. The model is constituted of the following subsystems: (i) the cardiac mechanical activity, (ii) the circulatory system and (iii) the autonomic baroreflex loop, including afferent and efferent pathways. The conditions for the simulation of a tilt test using this model and the proposed identification procedure are also described in Section 2.

Section 3 presents results of the identification procedure applied to the analysis of tilt tests of healthy and pathologic subjects. Finally, Section 4 presents the conclusions of this work.

2. Methods

2.1. Brief Description of the Underlying Physiology

The cardiovascular system is composed of the heart and two closed systems of vessels known as systemic and pulmonary systems. The primary objective of the CVS is to transport the blood to bring the oxygen from the lung to the organs that need it, and to carry important substances such as hormones and nutrients. The heart is a muscular pump system that pushes blood to all parts of the body. It is divided into four chambers: the two top chambers are called atria, and the lower chambers are called ventricles. The atria collect the blood that enters the heart and push it to the ventricles which eject blood out of the heart into the arteries. These heart chambers alternate periods of relaxation, called diastole, and periods of contraction, called systole.

At the scale of cardiac cells, the contraction is due to the shortening and lengthening of sarcomeres which are the elementary mechanical contractile elements. This mechanical activity is under the influence of an electrical activity, since the variation of the calcium concentration during the action potential (electrical activation of excitable cells) allows the development of force. This variation of force in the cardiac muscle fibres allows the delivering of a sufficient ventricular pressure.

The ANS is responsible for the short-term regulation of the SCV. The baroreflex is initiated by the stimulation of the baroreceptors which are sensory receptors that respond to variations of pressure that are mainly located in the wall of atria, vena cava, aortic arch, and carotid sinus. Other pressure receptors, called cardiopulmonary receptors, are found in veins and atria. Changes in blood pressure are translated into corresponding effects on the efferent sympathetic and parasympathetic pathways. The sympathetic system has a global excitatory effect, increasing heart rate, ventricular contractility, peripheral vascular resistance, and so forth, during situations like hunger, fear, and physical activity. The parasympathetic system presents generally an opposite effect. The main effectors are the heart rate, myocardium contractility, peripheral resistance, and venous blood volume.

The head-up tilt test allows the analysis of a patient's variations on heart rate and blood pressure during a controlled postural change from a supine to a head-up position. During tilt, approximately 300 to 800 mL of blood may be shifted into the lower extremities, leading to a reduction of venous return and hence of stroke volume. In normal subjects, a decrease in the mean arterial blood pressure (MABP) causes the unloading of arterial baroreceptors, providing a sympathetic activation and a vagal inhibition that leads to an increase on heart rate, ventricular contractility, and

peripheral vasoconstriction. A balance is established between heart rate and contractility to maintain the cardiac output and MABP in physiological levels. Some works have shown that slight differences in this response can be observed in patients suffering from diabetes mellitus [1].

2.2. Model Description

The proposed model of the SCV represents the main components of the baroreflex described in the previous section, namely, (i) the ventricles, (ii) the circulatory system, and (iii) the short-term regulation by the ANS. The ventricular model includes a simplified representation of the electromechanical processes involved in the ventricular activity. Moreover, the short-term autonomic regulation of the CVS is taken into account by the modulation of cardiovascular variables (heart rate, etc.). The bond graph formalism can be particularly useful for modelling physiological systems that often include various energy domains, for example, for the design of a bond-graph-based controller for muscle relaxant anesthesia [3] or for modelling the musculoskeletal structure [4]. Models of the vascular system [5–7] are especially interesting, since they take into account different energy phenomena (hydraulic, mechanic, chemical, etc.). The appendix presents the basics of bond graph modelling. A description of each one of the proposed model components is presented in the following sections.

2.2.1. Ventricles

A variety of mathematical models of the ventricular function has been proposed in the literature in order to represent explicitly, at different levels of detail, the cardiac electrical activity [8–10], the excitation-contraction coupling [11–13], the mechanical activity [14, 15], and the mechano-hydraulic coupling [16, 17]. Complete models of ventricular activity are developed from a combination of these different energy domain descriptions [18, 19]. The most detailed approaches represent a fine-grained description of the ventricular activity (at the cellular or subcellular levels), which is necessary for the analysis of regional myocardial dynamics [17, 20, 21]. However, these approaches require significant computational resources and are characterized by an important number of parameters. These aspects reduce the model identifiability, make more difficulty to couple these models with models of other physiological systems (e.g., the ANS) and thus limit their application to our problem. On the other hand, the simplest ventricular models are based on a time-varying elastance [22, 23], which can give realistic simulations of ventricular pressure and volume and require low computational resources. However, the influence of heart rate, calcium concentration variations, and autonomic modulation during the contraction process are not taken into account in these models.

The proposed model can be seen as an improvement of global elastance models and includes a simplified description of the excitation-contraction process. The well-known Beeler and Reuter [24] model of the cardiac action potential (BR model) has been chosen, as it presents a basic description of

the intracellular calcium $[Ca^{2+}]_i$ dynamics, while keeping a low level of complexity.

The ventricular mechanical activity is usually described as a function of its active and passive properties. Active properties are under the influence of an electrical activity, since the variation of the calcium concentration during the action potential allows the development of force. Passive properties are mainly due to myocardium organization (fibre orientation, collagen density, etc.). Myocardial tension is usually expressed as the sum of active and passive tensions.

The calcium concentration variable of the BR model is used as input to a model of active mechanical activity. In the present work, the active tension is inspired from the works of Hunter et al. [12] and is defined as

$$T_a = T_{ref} \frac{[Ca^{2+}]_i^n}{[Ca^{2+}]_i^n + Ca_{50}^n} [1 + \beta(\lambda - 1)], \quad (1)$$

where T_{ref} is the value of the tension at $\lambda = 1$, Ca_{50} the calcium concentration at 50% of the isometric tension, n is the Hill coefficient determining the shape of the curve and β is the myofilament ‘‘cooperativity.’’ Assuming that the ventricle is supposed to be made of circumferential muscular fibres, the fibre strain λ can be expressed as a function of ventricular radius;

$$\lambda = \frac{r}{R}, \quad (2)$$

where r and R are the ventricular radii in the deformed and undeformed states, respectively. In order to obtain the total active force developed by the ventricle, the resulting tension is multiplied by the myocardial wall surface S :

$$F_a = S \cdot T_a. \quad (3)$$

Passive tensions T_p are derived from the pole-zero constitutive law presented in [25] to have a relation between the circumferential strain and the tension in the fibre axis.

(i) For axial tension ($\lambda > 1$):

$$T_p = \frac{k_1 \varepsilon_{11}}{(a_1 - \varepsilon_{11})^{b_1}} \left[2 + \frac{b_1 \varepsilon_{11}}{a_1 - \varepsilon_{11}} \right], \quad \text{where } \varepsilon_{11} = \frac{1}{2} (\lambda^2 - 1). \quad (4)$$

(ii) For axial compression ($\lambda < 1$):

$$T_p = -\frac{2 \cdot k_2 \varepsilon_{22}}{(a_2 - \varepsilon_{22})^{b_2}} \left[2 + \frac{b_2 \varepsilon_{22}}{a_2 - \varepsilon_{22}} \right], \quad \text{where } \varepsilon_{22} = \frac{1}{2} \left(\frac{1}{\lambda} - 1 \right). \quad (5)$$

The total passive force developed by the ventricle is then calculated by multiplying the passive tension and wall surface S :

$$F_p = S \cdot T_p. \quad (6)$$

The total force developed by the ventricle is the sum of active and passive ones:

$$F = F_a + F_p. \quad (7)$$

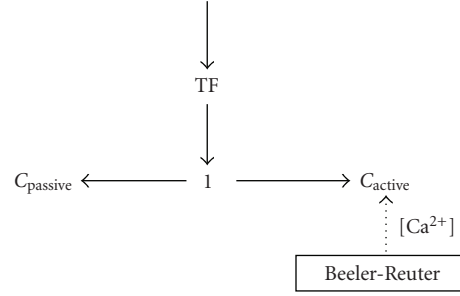


FIGURE 1: Bond graph model of the left ventricle. The calcium concentration variable of the BR model is used as input to a model of the active mechanical activity, which is described by active and passive capacitive elements implementing (3) and (6), respectively. A 1-junction (7) relates active and passive capacitances. This junction is linked to a transformer that describes the change of energy domain from mechanics to hydraulics, as presented in (8).

So the force in the fibre axis has been defined as a sum of two functions of ventricular radii. In the Bond Graph formalism, the force developed by the ventricle, which is defined by the previous relations, can be described by two capacitive elements representing the active and passive properties. A 1-junction is used to connect the two capacitive elements because the total force in the fibre axis is defined as the sum of two forces (Figure 1).

During the ventricular contraction, the rise of the force and the variation of the fibre length lead to variations of ventricular pressure. Assuming that the ventricle is supposed to be made of circumferential muscular fibres, the relation between fibre force and ventricular pressure proposed in [6] can be used. In this approach, the ejected volume V is defined as a function of the ventricular radius by

$$V = Ar^n, \quad (8)$$

where the values of A and n are empirically defined. This approach has shown to provide simulation results that are coherent with physiology [6]. As a result, the change of energy domain from mechanics to hydraulics can be described by a transformer implementing (4).

2.2.2. Circulation

The systemic and pulmonary circulations are composed of different kinds of vessels called arteries, capillaries, and veins. Windkessel models are often used to represent the vascular system [26, 27] by using an electrical analogy. In fact, each part of a vessel can be represented by a set of equations relating its volume V , flow Q , and pressure P .

- (i) Capacity (C): as blood vessels are characterized by their elastic properties, a relation between the volume and the variation of pressure can be defined: $V = V_0 + CP$, where V_0 is the unstretched volume.
- (ii) Resistance (R): the resistive properties of vessel are characterized by a relation between the flow and the variation of pressure: $Q = \Delta P/R$.

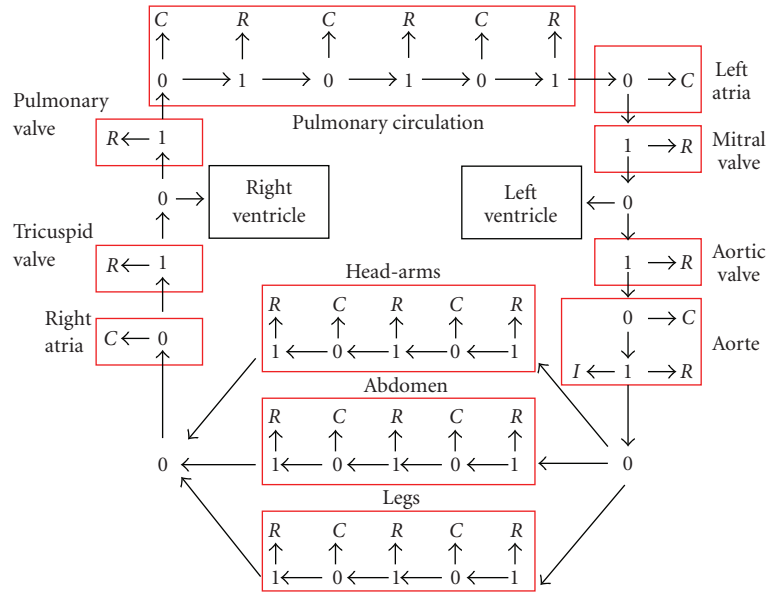


FIGURE 2: Proposed Bond Graph model of the circulation. Groups of vessels are represented by several Bond Graph elements (capacitance, a resistance, and an inertance) to represent the pulmonary and the systemic circulation. The latter has been divided into three different parts (the head, the abdomen, and the legs).

- (iii) Inertance (I): the mass of blood brings some inertial effects through the relation $P = I \cdot dQ/dt$.

Model of vessels can be directly represented in a Bond Graph model by a parallel capacitance, a resistance, and an inertance in series. Models of the whole circulation are defined in a global way by considering groups of vessels (e.g., pulmonary and systemic circulation) in an equivalent lumped model (Figure 2). In order to simulate the effect of a postural change from a supine to a head-up position, the influence of gravity on different parts of the body should be taken into account. The model of the systemic circulation has thus been divided in three parts (the head, the abdomen, and the legs). The heart valves are modelled as nonideal diodes using modulated resistances. The atria are modelled as constant capacitances. The ventricular model described in the previous section is used for the left and right ventricles. Tables 1, 2, 3 and 4 summarizes the values used for the parameters of the circulation model.

2.2.3. Autonomic Nervous System

The existing models of ANS, which are based on a closed-loop representation, can be classified into three main categories.

- (i) *Behavioral models* are based on signal processing and identification theories, such as autoregressive, moving-average models with exogenous input (ARMAX) [35]. Although they allow the reproduction of experimental signals, the physiological interpretation of the parameters of these models is difficult as there is not a direct structural relationship

between the physiology and the model components and parameters.

- (ii) *Global models* present unphysiological descriptions of the system dynamics [36].
- (iii) *Representation models* consist in modelling the different subsystems that can be associated with an entity of the cardiovascular control [37, 38]. Many of them [33, 34] are based on the structure proposed originally by Wesseling and Settels [39], which is composed of delays and first-order filters. This kind of formalism allows the representation of the global neurotransmitter dynamics for a particular efferent pathway and the description of the different response times of the sympathetic and the parasympathetic branches.

A new ANS model is presented to describe the activity of the baroreflex and the cardiopulmonary reflex (Figure 3). The baroreceptor input is the arterial pressure (P_a) and its dynamical properties are represented by a first-order filter (Figure 4(a)). The cardiopulmonary receptors are represented by the difference between instantaneous and mean venous pressures (P_v and P_{vmean} , respectively) (Figure 4(b)).

Four variables are controlled in the model by means of different efferent pathways: heart rate, cardiac contractility, systemic resistance, and venous volume. Heart rate depends on the action of both the sympathetic and the parasympathetic systems. The cardiac contractility, the systemic resistance, and the venous volume are only on the influence of the sympathetic system. The same structure, based on a normalized function, a delay and a first-order filter, is used for each one of the modelled efferent pathways. The normalized

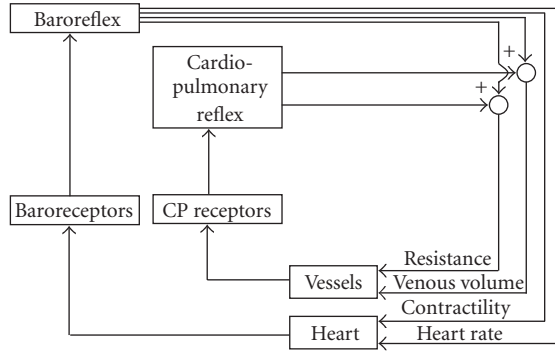


FIGURE 3: Diagram showing the coupling between the model of the ANS and the models of the ventricles and the circulatory system.

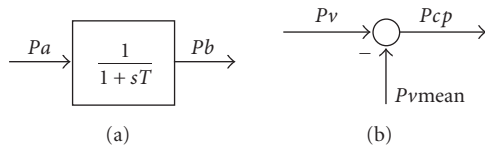


FIGURE 4: Model of the baroreceptors (a) and the cardiopulmonary receptors (b).

function is the sigmoid input-output relationship defined in [34]:

$$Fx(t) = a_x + \frac{b_x}{e^{Tx(PB(t)-Nx,o)} + 1}. \quad (9)$$

The generic parameter x represents heart rate, contractility, peripheral, and venous volume regulation. The ANS model is coupled to the CVS by injecting in the latter the four previous controlled variables in the following way.

- (i) *Heart rate*: the model of heart rate regulation is composed of two parts for the vagal and the sympathetic pathways (Figure 5(a)). Each branch is composed of a delay (R_s and R_v are the sympathetic and parasympathetic delays, respectively), and a first-order filter characterized by a gain (K_s and K_v for the sympathetic and the vagal gains, respectively) and a time constant (T_s and T_v). The output signal of the heart rate regulation model (F_c) is continuous and is obtained by adding the contributions from the sympathetic and parasympathetic branches and a basal (unmodulated) heart rate (I_o). To obtain pulsating blood pressure, an integral pulse frequency modulation (IPFM) model is used as it transforms a continuous input signal into an event series [40] (Figure 5(b)). The input of the IPFM model is the output signal of the heart rate regulation model. The output of the IPFM allows the excitation of the model of the electrical activity [24] and each emitted pulse (F_c) brings an augmentation of calcium concentration.
- (ii) *Contractility*: the T_{ref} parameter of the active tension of cardiac fibres can be considered to be an indicator

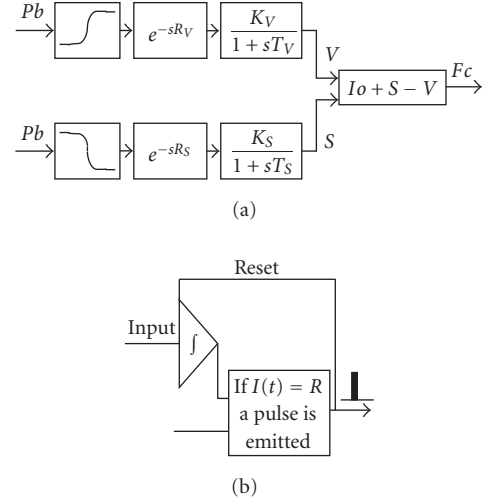


FIGURE 5: Model of heart rate regulation (a) and IPFM model (b).

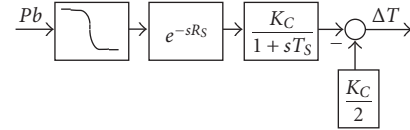


FIGURE 6: Model of contractility regulation.

of the cardiac contractility. In this sense, the T_{ref} definition is replaced by the sum of the basal value and the output signal of the contractility regulation model: $T_{ref} = T_{ref0} + \Delta T$ (Figure 6).

- (iii) *Peripheral resistance*: the systemic resistances are equal to the sum of a constant value and a component, which depends on the ANS regulation: $R = R_0 + \Delta R$ (Figure 7). P_b and P_{cp} are, respectively, the baroreceptors and the cardiopulmonary receptors outputs.
- (iv) *Venous volume*: the constitutive relation of the venous capacity depends on the unstretched volume V_0 : $\Delta P = (V - V_0)/C$. The regulated part of the unstretched volume corresponds to the differences with the basal value: $V_0 = V_{0basal} - \Delta V$ (Figure 8). P_b and P_{cp} are, respectively, the baroreceptors and the cardiopulmonary receptors outputs.

2.3. Simulation of a Tilt Test with the Proposed Model

The tilt test produces significant variations of blood pressure in the different parts of the body. In order to take into account the effect of gravity, different pressure levels are imposed on the hydraulic capacities of the model [26]. In the Bond Graph formalism, these pressures are introduced by a 1-junction (Figure 9(b)):

$$P = P_0 + P_{\text{tilt}}, \quad (10)$$

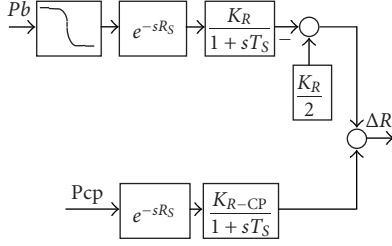


FIGURE 7: Model of peripheral resistance regulation.

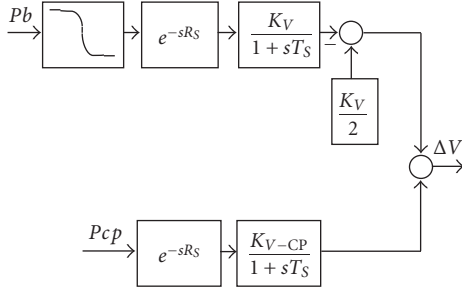


FIGURE 8: Model of venous volume regulation.

where P_0 is the fluid pressure in the supine position and P_{tilt} has been defined in [26] by the relation

$$P_{\text{tilt}} = \begin{cases} P_{\text{gravity}} \cdot \sin(\alpha(t)), & t_0 \leq t \leq t_0 + t_{\text{tilt}}, \\ P_{\text{gravity}} \cdot \sin(\alpha_{\text{max}}), & t > t_0 + t_{\text{tilt}}, \end{cases} \quad (11)$$

where $\alpha(t)$ is the table angle represented as a ramp function from 0 to the maximal angle α_{max} , t_0 is the onset of tilt, t_{tilt} is time to maximum angle and P_{gravity} is the pressure due to gravity, which is equal to

$$P_{\text{gravity}} = \rho \cdot g \cdot h, \quad (12)$$

where ρ is the fluid density and g is the gravitational constant. The parameter h corresponds to the mean distance between one part of body and the heart level. For an adult, the mean value for h is equal to -30 cm for the upper part, 20 cm for the abdomen, and 80 cm for the legs. So it is possible to determine the variation of the pressure due to the gravity in function of the part of the body that is considered $P_{\text{gravity}} = -20$ mmHg for the upper part, $P_{\text{gravity}} = 15$ mmHg for the abdomen, and $P_{\text{gravity}} = 60$ mmHg for the legs.

These results have been confirmed experimentally by measuring the pressure in the finger during three tests realized sequentially on the same normal subject (Figure 9(a)). The arterial pressure has been measured using the Task Force Monitor (CNSystems, Graz, Austria), which is a non-invasive system for continuous beat-to-beat evaluation of cardiovascular variables. Blood pressure is recorded by using the finger plethysmography technique and is regularly calibrated by an oscillometric blood pressure measurement with a cuff-based device.

During the first, second, and third tests, the finger sensor is, respectively, placed at the level of the abdomen, in an up-

TABLE 1: Ventricular model.

	Parameters value	Source
Ventricle		
Transformator		
A	100	[6]
N	3	[6]
Active capacity		
Tref	940 mmHg	[12]
B0	1.45	[12]
B1	1.95	[12]
n.ref	4.25	[12]
pC50.ref	5.33	[12]
B2	0.31	[12]
S	50 cm ²	Estimated
Passive capacity		
k1	1.5 mmHg	[12]
a1	0.22	[12]
b1	1	[12]
k2	0.45 mmHg	[12]
a2	0.41	[12]
b2	2.5	[12]
S	50 cm ²	Estimated

per position and in a lower position. When the finger is located at the level of the abdomen or the upper leg (Figures 9(a)(1), and 9(a)(3)), the blood pressure rises when changing from a supine to a head-up position, because the effect of the gravity brings an augmentation of blood volume in the lower part of the body. Oppositely, the measurement done in an upper position (Figure 9(a)(2)) results in a decreased blood volume at the sensor level during the tilt.

These pressure values are applied by implementing (11) in the circulation model for the three distinct parts defined for the systemic circulation. The introduction of time-varying gravity pressures is at the origin of the nonstationary conditions required to simulate the postural change of the patient.

2.4. Identification Algorithm

Most of the model parameters have been obtained from the literature and are presented in Tables 1, 2, 3, and 4. However, in order to determine patient-specific responses of the HR signal, parameters R_s , R_v , K_s , K_v , T_s , and T_v have been identified, by minimizing an error function between simulated and experimental heart rate signals. As this error function is not differentiable with respect to the model parameters and can have multiple local optima, evolutionary algorithms (EA) have been applied for parameter identification. EA are stochastic search techniques, inspired by the theories of evolution and natural selection, which can be employed to find an optimal configuration for a given system within specific constraints [41]. In these algorithms, each “individual” of a “population” is characterized by a set of parameters (or chromosomes). An initial population

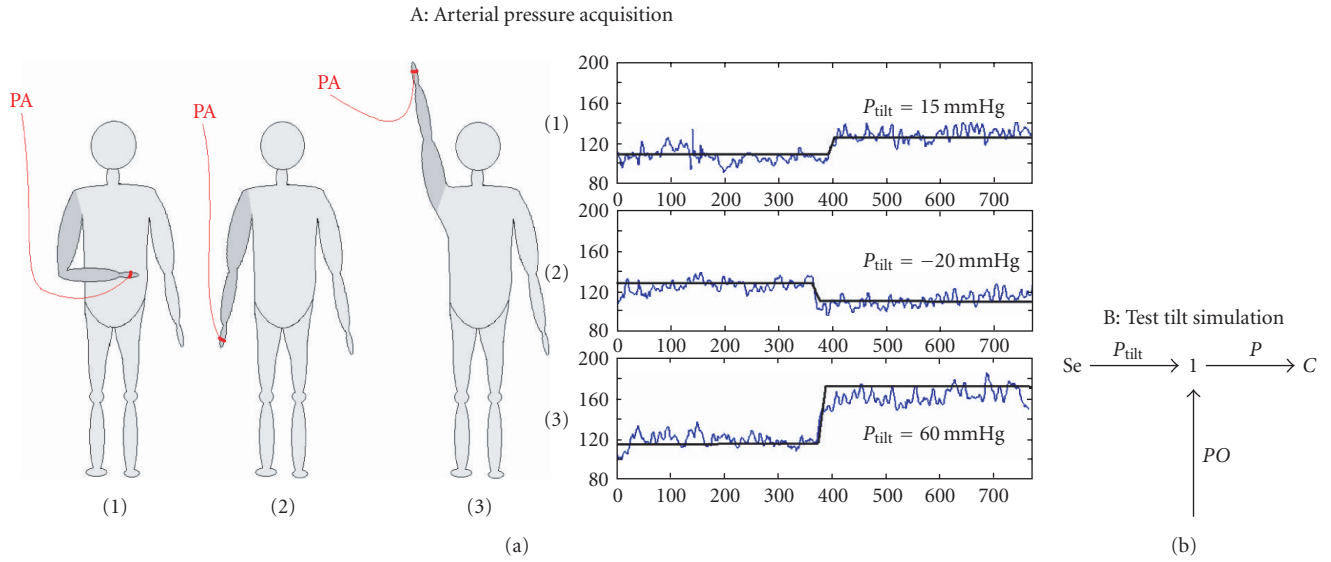


FIGURE 9: (a) Blood pressure acquired at the level of the abdomen (1), the legs (2), and the upper body(3). (b) Effort sources introduced in our model to take into account the gravity effects induced by the tilt test.

TABLE 2: Systemic circulation.

	Parameter value	Source	Unstretched volume	Source
Aorta				
<i>C</i>	0.219 mL/mmHg	[27]	0 mL	[28]
<i>R</i>	0.067 mmHg·s/mL	[27]		
<i>I</i>	0.00082 mmHg·s ² /mL	[27]		
Arteries				
Head-arms				
<i>C</i>	0.73 mL/mmHg	[29]	240 mL	[29]
Abdomen				
<i>C</i>	0.21 mL/mmHg	[30]	274 mL	[30]
Legs				
<i>C</i>	1.28 mL/mmHg	[29]	151 mL	[29]
Arteriols				
Head-arms				
<i>R</i>	3.6 mmHg·s/mL	[26]		
Abdomen				
<i>R</i>	3.307 mmHg·s/mL	[26]		
Legs				
<i>R</i>	3.9 mmHg·s/mL	[26]		
Veins				
Head-arms				
<i>C</i>	8 mL/mmHg	[26]	650 mL	[26]
<i>R</i>	0.23 mmHg·s/mL	[31]		
Abdomen				
<i>C</i>	43.11 mL/mmHg	[31]	1121 mL	[30]
<i>R</i>	0.038 mmHg·s/mL	[26]		
Legs				
<i>C</i>	19 mL/mmHg	[26]	350 mL	[26]
<i>R</i>	0.3 mmHg·s/mL	[26]		

TABLE 3: Pulmonary circulation.

	Parameter value	Source	Unstretched volume	Source
Pulmonary artery				
<i>C</i>	0.605 mL/mmHg	[32]	0 mL	[28]
<i>R</i>	0.1 mmHg·s/mL	[33]		
<i>I</i>	0.00075 mmHg·s ² /mL	[27]		
Arteries				
<i>C</i>	0.02 mL/mmHg	[32]	90 mL	[26]
Arterioles				
<i>R</i>	0.0338 mmHg·s/mL	[27]		
<i>I</i>	0.0018 mmHg·s ² /mL	[27]		
Veins				
<i>C</i>	39.99 mL/mmHg	[27]	490 mL	[26]
<i>R</i>	0.01875 mmHg·s/mL	[27]		
Left Atria				
<i>C</i>	6.665 mL/mmHg	[27]	25 mL	[28]

is created, usually from a set of random chromosomes, and this population will “evolve,” improving its global performance, by means of an iterative process. During this process, each individual is evaluated by means of an error function, and a new generation is produced by applying mutation and crossover operators on selected individuals that present low error values, with probabilities pm and pc , respectively. Convergence and robustness properties of EA have been largely studied in the literature [42–44]. These properties depend upon (i) adequate individual coding, (ii) proper definition of the error function, and (iii) selection of appropriate genetic operators for crossover and mutation.

2.4.1. Individual Representation and Initial Population

Each individual represents an instance of the whole model and is characterized by the 6 real-valued parameters to identify (R_s , R_v , K_s , K_v , T_s , and T_v). In order to reduce the search space, parameters values were bounded to physiologically plausible intervals that have been defined from physiological knowledge. The identification has been realized on heart rate signals of 200 heartbeats during tilt tests.

2.4.2. Error Evaluation

The selection process consists in associating each individual with a selection probability computed from its error value, which has to be minimized. The error function has been defined as the absolute value of the difference between each sample of experimental and simulated heart rate signals. This criterion has been chosen to obtain simulated strain as close as possible to real signals.

2.4.3. Selection Method

Once the error function has been evaluated for each individual, selection is carried out by means of the “Roulette

Wheel” method, adapted for function minimization, in which the probability of selecting a given individual depends on the value of its error function divided by the sum of all the error values of the population. Only standard genetic operators, defined for real-valued chromosomes, have been used in this work: “uniform crossover” which creates two new individuals (offspring) from two existing individuals (parents) by randomly copying each allele from one parent or the other, depending on a uniform random variable and “Gaussian mutation,” which creates a new individual by randomly changing the value of one allele (selected randomly), based on a Gaussian distribution around the current value.

3. Results and Discussion

Head-up tilt test has been applied to eight healthy subjects and eight type 2 diabetic patients. This pathology is characterized by high levels of sugar in the blood (hyperglycemia) due to metabolic disorders on the body’s response to insulin or to insulin deficiency.

For each tilt test, classical indicators for HRV analysis were estimated and the model parameters were identified for each subject. Figures 10 and 11 show the acquired heart rate for the eight healthy subjects and the eight diabetic patients during the tilt test (in gray) and the output of the model after parameter identification (in black). In most cases, it is possible to observe that the heart rate increases abruptly after tilt, applied at the end of the first minute of recording, and slowly decreases as the blood pressure approaches its physiological values.

Simulation results show that the model is able to reproduce the global individual heart rate response to the tilt test for the 16 subjects. The low frequency variations of heart rate are consistent with experimental signals and the first rebound after the heart rate increase is well reproduced in most of the cases. The lack of high frequency components, which can be seen in the experimental heart rate, can be

TABLE 4: ANS.

	Valeur parameters	Source
Baroreceptors		
T	2 s	[33]
Heart rate		
Vagal activity		
K		Identified
T		Identified
R		Identified
ax	0	[34]
bx	1	[34]
NxO	110	[34]
Tx	-0.04	[34]
Sympathic activity		
K		Identified
T		Identified
R		Identified
ax	0.3	[34]
bx	0.7	[34]
NxO	100	[34]
Tx	0.09	[34]
Contractility		
K	1	<i>Estimé</i>
T	10 s	[33, 34]
R	3 s	[33, 34]
ax	0.3	[34]
bx	0.7	[34]
NxO	110	[34]
Tx	0.04	[34]
Peripheral Resistance		
Baroreflex		
K	1	<i>Estimé</i>
T	6 s	[33, 34]
R	3 s	[33, 34]
ax	0.3	[34]
bx	0.7	[34]
NxO	110	[34]
Tx	0.04	[34]
Cardiopulmonary Reflex		
K	0.06	[26]
T	6 s	[33]
R	3 s	[33]
Venous volume		
Baroreflex		
K	1	<i>Estimé</i>
T	6 s	[33, 34]
R	3 s	[33, 34]
ax	0.3	[34]
bx	0.7	[34]
NxO	110	[34]
Tx	0.04	[34]
Cardiopulmonary Reflex		
K	22	[26]
T	6 s	[33]
R	3 s	[33]

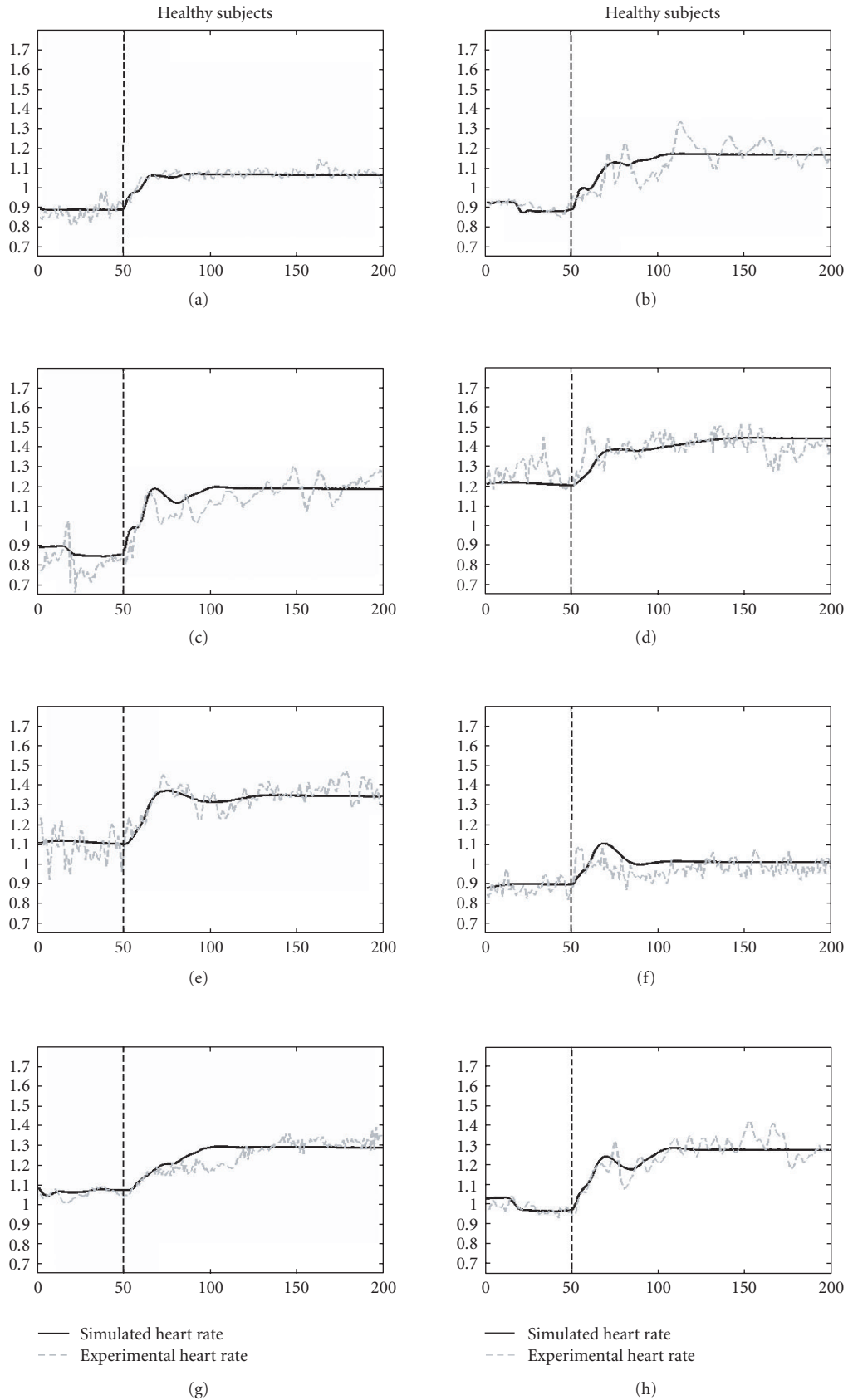


FIGURE 10: Experimental (gray curve) and simulated (black curve) heart rate (beat/second) for healthy subjects.

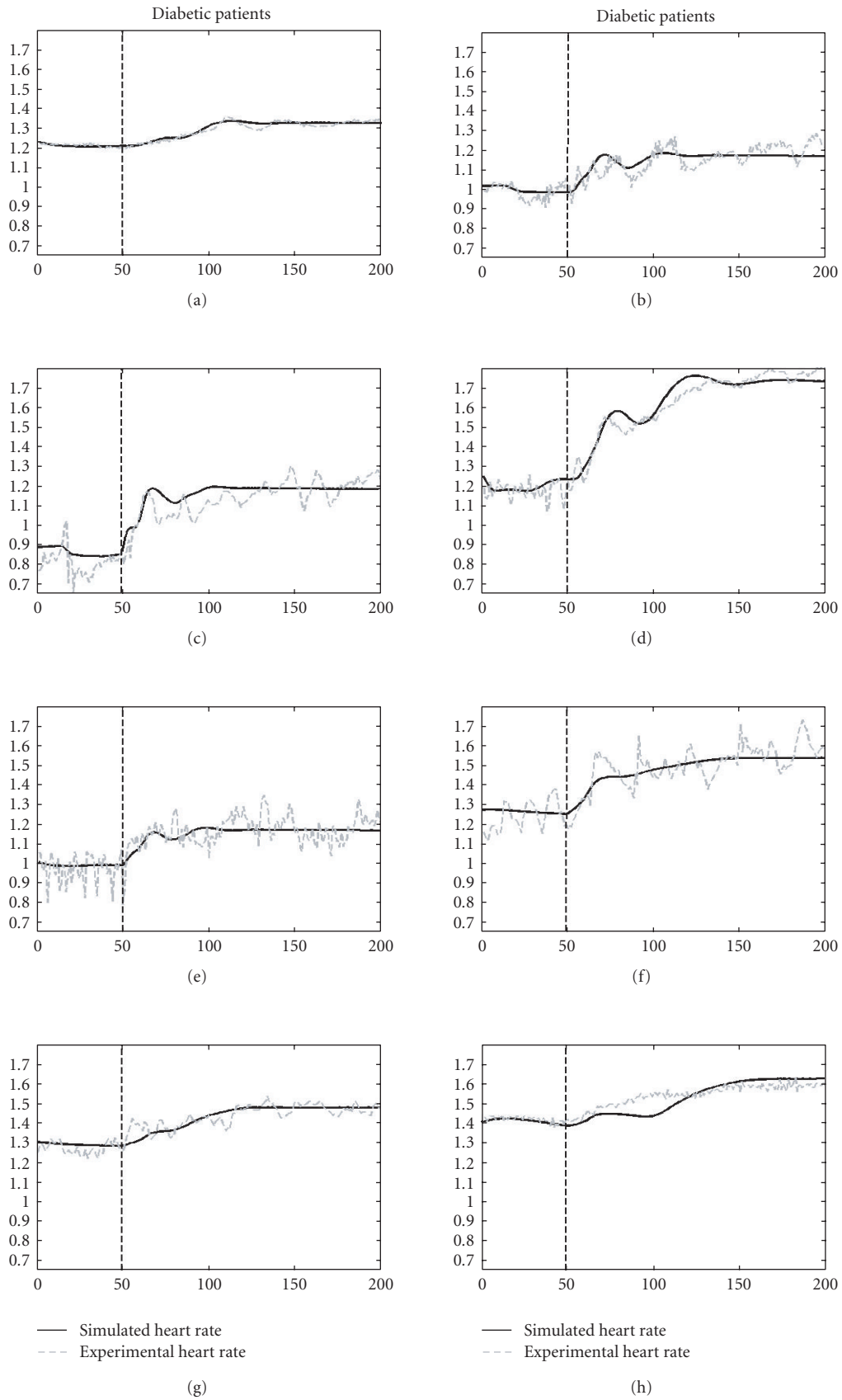


FIGURE 11: Experimental (gray curve) and simulated (black curve) heart rate (beat/second) for diabetic patients.

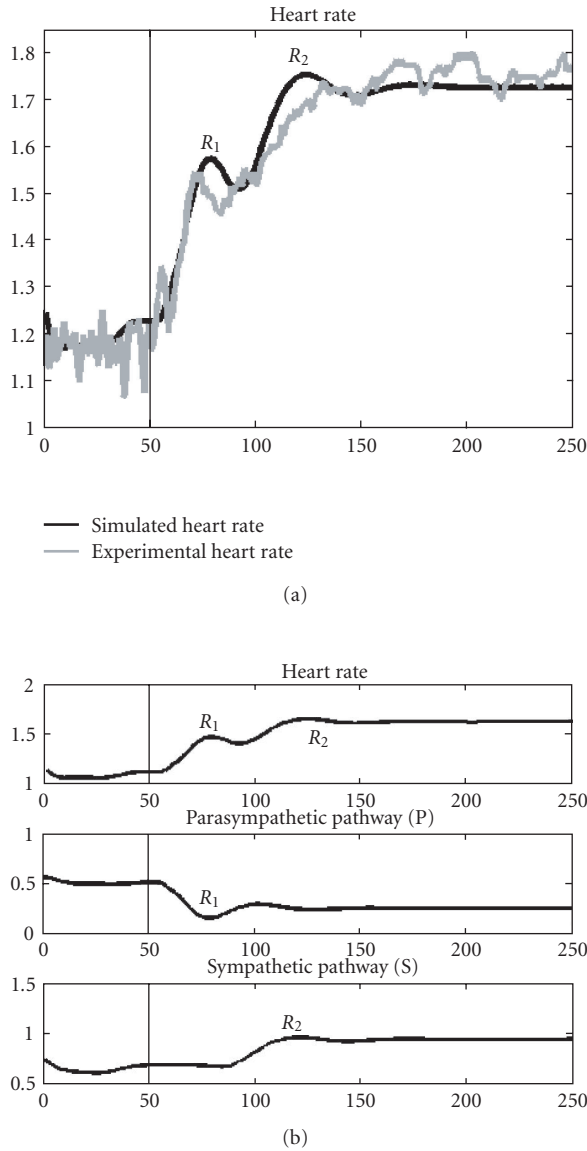


FIGURE 12: Comparison between simulated and experimental heart rates for one diabetic patient (a). Simulation of the activity of sympathetic and parasympathetic pathways after parameter optimization (b).

partly explained by the absence of the influence of respiration and environmental conditions (such as temperature or external modulations through the central nervous system) on the proposed model. Moreover, in this work, the identification algorithm has been applied in batch mode, in order to obtain one set of parameter values characterizing each patient. This is justified as the identified parameters (related to neurotransmitter densities and efferent temporal delays) are not supposed to vary during a tilt test.

Baroreflex control during the tilt test can be analyzed using the cardiovascular model. Figure 12 illustrates how heart rate is affected by the vagal and the sympathetic pathways for one diabetic patient. Two rebounds (R1 and R2) can be observed both on the experimental heart rate and the simulated signals. The first rebound (R1) is explained

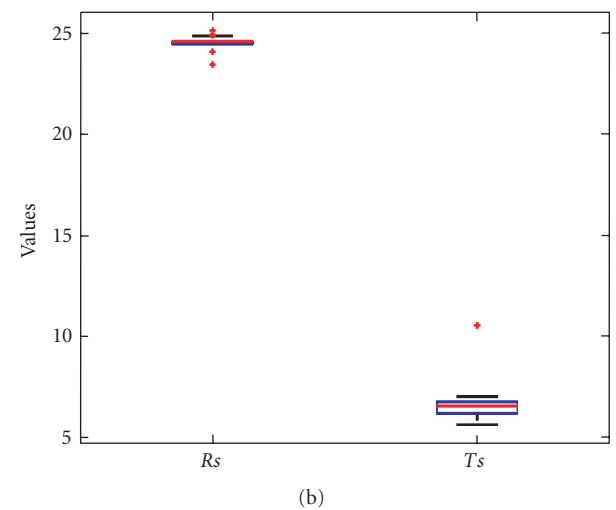
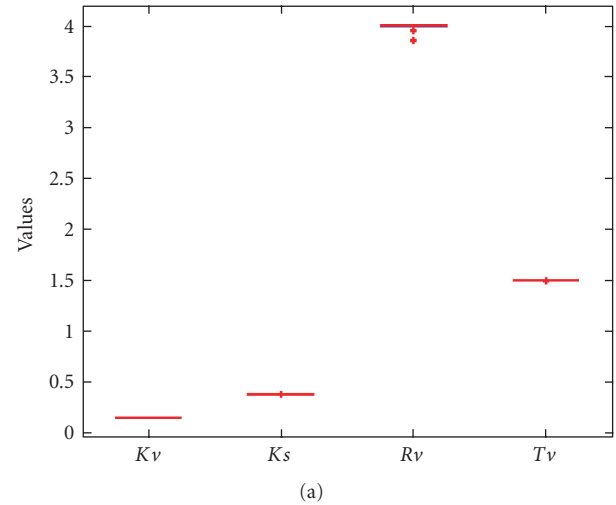


FIGURE 13: Boxplots of parameters K_v , K_s , R_v , and T_v (a), and R_s and T_s (b) obtained after 17 applications of the identification procedure. The vertical axes represent the parameter value.

by the onset of the vagal inhibition just after the beginning of the tilt test. The sympathetic system is slowly activated and can explain the presence of the second rebound (R2). These estimations of the parasympathetic and sympathetic activities can be useful for a better interpretation of HRV signals during tilt tests.

In order to test the robustness of the identification method, the algorithm has been repeated 17 times on one healthy subject. Figure 13 shows boxplots of the values obtained for parameters: K_v , K_s , R_v , R_s , T_v , and T_s for each of the 17 identification processes. These results show the stability of the solution obtained by the identification procedure.

One common time domain indicator for heart rate signal analysis is the standard deviation of the RR intervals between normal beats ($SDNN$). This indicator reflects the global variability of the heart rate and translates the total power of spectral energy of the HRV signal [1]. The $SDNN$

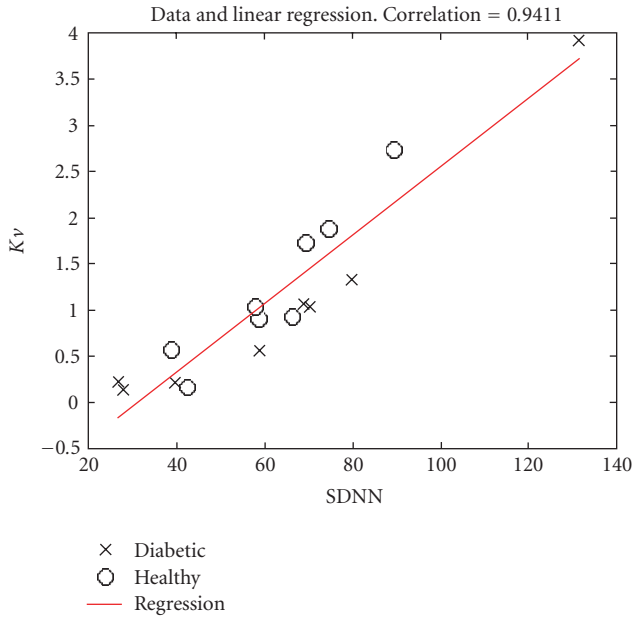


FIGURE 14: Linear regression between Kv and SDNN for the eight healthy subjects and the eight patients.

has been calculated for each subject and compared with the identified model parameters. The correlation coefficient between SDNN and the parasympathetic gain Kv has been calculated and has been found to be equal to 0.9411. Figure 14 shows the linear regression between Kv and SDNN. The correlation between Kv and SDNN can be explained by the presence of the vagal activity both in the low and high frequency components.

4. Conclusion

A new model of the cardiovascular system composed of several coupled subsystems (ventricles, circulation, and ANS) has been proposed and applied to the analysis of heart rate variability signals. The use of Bond Graphs to model ventricular activity and the vascular system has shown to facilitate the coupling of different simple components to form a complex system using the same formalisms for different energetic domains (hydraulic and mechanic). However, although this formalism seems to be particularly adapted to the description of the circulation and global mechanical activity of the ventricles, the marked nonlinearities involved in the genesis of the cardiac action potential has been modeled by a set of ordinary differential equations (the BR model) and coupled with the global Bond Graph model.

The proposed model has been used to reproduce patient-specific heart rate signals during tilt tests on eight healthy subjects and eight diabetic patients. Evolutionary algorithms have been applied as the identification method. After parameter adaptation, simulated signals reproduce the low-frequency components of the observed heart rate signals, which accounts for most of the energy on HRV signals acquired during a tilt test. Moreover, the analysis of identified

model parameters has shown a high correlation between the parameter Kv and the global variability calculated on experimental heart rate. In order to reproduce the high frequency components on the HRV signal, new additions to the model should be made, in particular the coupling of the respiratory system. Recursive identification of some model parameters left fixed in this work can be also applied in order to better represent the nonstationarities generated by the tilt test.

A statistical analysis differentiating the two studied populations by means of classical or model-based indicators was out of the scope of this paper, as the number of subjects included is still low. So, no conclusions can be done for the moment on the model parameters altered on diabetic patients. However, this represents one of the future directions of our work. The results presented in this paper are encouraging for the use of this model-based approach in computer-aided diagnosis, and for testing different therapeutic scenarios with a patient-specific model.

Appendix

The Bond Graph Formalism

The Bond Graph (BG) formalism is a diagram-based method that is particularly powerful to represent multienergy systems, as it is based on the representation of power exchanges [45]. Actually, the terminology, the rules, and the construction of Bond Graph models are the same for all energy domains. For example, in the mechanical domain, the effort variable e is the force and the flow variable f is the rate; whereas, in the hydraulic domain, the effort variable e is the pressure and the flow variable f represents flow. The power is the product of the effort and the flow: $P = e \cdot f$. The elements of the Bond Graph language can be classified in the following.

(a) Passive elements R , C , and I :

- (i) resistive element (R): the resistive element R is used to describe dissipative phenomenon and can represent electrical resistors, dashpots, or plugs in fluid lines;
- (ii) capacitive element (C): the capacitive element C is used to describe energy storage and can represent springs or electrical capacitors;
- (iii) inertial element (I): the inertial element I is used to model inductance effects in electrical systems and mass or inertia effects in mechanical or fluid systems.

(b) Active elements: Se and Sf :

- (i) An effort source is an element, which produces an effort, independently of the flow, and a flow source is an element that produces flow independently of the effort.

(c) Junction elements: 0 , 1 , TF , GY :

- (i) 0 junction: the 0 junction is characterized by the equality of the efforts on all its links, while the corresponding flows sum up to zero, if power orientations are taken positive toward the junction;

- (ii) 1 junction: 1 junction is characterized by the equality of the flows on all its links, and the corresponding efforts sum up to zero with the same power orientations;
- (iii) transformer (TF): the transformer TF conserves power and transmits the factors of power with scaling defined by the transformer modulus; it can represent an ideal electrical transformer or a mass-less lever;
- (iv) gyrator (GY): a gyrator establishes a relationship between flow to effort and effort to flow and conserves the power. It can represent a mechanical gyro-scope or an electrical dc motor.

References

- [1] Task Force of the European Society of Cardiology and the North American Society of Pacing and Electrophysiology, "Heart rate variability: standards of measurement, physiological interpretation, and clinical use," *Circulation*, vol. 93, no. 5, pp. 1043–1065, 1996.
- [2] J.-L. Coatrieux and J. Bassingthwaighe, "The physiome and beyond," *Proceedings of the IEEE*, vol. 94, no. 4, pp. 671–677, 2006.
- [3] D. A. Linkens and H. H. Chen, "The design of a bond-graph-based controller for muscle relaxant anaesthesia," in *Proceedings of IEEE International Conference on Systems, Man and Cybernetics: Intelligent Systems for the 21st Century*, vol. 4, pp. 3005–3010, Vancouver, Canada, October 1995.
- [4] L. A. Wojcik, "Modeling of musculoskeletal structure and function using a modular bond graph approach," *Journal of the Franklin Institute*, vol. 340, no. 1, pp. 63–76, 2003.
- [5] M. Diaz-Insua and M. Delgado, "Modeling and simulation of the human cardiovascular system with bond graph: a basic development," in *Proceedings of IEEE Computers in Cardiology Conference*, pp. 393–396, Indianapolis, Ind, USA, September 1996.
- [6] V. A. Diaz-Zuccarini, "Etude des conditions d'efficacité du ventricule gauche par optimisation téléonomique d'un model de son fonctionnement," Ph.D. thesis, Ecole Centrale de Lille, Lille, France, 2003.
- [7] J. Lefèvre, L. Lefèvre, and B. Couteiro, "A bond graph model of chemo-mechanical transduction in the mammalian left ventricle," *Simulation Practice and Theory*, vol. 7, no. 5-6, pp. 531–552, 1999.
- [8] A. L. Bardou, P. M. Auger, P. J. Birkui, and J.-L. Chassé, "Modeling of cardiac electrophysiological mechanisms: from action potential genesis to its propagation in myocardium," *Critical Reviews in Biomedical Engineering*, vol. 24, no. 2-3, pp. 141–221, 1996.
- [9] R. A. FitzHugh, "Impulses and physiological states in theoretical models of nerve membrane," *Biophysical Journal*, vol. 1, no. 6, pp. 445–466, 1961.
- [10] C.-H. Luo and Y. Rudy, "A dynamic model of the cardiac ventricular action potential. II. Afterdepolarizations, triggered activity, and potentiation," *Circulation Research*, vol. 74, no. 6, pp. 1097–1113, 1994.
- [11] P. H. M. Bovendeerd, P. Borsje, T. Arts, and F. N. van de Vosse, "Dependence of intramyocardial pressure and coronary flow on ventricular loading and contractility: a model study," *Annals of Biomedical Engineering*, vol. 34, no. 12, pp. 1833–1845, 2006.
- [12] P. J. Hunter, A. D. McCulloch, and H. E. D. J. ter Keurs, "Modelling the mechanical properties of cardiac muscle," *Progress in Biophysics and Molecular Biology*, vol. 69, no. 2-3, pp. 289–331, 1998.
- [13] J. J. Rice, M. S. Jafri, and R. L. Winslow, "Modeling short-term interval-force relations in cardiac muscle," *American Journal of Physiology: Heart and Circulatory Physiology*, vol. 278, no. 3, pp. H913–H931, 2000.
- [14] J. D. Humphrey, R. K. Strumpf, and F. C. Yin, "Determination of a constitutive relation for passive myocardium—II: parameter estimation," *Journal of Biomechanical Engineering*, vol. 112, no. 3, pp. 340–346, 1990.
- [15] V. P. Novak, F. C. P. Yin, and J. D. Humphrey, "Regional mechanical properties of passive myocardium," *Journal of Biomechanics*, vol. 27, no. 4, pp. 403–412, 1994.
- [16] B. Chahboune and J. M. Crolet, "Numerical simulation of the blood-wall interaction in the human left ventricle," *The European Physical Journal: Applied Physics*, vol. 2, no. 3, pp. 291–297, 1998.
- [17] R. C. P. Kerckhoffs, P. H. M. Bovendeerd, J. C. S. Kotte, F. W. Prinzen, K. Smits, and T. Arts, "Homogeneity of cardiac contraction despite physiological asynchrony of depolarization: a model study," *Annals of Biomedical Engineering*, vol. 31, no. 5, pp. 536–547, 2003.
- [18] M. Nash, "Mechanics and material properties of the heart using an anatomically accurate mathematical model," Ph.D. thesis, University of Auckland, Auckland, New Zealand, 1998.
- [19] M. Sermesant, H. Delingette, and N. Ayache, "An electromechanical model of the heart for image analysis and simulation," *IEEE Transactions on Medical Imaging*, vol. 25, no. 5, pp. 612–625, 2006.
- [20] D. Nickerson, N. Smith, and P. J. Hunter, "New developments in a strongly coupled cardiac electromechanical model," *Europace*, vol. 7, supplement 2, pp. S118–S127, 2005.
- [21] S. W. J. Ubbink, P. H. M. Bovendeerd, T. Delhaas, T. Arts, and F. N. van de Vosse, "Towards model-based analysis of cardiac MR tagging data: relation between left ventricular shear strain and myofiber orientation," *Medical Image Analysis*, vol. 10, no. 4, pp. 632–641, 2006.
- [22] M. Guarini, J. Urzúa, A. Cipriano, and W. González, "Estimation of cardiac function from computer analysis of the arterial pressure waveform," *IEEE Transactions on Biomedical Engineering*, vol. 45, no. 12, pp. 1420–1428, 1998.
- [23] J. L. Palladino and A. Noordergraaf, "A paradigm for quantifying ventricular contraction," *Cellular and Molecular Biology Letters*, vol. 7, no. 2, pp. 331–335, 2002.
- [24] G. W. Beeler and H. Reuter, "Reconstruction of the action potential of ventricular myocardial fibres," *Journal of Physiology*, vol. 268, no. 1, pp. 177–210, 1977.
- [25] P. J. Hunter, S. Sideman, H. Fozzard, et al., "Myocardial constitutive laws for continuum mechanics models of the heart," *Advances in Experimental Medicine and Biology*, vol. 382, pp. 303–318, 1995.
- [26] T. Heldt, E. B. Shim, R. D. Kamm, and R. G. Mark, "Computational modeling of cardiovascular response to orthostatic stress," *Journal of Applied Physiology*, vol. 92, no. 3, pp. 1239–1254, 2002.
- [27] B. McInnis, Z.-W. Guo, P. Lu, and J.-C. Wang, "Adaptive control of left ventricular bypass assist devices," *IEEE Transactions on Automatic Control*, vol. 30, no. 4, pp. 322–329, 1985.
- [28] M. Ursino, "Interaction between carotid baroregulation and the pulsating heart: a mathematical model," *American Journal of Physiology*, vol. 275, no. 5, pp. H1733–H1747, 1998.

- [29] M. S. Olufsen, J. T. Ottesen, H. T. Tran, L. M. Ellwein, L. A. Lipsitz, and V. Novak, "Blood pressure and blood flow variation during postural change from sitting to standing: model development and validation," *Journal of Applied Physiology*, vol. 99, no. 4, pp. 1523–1537, 2005.
- [30] M. Ursino and E. Magosso, "Acute cardiovascular response to isocapnic hypoxia. I. A mathematical model," *American Journal of Physiology*, vol. 279, no. 1, pp. H149–H165, 2000.
- [31] E. Magosso, S. Cavalcanti, and M. Ursino, "Theoretical analysis of rest and exercise hemodynamics in patients with total cavopulmonary connection," *American Journal of Physiology*, vol. 282, no. 3, pp. H1018–H1034, 2002.
- [32] J. B. Olansen, J. W. Clark, D. Khoury, F. Ghorbel, and A. Bidani, "A closed-loop model of the canine cardiovascular system that includes ventricular interaction," *Computers and Biomedical Research*, vol. 33, no. 4, pp. 260–295, 2000.
- [33] A. M. Van Roon, L. J. M. Mulder, M. Althaus, and G. Mulder, "Introducing a baroreflex model for studying cardiovascular effects of mental workload," *Psychophysiology*, vol. 41, no. 6, pp. 961–981, 2004.
- [34] K. Lu, J. W. Clark, F. H. Ghorbel, D. L. Ware, and A. Bidani, "A human cardiopulmonary system model applied to the analysis of the Valsalva maneuver," *American Journal of Physiology*, vol. 281, no. 6, pp. H2661–H2679, 2001.
- [35] G. Baselli, S. Cerutti, S. Civardi, A. Malliani, and M. Pagani, "Cardiovascular variability signals: towards the identification of a closed-loop model of the neural control mechanisms," *IEEE Transactions on Biomedical Engineering*, vol. 35, no. 12, pp. 1033–1046, 1988.
- [36] E. C. Zeeman, "Differential equations for the heartbeat and nerve impulse," in *Dynamical Systems*, pp. 683–741, Academic Press, San Diego, Calif, USA, 1973.
- [37] R. W. deBoer, J. M. Karemaker, and J. Strackee, "Hemodynamic fluctuations and baroreflex sensitivity in humans: a beat-to-beat model," *American Journal of Physiology*, vol. 253, no. 3, pp. H680–H689, 1987.
- [38] H. Seidel and H. Herzel, "Modelling heart rate variability due to respiration and baroreflex," in *Modelling the Dynamics of Biological Systems*, pp. 205–229, Springer, Berlin, Germany, 1995.
- [39] K. H. Wesseling and J. J. Settels, "Baromodulation explains short-term blood pressure variability," in *Psychophysiology of Cardiovascular Control*, pp. 69–97, Plenum Press, New York, NY, USA, 1985.
- [40] O. Rompelman, A. J. Coenen, and R. I. Kitney, "Measurement of heart-rate variability—part 1: comparative study of heart-rate variability analysis methods," *Medical and Biological Engineering and Computing*, vol. 15, no. 3, pp. 233–239, 1977.
- [41] J. H. Holland, *Adaptation in Natural and Artificial Systems*, MIT Press, Cambridge, Mass, USA, 1975.
- [42] D. Beasley, D. R. Bull, and R. R. Martin, "An overview of genetic algorithms: part 1, fundamental," *University Computing*, vol. 15, no. 2, pp. 58–69, 1993.
- [43] D. E. Goldberg, *Genetic Algorithms in Search, Optimization and Machine Learning*, Addison-Wesley, Boston, Mass, USA, 1989.
- [44] Z. Michalewicz, *Genetic Algorithms + Data Structures = Evolution Programs*, Springer, New York, NY, USA, 1994.
- [45] G. Dauphin-Tanguy, *Les Bond Graphs*, Hermes, Paris, France, 2000.

Research Article

Experimental and Numerical Modeling of Screws Used for Rigid Internal Fixation of Mandibular Fractures

Naresh Chaudhary,¹ Scott T. Lovald,² Jon Wagner,³ Tariq Khraishi,² and Bret Baack³

¹ *Manufacturing Engineering Program, University of New Mexico, Albuquerque, NM 87131, USA*

² *Mechanical Engineering Department, University of New Mexico, Albuquerque, NM 87131, USA*

³ *Department of Surgery, University of New Mexico, Albuquerque, NM 87131, USA*

Correspondence should be addressed to Tariq Khraishi, khraishi@unm.edu

Received 1 September 2007; Revised 2 January 2008; Accepted 6 February 2008

Recommended by Ewa Pietka

Experimental and numerical methods are used to explore the stresses generated around bone screws used in rigid internal fixation of mandibular fractures. These results are intended to aid in decisions concerning both the design and the use of these bone screws. A finite element (FE) model of a human mandible is created with a fixated fracture in the parasymphyseal region. The mandibular model is anatomically loaded, and the forces exerted by the fixation plate onto the simplified screws are obtained and transferred to another finite element submodel of a screw implant embedded in a trilaminar block with material properties of cortical and cancellous bone. The stress in the bone surrounding the screw implant is obtained and compared for different screw configurations. The submodel analyses are further compared to and validated with simple axial experimental and numerical screw pull-out models. Results of the screw FE analysis (FEA) submodel show that a unicortical screw of 2.6 mm major diameter and 1.0 mm pitch will cause less bone damage than a bicortical screw of 2.3 mm major diameter and 1.0 mm pitch. The results of this study suggest that bicortical drilling can be avoided by using screws of a larger major diameter.

Copyright © 2008 Naresh Chaudhary et al. This is an open access article distributed under the Creative Commons Attribution License, which permits unrestricted use, distribution, and reproduction in any medium, provided the original work is properly cited.

1. Introduction

Failure of bone screws used for fracture fixation in trauma surgeries is a significant problem that has been examined previously. Rigid internal fixation (RIF) of mandibular fractures has been a focus of studies on screw performance due to the mandible's load bearing function and the rate of complication seen with these types of surgery. Screw failure in mandibular bone is undesirable as any movement of the mandible in the presence of a foreign body can lead to infection. Tada [1] stated that inappropriate loading can cause excessive stress in the bone around a foreign implant and may result in bone resorption. Screw loosening not only increases the chance of infection at the screw failure site but creates a less stable environment for fracture healing. Murthy [2] and Gabrielli [3] have both stated that stability in the fracture region can aid in defending against infection. Infection reduces oxygenation to the fracture site creating an environment more conducive to fibrous union than bone deposition. The result of this

activity is that infection leads to more serious complications including debilitating pain, malunion, nonunion, chronic osteomyelitis, and acquired skeletal deformities [4]. Complications of this nature can in some cases require a second surgery.

The most pertinent metric to measure the success of a bone screw has traditionally been the pullout or holding strength of the screw when seated in bone [5]. In such mechanical assemblies, there will be some sort of internally and/or externally generated forces on these screws that can encourage failure of either the screw or the surrounding bone. Each bone screw has design parameters that may affect the likelihood of screw implant failure. One of the most important considerations is the decision to use bicortical or unicortical fixation. Bicortical fixation utilizes longer screws that are seated within both the buccal and lingual cortices while unicortical fixation uses shorter screws that are seated only in the buccal section of cortical bone. Utilization of bicortical screws stems from the common belief that a bicortically drilled screw can sustain a stronger load before

failure. However, a bicortical fixation also means longer surgical times and increased chance of complications due to higher probability of interference with the dental segment and the inferior alveolar nerve. Unicortical fixations, on the other hand, are less time consuming and avoid interference with the dental segment and the inferior alveolar nerve. It is important to have an understanding of the effect of screw length, as well as other design parameters, for a surgeon to make a judicious decision of the level of intrusion necessary to safely fixate a mandibular fracture.

Previous research has yielded many insightful observations into the modes of bone screw failure and the effect of certain design parameters for different types of bone screws. Skinner [6] compared four different types of screws used in transpedicular screw fixation. They observed an increase in the pull-out strength due to an increase in the screw diameter and an increase in displacement before failure resulting from an increase in the screw pitch. Complete failure occurred when a sharp-threaded screw was pulled out one whole pitch distance, an observation also reported by Ryken [7] using cervical plate screws. Another study by Ryken [8] suggested that bicortical screw insertion provides more holding than unicortical insertion while also finding a direct correlation between the bone mineral density (BMD) of the surrounding bone and the screw pull-out strength. Using Casper cervical screws, Maiman [9] observed that cancellous bone remained on screw threads after failure, but that posterior cortical penetration does not improve pull-out strength. With regard to smaller screws used in mandibular and maxilla fracture fixation, Boyle [10] suggested that 2.7 mm diameter screws do not have an advantage over 2.0 mm screws when seated in thin porcine rib, while at least three self-tapping threads should be used for maximum retention. A similar conclusion was also reached by Phillips [11]. Although a wealth of information exists on screw pull-out studies, there have been no studies that have completed a thorough analysis of screws used in *mandibular* fracture repair. To the authors' knowledge, this would be the first such study.

The first focus of the current study is to perform screw pull-out using mandibular bone screws in a trilaminar block with sections representing material properties closely resembling two sections/layers of cortical bone sandwiching a section of cancellous bone. This provides a more realistic determination of the effect of bone screw design parameters than using a single layer of continuous material. Screws will be experimentally pulled out of the trilaminar block to observe actual modes of screw failure before a FE model will simulate the experimental testing. The FE model gives flexibility towards discovering the effects of different design parameters on the pull-out strength. This is the first known correlated attempt to perform both experimental and simulated screw pull-out testing on a trilaminar material closely resembling layers of cortical and cancellous bone.

While both experimental testing and finite element analysis of screw loading and failure have received some attention, the natural loading on mandibular implant screws during mastication *has not yet been reported*. Previous studies

have shown that FEA of screw pull-out testing can be both validated by experiment, and it is a useful design tool when looking at stress and strain generated around screw implants [1]. The value of these studies has so far been limited by the generally unknown forces on the screws implants in actual patients.

Recently, work by Cox [12], Fernández [13], Wagner [14], and Lovald [15, 16] has shown that finite element analysis (FEA) of the entire mandible can mimic natural human loading on a fractured mandible and can determine the stress and strain fields within the bone and implant devices as well as the forces generated on the screw implants. Given the size and complexity of these models, simplifications are often required in representing the bone screws. Wagner and Cox neglected the screws, bonding the plate directly to mandibular bone. Lovald used cylinders in place of threaded screws. While these models were able to determine stress in the fixation plate and fracture mobility, they did not yield accurate results pertaining to the stresses in cortical and cancellous bone emanating from a *threaded* screw.

The second focus of the current study enhances work on both studies of screw pull-out FEA and mandibular fracture fixation FEA by translating three-dimensional forces from a mandibular FE model to a screw FE submodel considering bone screw embedded in a trilaminar bone material. The comparison will use von Mises stress in the cortical bone surrounding the screws. Stress in the bone surrounding the seated screw can lead to screw failure and the complications described previously. Von Mises criterion was chosen in order to be consistent with prior studies of similar nature [1, 12–15]. Using the boundary conditions from the mandibular FEA model, the effect of certain screw design parameters, including bicortical versus unicortical fixation, will once again be explored. To simplify the second part of this study, parameters determined optimal during the first part of the study will be used. Design parameter analysis will be focused on four configurations with differing screw lengths, pitches, and major diameters.

2. Materials and Methods

The current study has three components:

- (i) validation and design parameter analysis of experimental and numerical screw pull-out from a trilaminar block with properties of cortical and cancellous bone;
- (ii) determination of forces applied to screw implants during natural human loading using FEA of a fractured and fixated human mandible;
- (iii) application of the determined forces in component (ii) to a numerical analysis submodel of a screw embedded in a trilaminar block from component (i).

The methods section is broken into the three respective subsections.

2.1. Experimental and Numerical Analysis of Screw Pull-out

2.1.1. Experimental Screw Pull-out

The experimental tests were done using bone screws embedded in a trilaminate standard polyurethane block. The polyurethane block has two outer cortical layers and a middle cancellous layer, each 3.0 mm thick, mimicking mandibular bone. The material properties of these layers were synthesized to closely match mandibular bone properties (Pacific Research Laboratories, Inc., Vashon, Wash, USA). The dimensions of the block for all experiments are 15 mm × 15 mm × 9 mm. Apart from having realistic material properties, these “artificial bone” samples are less expensive, exhibit homogenous properties over a layer, and are easy to manipulate for experiment.

After drilling a pilot hole, titanium self-tapping screws were inserted either completely for bicortical seating, or up to the cancellous layer for unicortical seating. Self-tapping screws eliminate the separate tapping requirement for surgical screw insertion. The self-tapping screws are provided by the Leibinger Micro Implants (Stryker Corporation, Kalamazoo, Mich, USA).

The pull-out experiments were carried out on an Instron machine (4400R controller model). Figure 1(a) shows the experimental setup. The specimen is held by clamps in a specially designed vise. The screw is held in a jig such that the screw head rests on the seat provided in the jig. This jig is mounted on the stationary end, which is the Instron machine’s upper crossbar. The lower crossbar of the Instron, to which the vise is attached, is then gradually pulled down at a speed of 5 mm/min till the screw disengages completely from the block. Computer data acquisition recorded all the forces and displacements during the testing.

2.1.2. Polishing of the Experimental Specimen

The failure of the screw-bone interface is hypothesized to start long before the screw is completely pulled out of the block. Therefore, to verify the hypothesis, it is important to do a micro examination of bone damage at loads well below the maximum pull-out load encountered. This is done by taking partially pulled specimen and grinding them finely for examination under a high-resolution microscope. Using the mean failure load data from the pull-out experiments, different polished samples were obtained at different loads. A specimen was then ground on various abrasive grits, rough to fine, till the specimen was sectioned in half.

2.1.3. Numerical Analysis of Screw Pull-out

2.1.3.1. Geometry Creation

The 3D CAD modeling system Pro/ENGINEER Wildfire (PTC, Needham, Mass, USA) was used to build a model of a trilaminate mandibular bone specimen with an embedded screw implant. Finite element analysis (FEA)

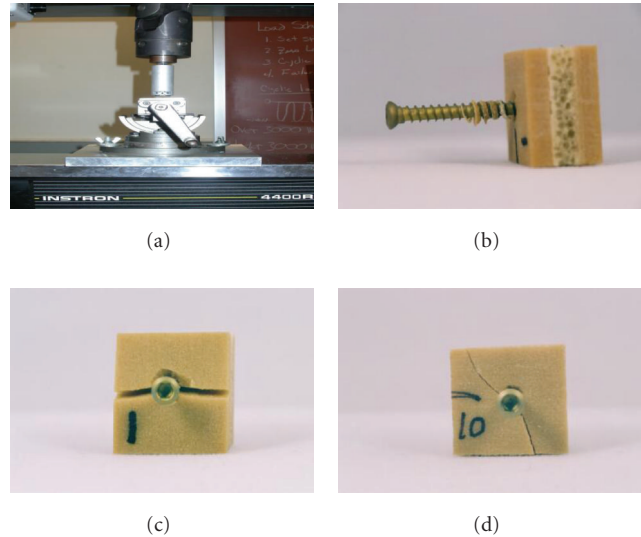


FIGURE 1: (a) Experimental setup for the pull-out tests, (b) typical specimen after cylindrical failure with material trapped between screw threads, (c) pull-out specimen with vertical cracks, and (d) pull-out specimen with diagonal cracks.

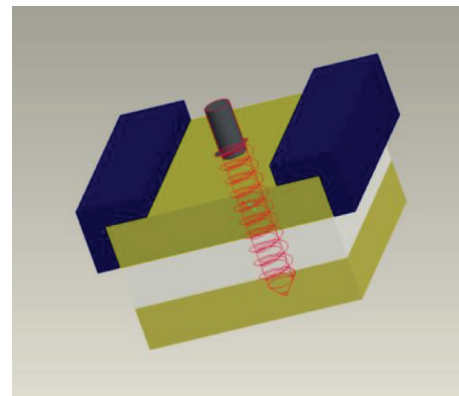


FIGURE 2: The Pro/E 3D assembly for the screw-pull out finite element analysis.

of a simulated screw pull-out process was carried out using the Pro/Mechanica software, which is companion software to Pro/ENGINEER Wildfire. Geometrical data for the screws was provided by the Stryker-Leibinger Corp. (Kalamazoo, Mich, USA).

To simplify the model, the trilaminate bone specimen is modeled as a cuboid (Figure 2). The trilaminate block is modeled as a 15 mm × 15 mm square with three 3 mm thick layers of outer cortical bone and inner cancellous bone. These layers are perfectly bonded to one another. Aluminum clamps of dimensions 15.0 mm × 3.5 mm × 2.0 mm were placed on the top edges of the block to mimic the experimental vise. The screw hole in the block is a direct replica of the screw geometry to facilitate CAD assembly. Titanium screws were inserted into the drilled blocks and assumed to be perfectly bonded to the block material.

TABLE 1: Material properties used in the numerical analysis of the screw pull-out.

Material properties for screw pull-out FEA		
	Elastic modulus (GPa)	Poisson's ratio
Bone screw	113.800	0.342
Cortical block layer	1.190	0.300
Cancellous block layer	0.267	0.300
Aluminum clamps	69.000	0.300

2.1.3.2. Material Properties

All materials are assumed to be linear elastic and isotropic. The material properties were taken directly from the respective manufacturers of the bone screws and the synthetic trilinear block material. Table 1 gives the material properties used in the screw pull-out FEA.

2.1.3.3. Boundary Conditions

The boundary conditions for the numerical analysis are meant to mimic the experiment. The top face of the screw was constrained from movement in all directions. A constant force of 600N is applied upon the top sides of the aluminum clamps in a downward direction.

The model was solved numerically for various parameters to study the effects of screw pitch, major diameter, and thread depth on the pull-out strength. The parameter values are as follows: major diameter: 2.0, 2.3, and 2.6 mm; pitch: 1.0, 1.2, and 1.4 mm; thread depth: 0.2, 0.3, and 0.4 mm. Each of these parameters was varied during the study using baseline values of 2.3 mm for the major diameter, 1.0 mm for the pitch, and 0.3 mm for the thread depth.

2.2. FEA of a Fractured Mandible

2.2.1. Mandibular FEA Geometry Creation

Computerized tomography scans of a 22-year-old male were obtained from a Siemens Somatone Sensations Multislice Scanner. The patient had full dentition and normal occlusion. The scans were imported into Mimics 7.3 (Materialise, Ann Arbor, Mich, USA) where thresholding and editing functions were used to create entities for cortical bone, cancellous bone, and the dental segment. Initial graphics exchange specification (IGES) curves were approximated around the volumes and imported into ANSYS 8.0. Volumes were created and subsequently bonded in the symphysis, parasymphysis, body, angle, ramus, coronoid, and condyle regions using their respective IGES curves.

The volumes created were meshed using tetrahedral-shaped solid elements. The final mesh of the mandible with hardware consisted of 67 434 elements and 107 352 nodes. Mesh refinement was used in the plate, screws, fracture region, and the surrounding cortical and cancellous regions until convergence of all pertinent measures was established. A consistent mesh size was used in all analyses. Geometric information from the finite element model was

compared to the original CT scan data to ensure model validity. Furthermore, loadings similar to previous studies were mimicked in order to validate stress results. CAD model verification for this study was detailed in Chaudhary [17] and Lovald [15, 18].

The fracture was simulated as a 2 mm thick linear fracture in the parasymphyseal region. The symphysis of the mandible is the region of the junction of the two symmetrical halves near the sagittal plane. Geometrical data for the plate was provided by the Stryker-Leibinger Corp. (Kalamazoo, Mich, USA). The plate analyzed is the 3D Matrix 4 × 2 Hole Mini Plate. There is a small amount of clearance between the modeled plate and bone, as in clinical situations. Unicortical screw fixation was used on the superior border while bicortical fixation was used on the inferior border. Screws were simulated as solid cylinders with a diameter of 2.3 mm that were inserted and bonded into the bone material.

2.2.2. Material Properties

The finite element (FE) model of the dentate mandible consists of the following materials: cortical bone, cancellous bone, and dental segment (dentin, enamel, and periodontal ligament). Coordinate systems and orthotropic properties for cortical bone only were designated in each of 12 mandibular volumes created and mentioned previously. Table 2 gives the material properties for the mandibular FEA. The orthotropic cortical bone values were taken from a study by Schwartz-Dabney and Dechow [19]. Isotropic properties for cancellous bone were taken from [13]. The properties for dentin were taken from another finite element study [20], and they correlate well with a study by Craig and Peyton [21]. In the current study, only material properties for dentin are modeled in the dental segment due to its high modulus of elasticity. The fracture region was given properties of initial connective tissue [22] (Young's modulus of 3 MPa and Poisson's ratio of 0.4). The properties of titanium plates and screws were taken from another FE study of mandibular angle fractures [12].

2.2.3. Boundary Conditions

The bite force used in this FEA was a unilateral molar clench. Muscle force vectors that were experimentally derived for that specific bite are distributed around the mandible. Each force has a direction, area of attachment, and magnitude. The magnitude and direction of muscle forces during the simulated bite were obtained from Koriath et al. [20] and are detailed in Lovald et al. [15]. The data from this reference pertains to the bite of a healthy adult with an intact mandible. It is estimated that the bite force of a patient with a fractured mandible is 60% of that of a healthy adult [23]. The bite force data was modified accordingly in this study. The muscle attachment areas on the mandible were obtained from [24]. Both condyles and the occlusal surface of the right first molar are restrained from movement in all directions. Figure 3 shows the meshed mandibular model.

TABLE 2: Material properties used in FEA of the mandible. Orthotropic properties were used for cortical bone, while isotropic properties were used for cancellous bone, dentin, and the titanium plate. The x -direction is along the length of the mandible, the y -direction is normal to the bone plane, and the z -direction is their cross product.

Material properties	Symphysis	Parasymphysis	Angle	Ramus	Condyle	Coronoid	Cancellous	Dentin	Titanium
E_x (MPa)	20 492	21 728	23 793	24 607	23 500	28 000	7 930	17 600	110 000
E_y (MPa)	12 092	12 700	12 757	12 971	12 650	14 000	7 930	17 600	110 000
E_z (MPa)	16 350	17 828	19 014	18 357	17 850	17 500	7 930	17 600	110 000
ν_{xy}	0.43	0.45	0.41	0.38	0.32	0.28	0.3	0.34	0.34
ν_{yz}	0.22	0.2	0.22	0.23	0.25	0.28	0.3	0.34	0.34
ν_{xz}	0.34	0.34	0.3	0.28	0.24	0.23	0.3	0.34	0.34
G_{xy} (MPa)	5 317	5 533	5 493	5 386	5 500	5 750	3 050	6 567	41 045
G_{yz} (MPa)	4 825	5 083	4 986	5 014	5 150	5 300	3 050	6 567	41 045
G_{xz} (MPa)	6 908	7 450	7 579	7 407	7 150	7 150	3 050	6 567	41 045

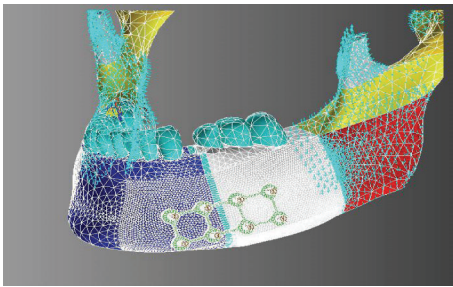


FIGURE 3: Meshed mandibular model showing a parasymphyseal fracture, fixation plates and screws, and different material regions for orthotropic material properties.

2.3. Submodel FEA of a Threaded Screw

2.3.1. Geometry Creation

Geometry used in the screw FEA submodel is nearly identical to that described in Section 2.1.3.1. To simplify the modeling, the aluminum clamps were not modeled.

2.3.2. Material Properties

The material properties in the screw FEA submodel are identical to those of the mandibular FEA from Section 2.2. The outer layers of the trilaminar block are assumed to be orthotropic and are taken directly from the material properties of the parasymphyseal region from the mandibular FEA. To the authors' knowledge, this is the first FE study of screw pull-out using orthotropic cortical bone properties. The inner section of the trilaminar block was assumed to be isotropic and was given material properties of cancellous bone. The screw implant was given material properties of titanium. All material properties for the screw FEA submodel are given in Table 2.

2.3.3. Boundary Conditions

This submodel trilaminar block was restrained from movement in three directions on its four sides. A force, obtained from the mandibular FEA in Section 2.2, was applied to the

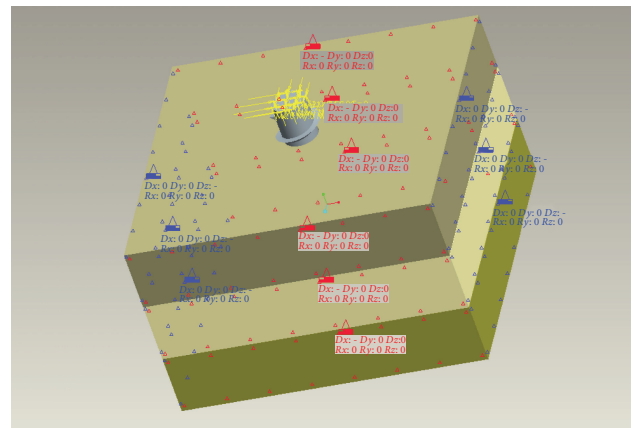


FIGURE 4: The 3D Pro/E assembly with boundary conditions. The bone layers are treated as orthotropic.

TABLE 3: Different screw configurations used in the FEA screw submodel.

Fixation	Major diameter (mm)	Pitch (mm)
Bicortical	2.3	1.0
Unicortical	2.3	1.0
Unicortical	2.3	1.2
Unicortical	2.6	1.0

top surface of the screw implant (Figure 4). The force of the particular screw which showed the highest magnitude in the mandibular FEA was the only force applied to the screw FEA submodel. The same constitutive equations as in Sections 2.1.3.2 and 2.2.2 apply also here to the screw pull-out submodeling.

This screw FEA submodel setup was utilized to compare different screw design configurations. Table 3 shows the configurations for each analysis. The bicortical screw configuration was considered the base analysis. The other configurations were analyzed to compare with the bicortical screw configuration. A thread depth of 0.3 mm was held constant throughout all analyses. All screw parameter configurations are commercially available.

3. Results

3.1. Experimental and Numerical Analysis of Screw Pull-out

3.1.1. Experimental Screw Pull-out

The experimental results were dependent on how the screw exactly failed. Three different modes of failure were observed:

- (i) *cylindrical failure* (Figure 1(b)): in this scenario, the screw pulls out from the block with a significant amount of material trapped between the threads. Samples showing this type of failure have an average pull-out force that is greater than samples in the following scenarios. Samples with cylindrical failure exhibit smooth load-displacement curves, with single maxima (i.e., the lower curve in Figure 5);
- (ii) *failure with vertical cracks* (Figure 1(c)): the block samples show cracks normal to the clamp faces. Wide vertical cracks appear on the top surface of the block. Generally, crackling sounds preceded and accompanied the failure. The cracking of this nature is thought to be due to bending of the block. This assumption is supported by the fact that these cracks were predominant when larger block sizes were used. The curves in this case are jagged with multiple peaks (i.e., multiple local maxima);
- (iii) *failure with diagonal cracks* (Figure 1(d)): these samples show cracks on the top surface of the block that propagate from the circumference of the screw to the corner of the clamp and they are narrow in comparison to the vertical cracks. The curves in this case are not seen to be as jagged as those of the vertical crack.

The experimental load-displacement curves for the bicortical and unicortical screws show a very consistent trend or characteristic shape for cylindrical type failure (similar to the lower curve in Figure 5). The curves in Figure 5 were obtained using 2.3 mm major diameter screws with 1.0 mm pitch. The curve can be divided into three different regions. Region 1 represents a presumably elastic region. Region 2 is predicted to contain the start of plastic deformation through the formation and growth of microcracks. Region 3 is the failure region with macrocracks clearly visible on the surface of the block.

The pull-out experiments were carried out with a sample size of 15 specimens for each of the unicortical and bicortical studies. Results for maximum load and maximum displacement are shown in Table 4. Bicortical fixation is shown to have a higher pull-out strength than unicortical fixation, similar to findings by various works on *other* types of surgical screws [7, 8].

The mean displacement to failure in the case of unicortical pull-out was approximately equal to the pitch of the screw used, similar to findings by Ryken [7]. However, the study by Ryken showed that bicortical screws had a mean displacement to failure greater than unicortical screws

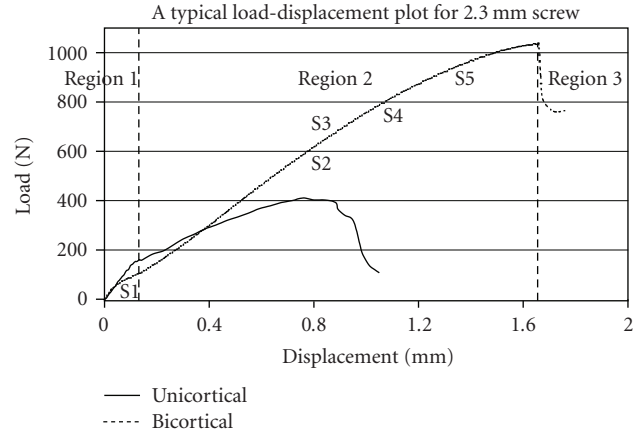


FIGURE 5: Graph showing typical load-displacement curves for bicortical and unicortical pull-outs. Results were taken for screws with a 2.3 mm major diameter and a 1.0 mm pitch. Three different regions are denoted from which specimens were taken for polishing.

TABLE 4: Load and displacement results for the screw pull-out experiments.

		Mean	St. Dev.
Bicortical screw	Global maximum load (N)	975.02	83.15
	Displacement (mm)	1.61	0.20
Unicortical screw	Global maximum load (N)	372.96	38.77
	Displacement (mm)	0.96	0.24

by approximately 8%. This is in contrast to results from the current study which shows about a 67% increase. These studies differed in the tested material, the screw type/geometry, the pull-out rate, and the flex within the experimental setup, which all can alter the pull-out force [25]. While Ryken focused on cervical plate screws, the current study is deemed more appropriate pertaining to screws used in the rigid fixation of mandibular fractures.

3.1.2. Polishing

Five different samples, labeled S1, S2, S3, S4, and S5 (see Figure 5), were sectioned and polished to reveal their interior damage state. Specimen S1 showed no observed microdamage at magnification of 400X. S1 lies within an elastic region (Region 1) which exhibits linear behavior. Specimen S2 was just past the elastic region but it was not associated with macro surface cracks (Figure 6(a)). The image of specimen S3 is shown in Figure 6(b). Shearing of the cortical material can be seen near the top part of the image. With increased load the screw is slowly pulled out until the uppermost thread chips off the material (Figure 6(b)). For specimen S4, in addition to the failure seen in S3, the bone undergoes microcracking (Figure 6(c)) at the thread immediately inferior to the uppermost thread.

At higher loads, near S5, microcracking also takes place in the lower cortical layer as well (Figure 6(d)). It is worthy to mention, from the polished specimens, that crack formation

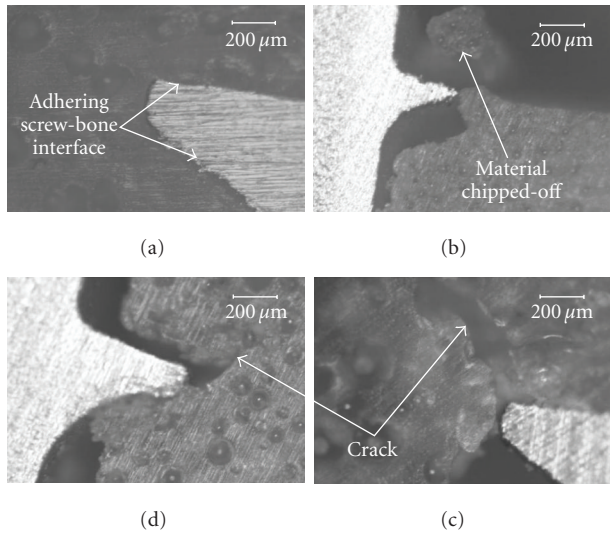


FIGURE 6: Images of polished specimens showing the thread-block interface for the following loads: (a) 566.4N and magnification of 200X (specimen S2), (b) 684.6N and magnification of 50X (specimen S3), (c) 783.9N and magnification of 200X (specimen S4), and (d) 891.3N and magnification of 100X (specimen S5).

always seems to start near the uppermost thread in both the upper and lower cortical layers.

3.1.3. Numerical Screw Pull-out

General stress contours for all screws analyzed are first discussed. Figure 7(a) shows a typical distribution of von Mises stress in the block for the numerical analysis using a load of 600N. Stress concentration occurs in the block material immediately surrounding the screw threads with the highest stress region observed near the top surface of the block. This finding is consistent with another work by the authors in which 3D finite element modeling was performed on a fractured mandible that was fixated with a common plating configuration [15]. It is also consistent with damage occurring near the top surface as found in the above microscopic studies. In the current work, the stress concentration on the top surface was found to be traversing in a direction diagonal to the block. This was clear at higher loads and conforms to experimental observations as almost all of the bicortical, and some of the unicortical specimens, failed with diagonal surface cracks.

Figures 7(b) and 7(d) show plots depicting stress distribution along diagonal and frontal sectional views. The stress is seen to concentrate along the screw-block interface and in the general vicinity of the screw. Measurements suggest that inserted surgical screws separated by a diameter or more would have little interaction between their respective stress fields.

Figure 7(c) shows a typical volumetric contour plot. The plot shows only the material surrounding the screw that is stressed above a certain threshold of von Mises stress. As mentioned in earlier sections, most test failures occur in such

a way that the screw comes off from the block with cortical material entrapped between its threads. This type of failure was hence referred to as “cylindrical failure.” Figures 7(b), 7(c), and 7(d) show the screw surrounded by a cylindrical envelope of the block material with the highest stress. This is consistent with the experimentally observed cylindrical failures.

Seven different parametric cases were studied using the finite element model for both bicortical and unicortical setups. Each case had a different combination of major diameter, pitch, and thread depth. The base case represents a major diameter of 2.3 mm, a pitch of 1.0 mm, and a screw depth of 0.3 mm. All of these base case numbers are standard for surgical screws (taken with permission from Stryker Corporation, Kalamazoo, Mich, USA). Note that every time a parameter (e.g., major diameter) was varied, all other parameters were held constant (e.g., pitch and screw depth). For a given case, von Mises stresses are interrogated from the highest stress level, which occurs near the top screw thread, down to a stress level, which *completely* envelops the screw. At this stress level, which we term the “envelope stress,” the stress at any material point within this envelope will be equal or higher than this value up to the maximum stress level near the uppermost thread. The envelope stress essentially describes the weakest point before cylindrical failure, and it is used here to weigh the varying screw parameters. A lower value of the “envelope stress” is desirable when considering the different bone screws.

The plots in Figure 8 depict the effect of screw parameters of both bicortical and unicortical screws on the screw envelope stress. Figure 8(a) shows the effect of the different parameters on the unicortical pull-out. The most optimal conditions pertaining to envelope stress were a larger major diameter and a larger thread depth. Interestingly, it was found that a small screw diameter also has a desirable “envelope stress,” but it was associated with a higher stress measure at the top surface when compared to the effect of other parameters. Change in screw pitch affected the envelope stress less than the other screw parameters.

Figure 8(b) shows the effects of various screw parameters on the pull-out envelope stress of the bicortical samples. Optimal conditions suggest a smaller pitch and a large major diameter. This is different than in the unicortical results, where the pitch did not largely affect the stress. A deeper thread depth seems to have lower “envelope stress,” but it was found to have very high localized stress at the top surface of the block, again differing from the unicortical screw results. A deeper thread depth appears to be unfavorable in the bicortical case. Similar to the unicortical sample conclusion, a large screw diameter has a positive effect with a low stress value for the “envelope stress” plot.

3.2. Mandibular Finite Element Analysis

Results for the forces transmitted upon mastication from the fixation plate to the screw implant were obtained for the four screw implants most proximal to the fracture (Table 5). The x , y , and z axes correspond to the orthotropic material axes described in Section 2.2.2, with the positive y direction

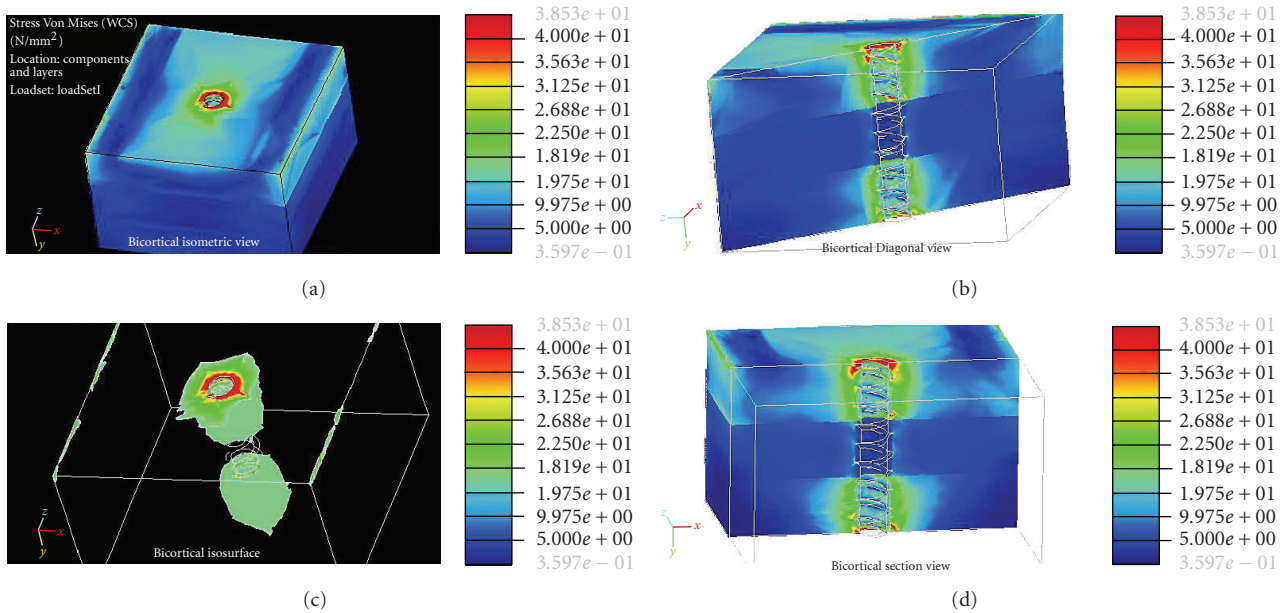


FIGURE 7: Plots of von Mises stress (MPa) in a typical trilaminated block. The four views shown are (clockwise from top-left): (a) isometric view, (b) diagonal section view, (c) volumetric contours, and (d) section view.

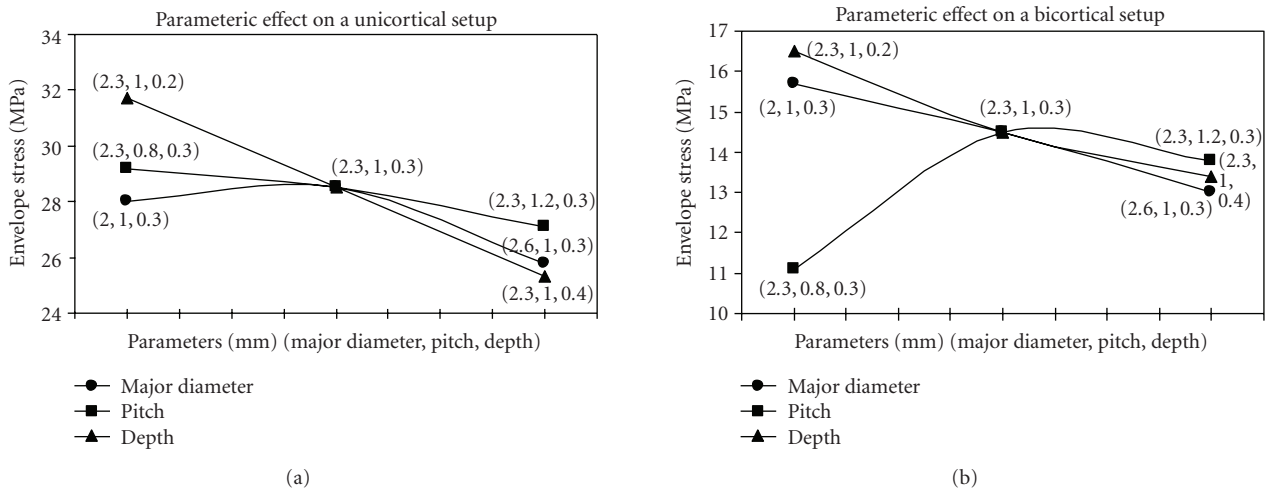


FIGURE 8: Plots showing the “envelope stress” for unicortical and bicortical setups.

corresponding to the pull-out direction (normal to the bone surface). A negative y direction refers to a “pushing in” of the screw implant. Only the maximum “pulling out” force was considered for the screw FEA submodel.

These results were translated into relevant loadings and applied to a threaded screw implant submodel in order to compare the effect of different screw configurations on stresses induced in the bone in which they are seated. The study was undertaken to gather information that will aid the design and use of screw implants in rigid internal fixation of mandibular fractures. The results gathered are expected to be more relevant than linear screw pull-out numerical analyses.

The results of the mandibular FEA show the forces applied to the four screw implants most proximal to the fracture. The maximum pull-out force seen from the current

TABLE 5: Force components (N) applied to the screw implants by the fixation plate in FEA of a fractured and fixated mandible. The x -direction is along the length of the mandible, y is normal to the bone plane, and the z -direction is their cross product.

Screw location	x	y	z
Superior posterior medial	55.3	-13.2	39.4
Superior anterior medial	-57.6	8.9	-26.3
Inferior posterior medial	-67.6	-16.4	22.2
Inferior anterior medial	51.0	21.8	-30.0

mandibular FEA is 21.8N. This is considerably less than the forces leading to failure in the experimental pull-out analyses. We see further that the transverse forces (in the x

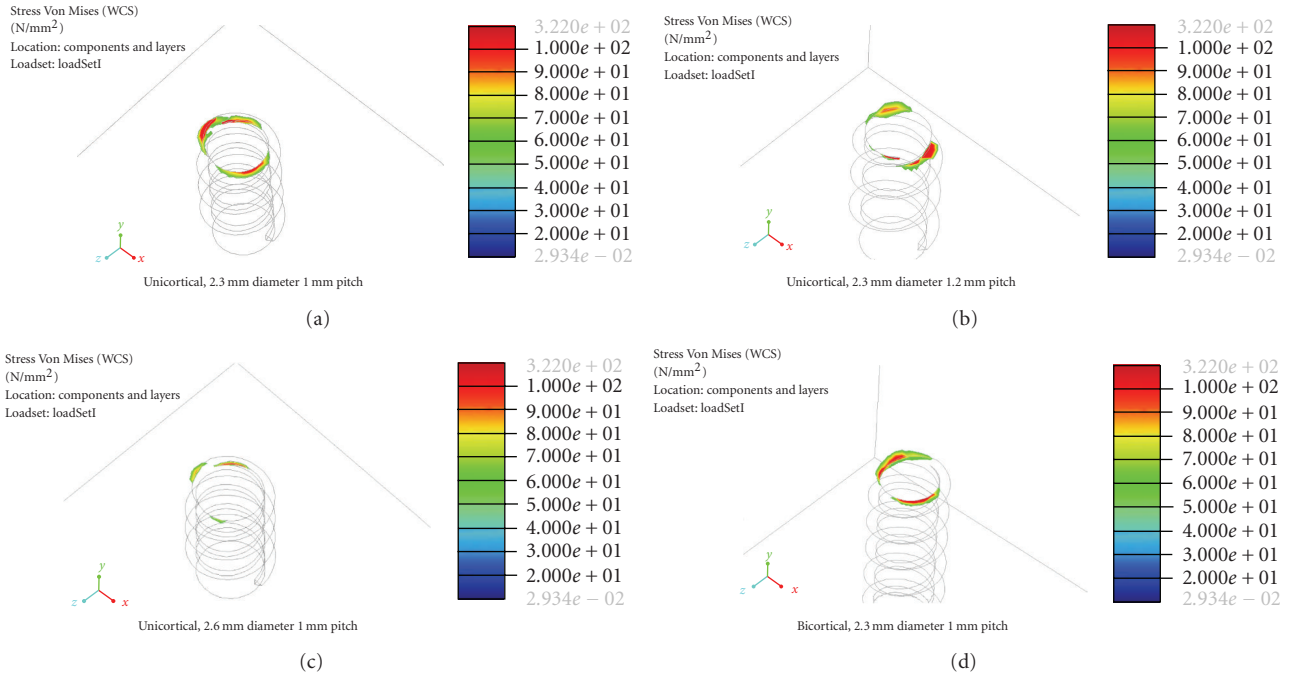


FIGURE 9: An isometric plot of the von Mises stress in bone surrounding the 4 configurations of screw implants. The plot shows only stresses above a 60 MPa threshold.

TABLE 6: Peak von Mises stress in the bone surrounding screw implants for the four different screw configurations.

Fixation	Major diameter (mm)	Pitch (mm)	Peak von Mises Stress (MPa)
Bicortical	2.3	1.0	147
Unicortical	2.3	1.0	322
Unicortical	2.3	1.2	226
Unicortical	2.6	1.0	106

and z directions) are the dominant loads upon screws used in the fixation of mandibular fractures, which is *contrary* to *all* pull-out experiments in the literature focusing solely on the axial direction.

3.3. Screw FEA Submodel

Results were obtained for von Mises stress in the bone surrounding the screw implant for the screw FEA submodel. Figure 9 shows an isometric plot of the von Mises stress in the bone for all four screw configurations analyzed. The isometric plot shows only the material that is stressed beyond what is considered the failure stress of the bone material. Frost suggested this failure stress is 60 MPa [26]. The maximum error limit for all numerical analyses was 2% of maximum principal stress.

To simplify the comparison, the peak von Mises stress was obtained from the analyses for the four different screw configurations under the described loading. Table 6 contains these peak stresses for the four screw configurations.

Applying clinically relevant forces elucidates the true effect of screw parameters on their fixation capabilities for mandibular fractures. Like previous works, including previously in this work, the highest stresses were located

nearest to the cortical bone surface, where the implant first enters the bone material [1, 15, 16]. Peak stress was the lowest in the unicortical screw of 2.6 mm major diameter (Table 6). This outperforms even the bicortically fixed screw configuration. Results from Figure 9 support this conclusion. It is clearly shown that the 2.6 mm unicortical screw has the least amount of material that is above the specified failure threshold. Based on stress results, this evidence suggests that surgeons could avoid bicortical drilling by using unicortical screws with a larger major diameter. This is fortunate as the likelihood of nerve and dental segment interference can be significantly reduced without the need to penetrate past the outer cortical shell of the mandibular corpus.

Tada [1] reported that implant length was a factor in analyses mimicking poor bone quality and pure axial loading. While their study focused on dental implants, loadings were similar in nature to those of experimental screw testing. Less of an affect was seen in bone modeled as having good quality and in analyses undergoing transverse loading. Similarly Van Steenburgh [27] found that the length did not affect the success rate in patients with good quality bone. The current study only considers bone of good quality, and the loading applied here has a much higher transverse component relative to the axial component. Both of these are

conductive to results unaffected by implant insertion length. While the loading of the current study is considered more relevant than previous works, the effect of bone quality on the results is not within the current scope.

Readers should be informed in putting too much confidence into quantitative results from FE analyses of this type. There is a large range of possible inputs into mandibular FEA considering the different bone material properties, bite force magnitudes, fracture locations, and jaw geometries among patients, to name just a few variable patient parameters. Nonetheless, comparisons between different screw configurations based on peak stress and the amount of material that is predicted to fail given a failure stress threshold offer qualitative insight that can aid both screw design and craniomaxillofacial surgical practice.

4. Conclusions

The current study used experimental screw pull-out tests, finite element analysis (FEA) of detailed screw pull-out models, and FEA of a fractured and fixated mandible to determine the effect of bone screw design parameters on stresses generated in bone surrounding screw implants used in patients treated with open reduction and internal fixation (ORIF) of mandible fractures. Results from the experimental and numerical screw pull out tests correlated well. The parametric numerical analyses gave differing conclusions pertaining to screw thread depth and pitch for the unicortical and bicortical screws but concluded that the major diameter is relevant in reducing high stress in the surrounding bone. Results of the mandibular FEA suggest that transversely applied forces are dominant upon the implant. The screw FEA submodel determined that there are lower stresses generated around a 2.6 mm unicortical screw than those surrounding a 2.3 mm bicortical screw when subjected to clinically relevant loading. This suggests that better fixation can be achieved while avoiding bicortical drilling by increasing the major diameter of unicortical bone screws used in ORIF.

Acknowledgment

The authors acknowledge the support of Stryker-Leibinger Inc. for STL and NC.

References

- [1] S. Tada, R. Stegaroiu, E. Kitamura, O. Miyakawa, and H. Kusakari, "Influence of implant design and bone quality on stress/strain distribution in bone around implants: a 3-dimensional finite element analysis," *International Journal of Oral & Maxillofacial Implants*, vol. 18, no. 3, pp. 357–368, 2003.
- [2] A. S. Murthy and J. A. Lehman Jr., "Symptomatic plate removal in maxillofacial trauma: a review of 76 cases," *Annals of Plastic Surgery*, vol. 55, no. 6, pp. 603–607, 2005.
- [3] M. A. C. Gabrielli, M. F. R. Gabrielli, E. Marcantonio, and E. Hochuli-Vieira, "Fixation of mandibular fractures with 2.0 mm miniplates: review of 191 cases," *Journal of Oral and Maxillofacial Surgery*, vol. 61, no. 4, pp. 430–436, 2003.
- [4] J. Lamphier, V. Ziccardi, A. Ruvo, and M. Janel, "Complications of mandibular fractures in an urban teaching center," *Journal of Oral and Maxillofacial Surgery*, vol. 61, no. 7, pp. 745–749, 2003.
- [5] E. C. Benzel, "Implant-bone interfaces," in *Biomechanics of Spine Stabilization: Principles and Clinical Practice*, E. C. Benzel, Ed., pp. 127–134, McGraw-Hill, New York, NY, USA, 1995.
- [6] R. Skinner, J. Maybee, E. Transfeldt, R. Venter, and W. Chalmers, "Experimental pull-out testing and comparison of variables in transpedicular screw fixation. A biomechanical study," *Spine*, vol. 15, pp. 195–201, 1990.
- [7] T. C. Ryken, J. D. Clausen, V. C. Traynelis, and V. K. Goel, "Biomechanical analysis of bone mineral density, insertion technique, screw torque, and holding strength of anterior cervical plate screws," *Journal of Neurosurgery*, vol. 83, no. 2, pp. 324–329, 1995.
- [8] T. C. Ryken, V. K. Goel, J. D. Clausen, and V. C. Traynelis, "Assessment of unicortical and bicortical fixation in a quasistatic cadaveric model: role of bone mineral density and screw torque," *Spine*, vol. 20, no. 17, pp. 1861–1867, 1995.
- [9] D. J. Maiman, F. A. Pintar, N. Yoganandan, et al., "Pull-out strength of Caspar cervical screws," *Neurosurgery*, vol. 31, no. 6, pp. 1097–1101, 1992.
- [10] J. M. Boyle, D. E. Frost, W. L. Foley, and J. J. Grady, "Torque and pullout analysis of six currently available self-tapping and "emergency" screws," *Journal of Oral and Maxillofacial Surgery*, vol. 51, no. 1, pp. 45–50, 1993.
- [11] J. H. Phillips and B. A. Rahn, "Comparison of compression and torque measurements of self-tapping and pretapped screws," *Plastic and Reconstructive Surgery*, vol. 83, no. 3, pp. 447–456, 1989.
- [12] T. Cox, M. W. Kohn, and T. Impelluso, "Computerized analysis of resorbable polymer plates and screws for the rigid fixation of mandibular angle fractures," *Journal of Oral and Maxillofacial Surgery*, vol. 61, no. 4, pp. 481–487, 2003.
- [13] J. R. Fernández, M. Gallas, M. Burguera, and J. M. Viaño, "A three-dimensional numerical simulation of mandible fracture reduction with screwed miniplates," *Journal of Biomechanics*, vol. 36, no. 3, pp. 329–337, 2003.
- [14] A. Wagner, W. Krach, K. Schicho, G. Undt, O. Ploder, and R. Ewers, "A 3-dimensional finite-element analysis investigating the biomechanical behavior of the mandible and plate osteosynthesis in cases of fractures of the condylar process," *Oral Surgery, Oral Medicine, Oral Pathology, Oral Radiology & Endodontics*, vol. 94, no. 6, pp. 678–686, 2002.
- [15] S. T. Lovald, T. Khraishi, J. Wagner, B. Baack, J. Kelly, and J. Wood, "Comparison of plate-screw systems used in mandibular fracture reduction: finite element analysis," *Journal of Biomechanical Engineering*, vol. 128, no. 5, pp. 654–662, 2006.
- [16] S. T. Lovald, J. Wagner, T. Khraishi, J. Kelly, J. Wood, and B. Baack, "Finite element analysis of screw-plate systems for fixation of parasymphseal fractures of the mandible," *Journal of Mechanics*, vol. 23, no. 1, pp. 69–77, 2007.
- [17] N. Chaudhary, S. T. Lovald, J. Wagner, T. Khraishi, J. Kelly, and J. Wood, "Modeling of screw-plate systems for mandibular fracture repair," in *Proceedings of the ASME International Mechanical Engineering Congress and Exposition Conference (IMECE '04) Bioengineering Division*, Bioengineering Division, Anaheim, Calif, USA, November 2004, paper no. 62256.
- [18] S. T. Lovald, J. Wagner, T. Khraishi, J. Kelly, J. Wood, and B. Baack, "Finite element analysis of fixation plates for mandibular fracture reduction," in *Proceedings of the ASME*

- Summer Bioengineering Conference (SBC '05)*, pp. 1406–1407, Vail, Colo, USA, June 2005.
- [19] C. L. Schwartz-Dabney and P. C. Dechow, “Variations in cortical material properties throughout the human dentate mandible,” *American Journal of Physical Anthropology*, vol. 120, no. 3, pp. 252–277, 2003.
- [20] T. W. P. Koriotoh, D. P. Romilly, and A. G. Hannam, “Three-dimensional finite element stress analysis of the dentate human mandible,” *American Journal of Physical Anthropology*, vol. 88, no. 1, pp. 69–96, 1992.
- [21] R. G. Craig and F. A. Peyton, “Elastic and mechanical properties of human dentin,” *Journal of Dental Research*, vol. 37, no. 4, pp. 710–718, 1958.
- [22] A. Bailon-Plaza and M. C. H. van der Meulen, “Beneficial effect of moderate, early loading and adverse effects of delayed or excessive loading on bone healing,” *Journal of Biomechanics*, vol. 36, no. 8, pp. 1069–1077, 2003.
- [23] G. S. Tate, E. Ellis III, and G. Throckmorton, “Bite forces in patients treated for mandibular angle fractures,” *Journal of Oral and Maxillofacial Surgery*, vol. 54, no. 7, pp. 734–736, 1994.
- [24] H. Gray, *Gray’s Anatomy*, Barnes and Noble Books, New York, NY, USA, 15th edition, 1995.
- [25] A. Shirazi-Adl, M. Dammak, and D. J. Zukor, “Fixation pull-out response measurement of bone screws and porous-surfaced posts,” *Journal of Biomechanics*, vol. 27, no. 10, pp. 1249–1258, 1994.
- [26] H. M. Frost, “A 2003 update of bone physiology and Wolff’s law for clinicians,” *The Angle Orthodontist*, vol. 74, no. 1, pp. 3–15, 2003.
- [27] D. van Steenburgh, U. Lekholm, C. Bolender, et al., “Applicability of osseointegrated oral implants in the rehabilitation of partial edentulism: a prospective multicenter study on 558 fixtures,” *Journal of Oral and Maxillofacial Surgery*, vol. 5, no. 3, pp. 272–281, 1990.